CONTROLLER DESIGN AND IMPLEMENTATION FOR A GUIDANCE KIT USED AT SPINNING ROCKETS AND PROJECTILES

A THESIS SUBMITTED TO
THE GRADUATE SCHOOL OF NATURAL AND APPLIED SCIENCES
OF
MIDDLE EAST TECHNICAL UNIVERSITY

BY

GÖRKEM GÜNAY

IN PARTIAL FULFILLMENT OF THE REQUIREMENTS
FOR
THE DEGREE OF MASTER OF SCIENCE
IN
MECHANICAL ENGINEERING

APRIL 2022

Approval of the thesis:

CONTROLLER DESIGN AND IMPLEMENTATION FOR A GUIDANCE KIT USED AT SPINNING ROCKETS AND PROJECTILES

submitted by **GÖRKEM GÜNAY** in partial fulfillment of the requirements for the degree of **Master of Science in Mechanical Engineering Department, Middle East Technical University** by,

Prof. Dr. Halil Kalıpçılar
Dean, Graduate School of **Natural and Applied Sciences** _____

Prof. Dr. Mehmet Ali Sahir Arıkan
Head of Department, **Mechanical Engineering** _____

Prof. Dr. Raif Tuna Balkan
Supervisor, **Mechanical Engineering** _____

Assist. Prof. Dr. Hakan Çalışkan
Co-supervisor, **Mechanical Engineering** _____

Examining Committee Members:

Assoc. Prof. Dr. Ulaş Yaman
Mechanical Engineering, METU _____

Prof. Dr. Raif Tuna Balkan
Mechanical Engineering, METU _____

Assist. Prof. Dr. Orkun Özşahin
Mechanical Engineering, METU _____

Assist. Prof. Dr. Hakan Çalışkan
Mechanical Engineering, METU _____

Assoc. Prof. Dr. Sinan Kılıçaslan
Mechanical Engineering, Gazi University _____

Date:28.04.2022

I hereby declare that all information in this document has been obtained and presented in accordance with academic rules and ethical conduct. I also declare that, as required by these rules and conduct, I have fully cited and referenced all material and results that are not original to this work.

Name, Surname: Görkem Günay

Signature :

ABSTRACT

CONTROLLER DESIGN AND IMPLEMENTATION FOR A GUIDANCE KIT USED AT SPINNING ROCKETS AND PROJECTILES

Günay, Görkem
M.S., Department of Mechanical Engineering
Supervisor: Prof. Dr. Raif Tuna Balkan
Co-Supervisor: Assist. Prof. Dr. Hakan Çalışkan

April 2022, 143 pages

Traditional spin-stabilized projectiles have disadvantages due to low accuracy and precision with respect to guided munitions. There are two main solutions to eliminate these disadvantages. The first one uses a drag brake mechanism to make 1-D guidance by making range correction. The second solution makes 2-D guidance. Since rotation dynamics of a spin-stabilized projectile is faster than existing servo actuators this solution requires isolation of the guidance kit from the rotation of the projectile body. It is possible to use traditional control actuation systems with movable aerodynamic surfaces for 2-D guidance but it requires complicated electronics and a battery. In the scope of this thesis, the feasibility of an actuation solution to 2-D guidance problem of spin-stabilized projectiles is examined. The examined solution uses a fixed canard structure which is isolated from body rotation. The actuator part consists of an alternator. The stator of the alternator rotates with the projectile body and the rotor of the alternator rotates with a fixed canard structure. There is a net torque and a net force generated by fixed canards and guidance can be done by controlling the direction of the net force. Therefore, the main actuation problem is position control

of an alternator. Since the actuation problem is reduced to one-axis position control, required driver electronics and actuators are simplified. And also, it is possible to use power generated by the alternator instead of using a battery.

A test system is developed to simulate the rotation of the projectile body and aerodynamic torque on the guidance kit. Mathematical model of the test system with the alternator is created. To make position control of the alternator, a cascade PI controller is designed and applied in the test system. Requirements of the controller are satisfied with PI controller in the velocity loop and P controller in the position loop. Clamping anti-windup method is used to overcome the overshoot problem caused by the limitation of the controller output in the velocity loop.

Also, in the scope of this thesis, flight dynamics of a spin-stabilized artillery projectile is examined. Firstly, the model is established in 6-DOF, then it is extended to 7-DOF with the addition of 1-DOF generated by the free rotating part of the guidance kit. This 7-DOF flight simulation model is used to find the angular velocity of the projectile body and aerodynamic torque on the guidance kit.

The designed controller is tested with changing aerodynamic torque and body angular velocity. The aerodynamic torque found by using 7-DOF simulation is directly applied to the test system but the angular velocity of the body is scaled down to be inside of the limits of the test system. A disturbance observer is designed to be able to find the sum of the aerodynamic torque and friction torque generated by body angular velocity. The saturation parameters are updated with respect to total disturbance torque on the system to have control ability through to fight time.

Keywords: Cascade PI Control, Disturbance Observer, Projectile Guidance Kit, Projectile Flight Dynamics, Spinning Projectiles

ÖZ

DÖNEN ROKET VE MÜHİMMATLARDA KULLANILAN BİR GÜDÜM KİTİ İÇİN KONTROLCÜ TASARIMI VE UYGULANMASI

Günay, Görkem
Yüksek Lisans, Makina Mühendisliği Bölümü
Tez Yöneticisi: Prof. Dr. Raif Tuna Balkan
Ortak Tez Yöneticisi: Dr. Öğr. Üyesi. Hakan Çalışkan

Nisan 2022 , 143 sayfa

Geleneksel dönü kararlı mermiler düşük hassasiyet ve doğruluk sebebi ile güdümlü mühimmatlara kıyasla dezavantaja sahiptir. Bu dezavantajı gidermek için iki ana çözüm bulunmaktadır. İlk çözüm bir fren mekanizması yardımıyla menzilce tek boyutlu düzeltme yapar. İkinci çözüm iki boyutlu düzeltme yapmaktadır. Dönü kararlı mermilerin dinamiği günümüzde bulunan eyleyicilerin dinamiğinden yüksek olduğu için bu çözümde güdüm kitini mermi gövdesinden yalıtmak gerekir. İki boyutlu düzeltme için hareket edebilir aerodinamik yüzeyler içeren geleneksel kontrol tahrik sistemlerini kullanmak mümkündür ancak bu karmaşık elektronik bileşenler ve batarya gerektirir. Bu tezde dönü kararlı mermi ve roketlerin güdümlendirilme problemine çözüm olabilecek bir yöntem çalışılmıştır. Çalışılan çözüm mermi gövdesinden bağımsız dönebilen sabit kanatlı bir yapı kullanmaktadır. Eyleyici kısmı sarımları mermi gövdesi ile birlikte, mıknatısları sabit kanatlı yapı ile birlikte dönen bir alternatörden oluşur. Sistemde sabit kanatlar tarafından oluşan net kuvvet ve net tork bulunmaktadır ve net kuvvetin yönü ayarlanarak güdüm yapılabilir. Dolayısıyla ana tahrik problemi bir

alternatörün pozisyon kontrolüdür. Temel tahrik problemi tek eksende pozisyon kontrolüne indirgendiğinden dolayı gerekli elektronik sistemler ve eyleyiciler basitleştirilmiştir. Ayrıca alternatörden elde edilen gücü batarya yerine kullanmak mümkündür.

Mermi gövdesinin dönüsünü ve güdüm kiti üzerindeki aerodinamik torku simule etmek için bir test sistemi geliştirilmiştir. Alternatör ile birleştirilen test sisteminin matematiksel modeli elde edilmiştir. Alternatörün pozisyon kontrolü için bir kaskad PI denetleyici tasarlanmış ve test sisteminde uygulanmıştır. Denetleyici isterleri hız döngüsünde PI denetleyici, pozisyon döngüsünde P denetleyici ile karşılanmıştır. Hız döngüsünde denetleyici çıktısının sınırlandırılması nedeniyle oluşan aşım problemini çözmek için "Clamping anti-windup" yöntemi kullanılmıştır.

Bu tezin içeriği kapsamında dönü kararlı top mermilerinin uçuş dinamiği de incelenmiştir. Uçuş dinamiği ilk olarak 6 serbestlik derecesi ile incelenmiş, daha sonra güdüm kiti tarafından sisteme eklenen 1 serbestlik derecesi de dahil edilerek benzetim 7 serbestlik derecesine çıkarılmıştır. 7 serbestlik derecesi içeren uçuş modeli top mermisi gövdesinin açısal hızını ve güdüm kiti üzerinde oluşan aerodinamik torku bulmak için kullanılmıştır.

Tasarlanan denetleyici değişken aerodinamik tork ve gövde açısal hızı için test edilmiştir. 7 serbestlik dereceli uçuş simulasyonu kullanılarak bulunan aerodinamik tork test sisteminde değiştirilmeden uygulanmıştır ancak gövde açısal hızı test sisteminin limitlerinin içinde kalabilmek için oransal olarak azaltılmıştır. Güdüm kiti üzerinde oluşan aerodinamik tork ve gövde dönüsü dolayısıyla oluşan sürtünme torkunun toplam değeri bozucu kestirimi yoluyla elde edilmiştir. Denetleyicilerin doyum noktası değişkenleri sistemdeki toplam bozucu etkiye göre uçuş boyunca denetleme kabiliyetinin korunması amacıyla güncellenmiştir.

Anahtar Kelimeler: Kaskad PI Kontrolcü, Bozucu Kestirimi, Top Mermisi Güdüm Kiti, Top Mermisi Uçuş Mekaniği, Dönü Kararlı Top Mermisi

If you want to find the secrets of the universe, think in terms of energy, frequency and vibration.

ACKNOWLEDGMENTS

Firstly, I want to give my deepest thanks to my supervisor Prof. Dr. Raif Tuna Balkan, and my co-supervisor Assist. Prof. Dr. Hakan Çalışkan for the knowledge and experience they share with me and their positive attitude to me during this thesis period.

I also want to thank Roketsan and my colleagues at this company, for their friendship and their technical support to me during this thesis process. Especially, I want to thank Berkan Bilir who is my first manager at this company.

I owe a thank you to my friends Banu Çiçek Büyüker and Ali Mert Vural for their support during the thesis process. Also, I want to thank Okan Günel, Ali Nuri Güneş-doğdu, Önder Gezer, Cemal Gönen, and Emre Ersoy who are my friends from Mechanical Engineering Department.

Lastly, I am thankful to my family and all my friends for their endless support to me in this thesis and in my life.

TABLE OF CONTENTS

LIST OF TABLES

TABLES

LIST OF FIGURES

FIGURES

LIST OF ABBREVIATIONS

p_{body}: Angular velocity of the projectile or rocket body

p_{gk}: Angular velocity of the guidance kit

J_{body}: Inertia of the projectile or rocket body

J_{gk}: Inertia of the rotating parts of the guidance kit

b: Viscous friction coefficient

T_{aero}:Aerodynamic torque at the guidance kit

K_t: Torque constant of the alternator

K_v: Voltage constant of the alternator

I_a: Current at the alternator

L_a: Phase to phase inductance of the alternator

R_a: Phase to phase resistance of the alternator

C_f: Filter capacitance

I_{load}: Load current

V_{C_f}, V_{L_a}, V_{R_a}: Voltage drop at C_f, L_a, R_a

δV: Resolution of velocity measurement

K_p: Static position error constant

G_{vc}: Transfer function of velocity controller

G_{olp}: Open loop transfer function of position loop

d: Projectile reference diameter

p, q, r: Angular velocities in x, y, z direction

u, v, w: Linear velocities

L, M, N: Moments in x, y, z direction

$L_{gk-7DOF}, L_{B-7DOF}$: Total torque in x-axis in 7-DOF

M_{7DOF}, N_{7DOF}: Moments in y, z direction in 7-DOF

X, Y, Z: Forces in x, y, z direction

$X_{7DOF}, Y_{7DOF}, Z_{7DOF}$: Forces in x, y, z direction in 7-DOF

$C_{L\alpha}$: Lift force coefficient

C_D Drag force coefficient

$C_{yp\alpha}$: Magnus force coefficient

$C_{m\alpha}$: Pitching / Yawing moment coefficient

$C_{np\alpha}$: Magnus moment coefficient

C_{mq}: Ptich / Yaw damping moment coefficient

C_{lp}: Roll damping moment coefficient

C_{rd}: Roll damping moment coefficient of guidance kit

C_{rc}: Roll moment coefficient of guidance kit

$C_{N\delta}$: Normal force coefficient of guidance kit

δ_s: Deflection angle of the steering canards

α: Incidence angle

β: Sideslip angle

ρ: Air density

θ_{gk}: Roll angle of the guidance kit

V: Magnitude of the projectile velocity

S: Reference area

L: Lift force

D: Drag force

K: Magnus force

$\mathbf{M}_{py}$: Pitching/Yawing moment

$\mathbf{M}_m$: Magnus moment

$\mathbf{M}_{pyd}$: Pitch/Yaw damping moment

$\mathbf{M}_{rd}$: Roll damping moment

$\mathbf{F}_g$: Gravitational force

$\mathbf{F}$: Total aerodynamic force for 6-DOF modeling

$\mathbf{M}$: Total aerodynamic moment for 6-DOF modeling

$\mathbf{F}_c$: Control forces generated by guidance kit

$\mathbf{M}_c$: Control moments generated by guidance kit

l_{CG}: Distance between pressure center of the steering canards and center of mass of projectile

$\mathbf{F}_{7DOF}$: Total aerodynamic force for 7-DOF modeling

$\mathbf{M}_{7DOF}$: Total aerodynamic moment for 7-DOF modeling

T_{ad}: Damping torque due to the angular velocity of the guidance kit at roll axis

$L_{gk-7DOF}$: Total aerodynamic torque on the guidance kit at the roll axis

C_{rdgk}: Roll damping moment coefficient of the guidance kit

ϕ, θ, ζ: Euler angles

DOF: Degree of freedom

m: Mass of the projectile

Q: Filter transfer function

$\hat{G}$: Reduced transfer function between I_{load} and P_{gk}

CHAPTER 1

INTRODUCTION

1.1 Motivation and Problem Definition

Preventing civilian losses and having more precise strikes are increasing trends in modern warfare environments [1]. Traditional artillery projectiles have disadvantages due to low accuracy and precision in comparison to missiles and guided rockets [2]. And also having more precise strikes by using artillery projectiles requires adjustment fire and observation and evaluation of the impact point location to correct the firing parameters at the coming fire. This adjustment fire significantly decreases the chance of destroying the target because of the time it consumes and it produces a risk at the secrecy of the operation.

Developing a guided projectile requires navigation and guidance components which need to be functional after gun launch and operational during flight. At the gun launch, there is 15000g axial and 5000g radial acceleration exist and at the flight phase, the projectile has an angular velocity of about 270 Hz [3].

The motivation behind this thesis is to develop a test system for the feasibility study of the actuation system of a guidance kit that can be used at spin-stabilized munitions. Also this thesis aims to develop a flight simulation of a spin-stabilized projectile to have the necessary information for guidance kit design.

1.2 Literature Survey

In the existing works, there are two commonly used approaches to convert existing spin-stabilized artillery projectiles to guided munitions. One of them is a 1-D approach which has a brake mechanism at its structure. In this approach, the projectile is aimed intentionally behind the target and the reduction existed by the use of the drag brake in the range of the projectile is used to make a range correction [4]. One of the examples of this 1-D correction drag brake is given in Figure 1.1. This is a simple approach but it does not have the control ability to make side corrections.

Figure 1.1: An Example Design of 1-D Control Approach by Using Drag Brake

The other approach is making 2-D guidance by using movable canards or fixed canards. At the spinning projectiles, it is not possible to use conventional actuators due to the high bandwidth requirement which is proportional with the angular velocity of the projectile[4]. Therefore, it is found to be necessary to isolate the rotation of the part that has actuators from the projectile body. We can divide the design that makes 2-D guidance into two. The first uses movable aerodynamic surfaces to have necessary forces and moments for guidance. An example of this is given in Figure 1.2. This solution requires complicated actuators and drivers. Also, a battery is necessary to supply power to control actuation system components. These are disadvantages due to volume and mass limitations.

Figure 1.2: An Example Design Which Uses Movable Aerodynamic Surfaces

There is also an interesting approach that uses fixed aerodynamic surfaces isolated from the projectile body to make 2-D guidance [5]. This alternative uses 4 fixed canards attached to an isolated part from the projectile body. The cant angles of these canards are arranged such that 2 of them produce an aerodynamic torque in the opposite direction of the angular velocity of the projectile body. The others produce a net force that is required for guidance. The arrangement of the fixed canard structure is shown in Figure 1.3 and an example of this type of design is given in Figure 1.4. The actuator of this system is an alternator its rotor is attached to the fixed canard structure and its stator is attached to the projectile body. This approach simplifies the actuation problem to one axis and reduces the complexity of required components. Since it is possible to generate power for other avionic components by using the alternator, the battery requirement can be eliminated.

The actuator part of the fixed canard structure is examined by Zhang, Li, Xiao, and Tian in 2016 for a mortar projectile [6]. The schematic of the used control structure is given in Figure 1.5. Also in this work, the platform of the control system simulation is explained. They used two motors to simulate the angular velocity of the mortar munition and aerodynamic torque at the canards. They measured the angular velocity of the fixed canard structure by using a gyroscope and used fourth-order Runge-Kutta integral to calculate roll angle. The test platform they used is given in Figure 1.6.

A similar actuation mechanism for artillery projectiles is examined and test results are given by Yin, Jia, and Yu in 2018. In this work, roll angle information of the guidance kit body is taken by using a geomagnetic sensor, and a hall sensor is used

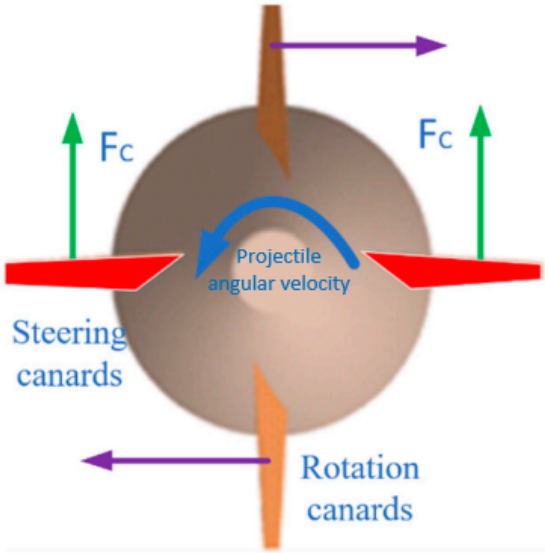

Figure 1.3: Orientation of Fixed Canard Structure

Figure 1.4: An Example Design Which Uses Fixed Aerodynamic Surfaces

to get the position of the fixed-wing structure with respect to the projectile body [7]. A cascade structure is used to control the velocity and position of the fixed canard structure. They used a proportional controller in the position loop and a proportional-integral controller in the velocity loop. The closed-loop control system they used is given in Figure 1.7.

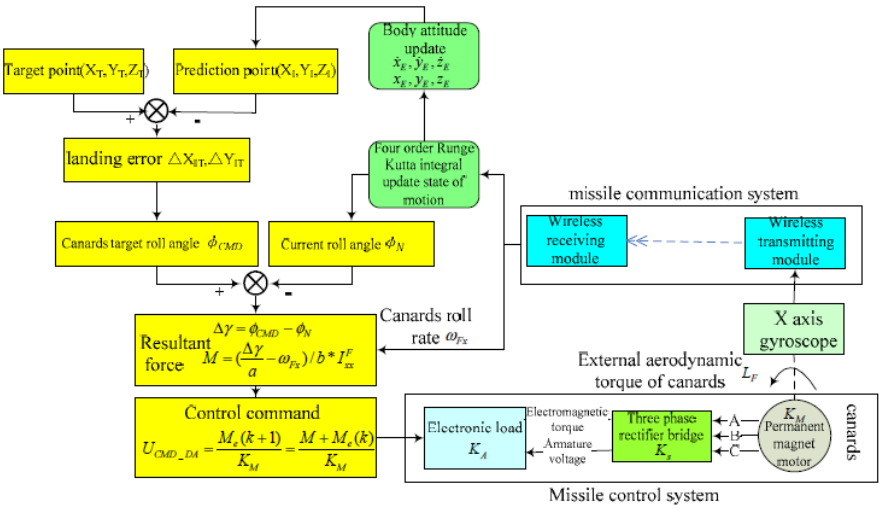

Figure 1.5: Schematics of Zhang, Li, Xiao and Tian's Control Structure

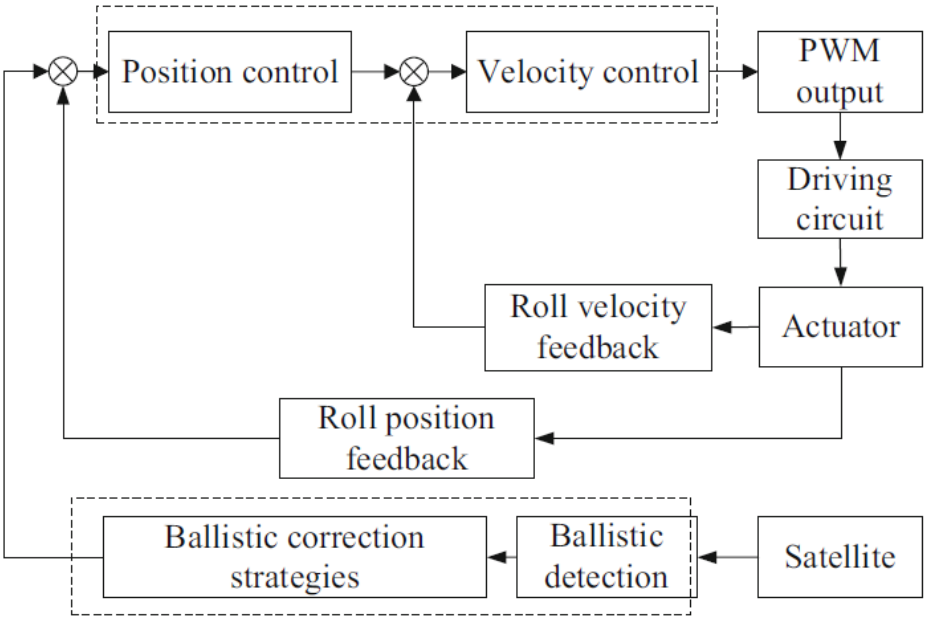

Figure 1.7: Yin, Jia and Yu's Control Structure

Flight dynamics of a projectile which has an isolated part from body rotation of the projectile is examined by Costello in 1998 [8]. The projectile body is modeled as two inertia elements that can rotate relative to each other and connected with bearings. The projectile schematic used is given in Figure 1.8. In this figure, Φ_F represents the roll angle of the forward body and Φ_A represents the roll angle of the aft body. And

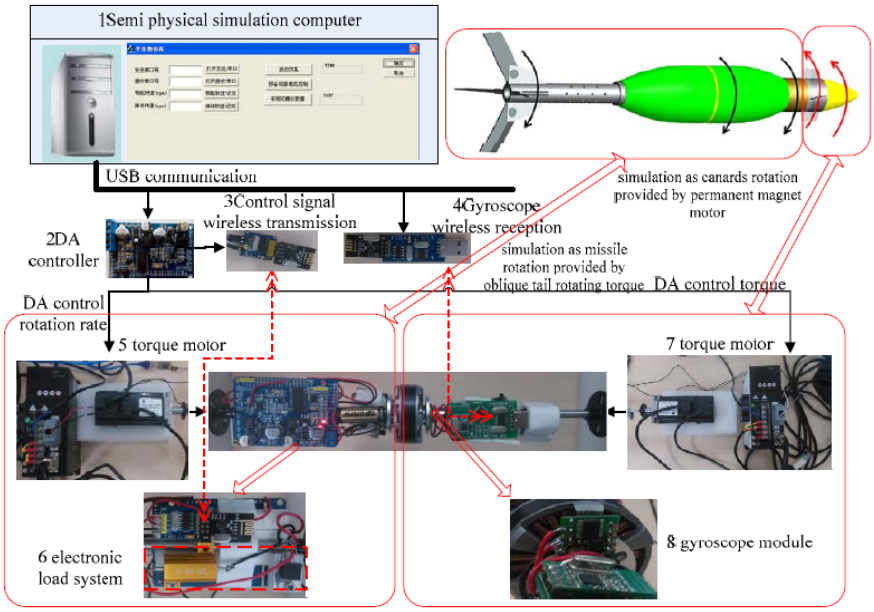

Figure 1.6: Zhang, Li, Xiao and Tian's Test Set-up

forward body and aft body can rotate relatively.

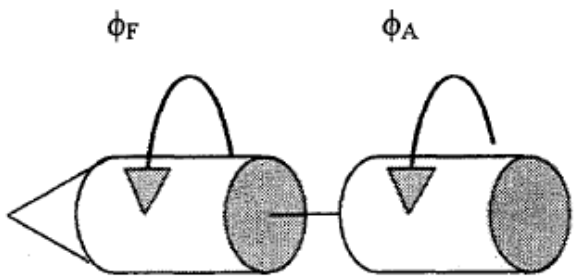

Figure 1.8: Costello's Projectile Schematic

In 2010, Wernert, Theodoulis, and Morel work on the equation of motion of a dual-spin projectile in different reference frames [9]. They compared the computational work required at every reference frame to choose the optimum frame for guidance purposes in real-life. In 2012, Costello presented his work with some modifications which make it possible to use an impact point prediction method for guidance purposes. In 2019, Zhang, Yao, and Zheng presented their work on the guidance of an

artillery projectile by using fixed canards [10].

1.3 Contributions and Novelties

The thesis contributes to the literature in the parts listed below.

- Developing a test system to make the feasibility analysis of a 2-D guidance kit actuation system that uses a fixed canard structure. A controller is designed and tested for the actuator part of the guidance kit which mainly consists of position control of an alternator.
- Dynamics of the spin-stabilized projectile is modeled and simulated in 6-DOF and 7-DOF. By using this 7-DOF simulation, aerodynamic torque and body angular velocity are found and they are applied using the test set-up to test control ability through flight.

1.4 The Outline of the Thesis

Introduction, literature survey, and contributions to literature are given in Chapter 1. Guidance methods for artillery projectiles are listed. The advantage and disadvantages of guidance methods are explained.

Explanation of the test system, list of the test hardware, and explanations of test software are given in Chapter 2. The relationships between components of the system are also explained in this section.

The mathematical model and simulations of the actuation system are given in Chapter 3. The results are presented and different modeling techniques are compared.

Controller design for the actuation system is given in Chapter 4. In this chapter, the test results of the designed controller and the comparison of the test results with simulation are also presented.

Modeling and simulation of flight dynamics of a spin-stabilized projectile are given in Chapter 5. First, a 6-DOF model is established and the 6-DOF model is updated to

7-DOF to include the additional degree of freedom.

The impact of the changing aerodynamic torque and body angular velocity are examined in the simulation environment in Chapter 6. Three different solutions are proposed to make the controller more robust to changes in the torque and body angular velocity. The simulation results of the solutions are also explained in this chapter.

The test results of the modified controllers for changing aerodynamic torque and velocity are presented in Chapter 7.

Conclusion and future work are given in Chapter 8.

CHAPTER 2

EXPLANATION OF THE TEST SYSTEM

2.1 Explanation of System Aim to be Tested

A projectile that contains a guidance kit is given in Figure 2.1 with axis convention. A general spin-stabilized 155 mm artillery projectile has a large angular velocity on X-axis to have gyroscopic stabilization. The angular velocity can change between 10000 rpm and 20000 rpm with the powder charge of the firing. The linear velocity of the projectile increases with increasing powder charge and there is a linear relationship between linear velocity and angular velocity at the barrel outlet. Angular velocities of the projectile with respect to powder charge are given in Table 2.1. The direction of the projectile rotation is +X-axis.

Table 2.1: Axial and Angular Velocities of 155 mm Spin-Stabilized Projectile

Powder Charge	Initial Velocity (m/s)	Initial Angular Velocity (Hz)	Final Angular Velocity (Hz)
3M	546.4	176.3	128.2
4M	676.7	218.3	158.8
5M	812.4	262.1	190.6
6M	943.5	304.4	221.3

Preliminary design of a guidance kit is shown in Figure 2.2. The guidance kit mainly consists of 3 parts which are the guidance kit body (Green part in Figure 2.2), the nose of the projectile (Orange part in Figure 2.2), and the part that contains 4 fixed canards (Blue part in Figure 2.2).

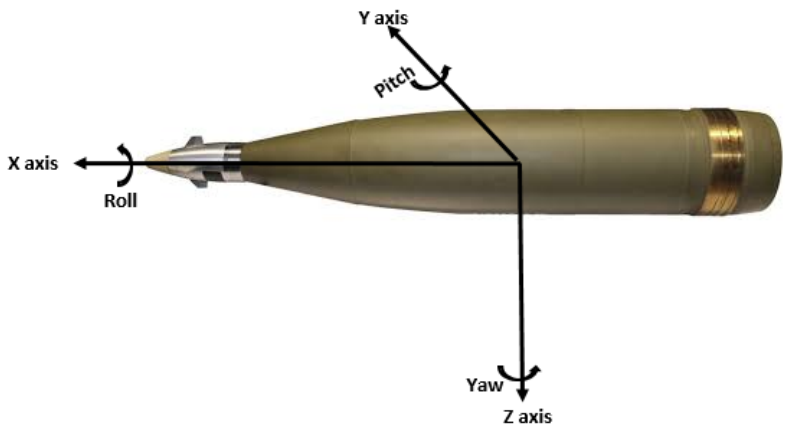

Figure 2.1: An Example Projectile with Guidance Kit

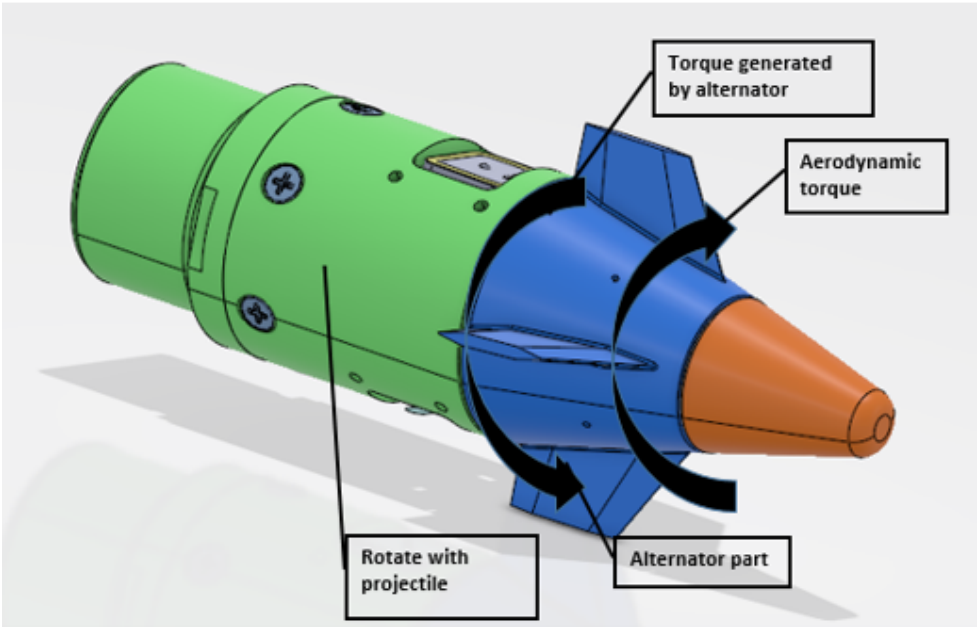

Figure 2.2: Preliminary Design of Guidance Kit

Section view of Figure 2.2 is given in Figure 2.3. Guidance kit body and nose fixed to each other. The green part is connected to the projectile body and rotates with the body. The blue part is isolated from the projectile body by using two bearings and it can rotate freely on X-axis. A permanent magnet synchronous alternator is attached to the system as an actuator and power source for avionic components. The rotor of the alternator is fixed to the blue part and the stator of the alternator is fixed to the

green part. Since there is no stationary part in the system, it is not possible to use classical rotor and stator convention. The part which has permanent magnets is called as rotor and the part which has coils is called as stator. There are four fixed canards on the outside of the rotor. The canards are fixed to the rotor, so they rotate with the blue part. Therefore, the rotation of the canards on the X-axis is free from the projectile body.

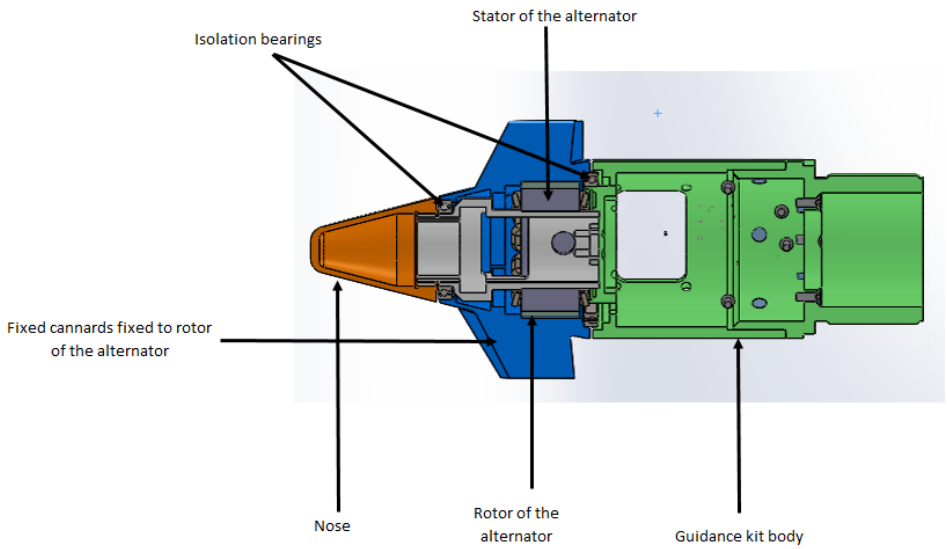

Figure 2.3: Section View of Preliminary Design of an Example Guidance Kit

A closer look at the canards is given in Figure 2.4. Two of the canards have the same cant angle. These canards are shown at 0° and 180° in Figure 2.4. These canards are called steering canards. The aerodynamic forces on these canards are also shown in Figure 2.4 with yellow color. Since the forces on these canards have the same direction, the torques generated by these forces on the X-axis cancel each other and they do not form any net torque but they form a net force that is double of the aerodynamic force at one of the steering canards. This net force will be used to make 2-D guidance.

The other two canards have opposite cant angles which are shown at 90° and -90° in Figure 2.4. The aerodynamic forces are also shown in Figure 2.4 with red color. Since the directions of these two forces are opposite, they cannot form a net force but they form a net torque on the X-axis.

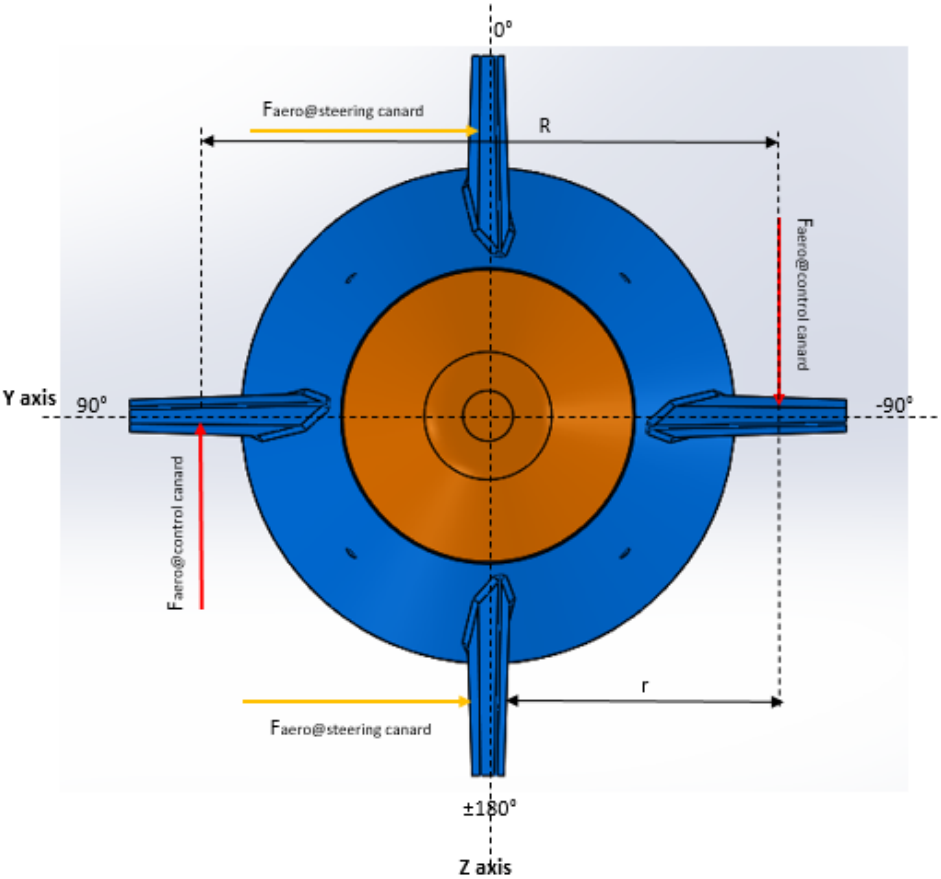

Figure 2.4: Steering and Control Canards and Axis System

The meanings of the symbols in Figure 2.4 are given below.

- F_{aero}@steering canard: Total aerodynamic force acting on one of the steering canards at the center of pressure.
- F_{aero}@control canard: Total aerodynamic force acting on one of the control canards at the center of pressure.
- r: The distance from the center of pressure of the control canard to the X-axis.
- R: The distance of the center of pressures of control canards.

The cant angles of the canards are adjusted such that the direction of T_{aero} (-X-axis)

and the rotation of the projectile body (+X-axis) are opposite to each other. Therefore, we can form a torque in the opposite direction of the T_{aero} by loading the alternator.

The guidance kit aims to adjust the direction of the net force at steering canards with respect to the earth fixed reference frame by using the torques which are given in Figure 2.5.

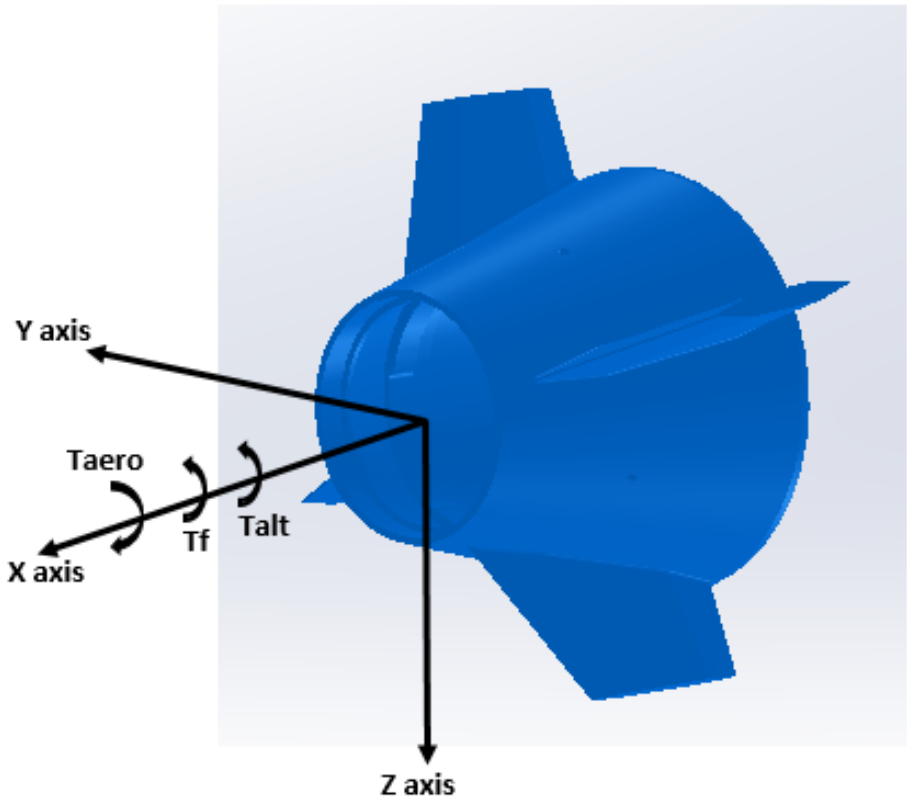

Figure 2.5: Torques at Fixed Canard Structure

The meanings of the symbols in Figure 2.5 and explanations of them are given below.

- T_{aero}: Total aerodynamic torque formed by control canards. It is at -X direction.

  $T_{aero} = f(Projectile\,Velocity\,, Altitude)$.

  It depends on the altitude because the air density is significantly changing with altitude.

- T_f: Friction torque at the bearings. It is in the same direction with projectile angular velocity. (+X)

  $$T_f = f(Relative\,Velocity,\ Radial\,and\,Axial\,Load)$$

- T_{alt}: The torque generated by the alternator by taking current on it. It is in the same direction with projectile angular velocity.(+X)

  $$T_{alt} = f(Load\,on\,Alternator)$$

This test set-up aims to make a feasibility analysis of the actuation system of the guidance kit which mainly consists of position control of an alternator. The stator of the alternator is connected to the projectile body and the rotor can rotate freely, under the torques which are shown in Figure 2.5.

2.2 Explanation of Test Hardware

2.2.1 General Description of the Test Set-up

The main purpose of the test set-up is to have a test system that can simulate aerodynamic torque on the guidance kit and body angular velocity of the projectile or rocket; therefore having a ground test opportunity for the actuation system of the guidance kit.

The schematic of the test set-up is given in Figure 2.6. Also, the pictures of the test set-up with the name of the components used is given in Figure 2.7, Figure 2.8, and Figure 2.9.

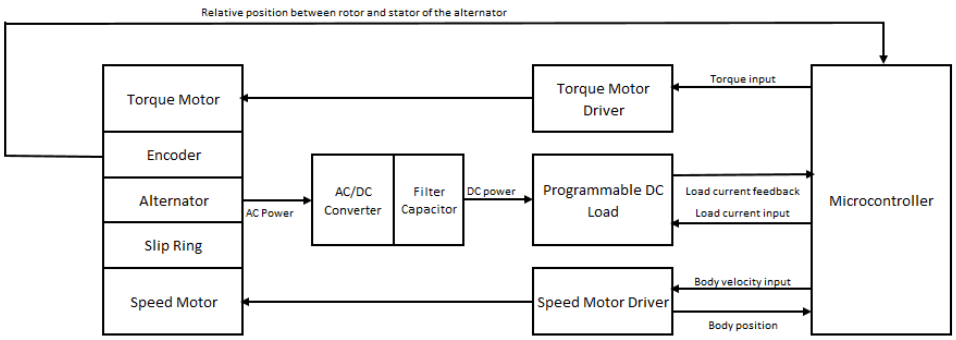

Figure 2.6: Schematic of the Test Set-up

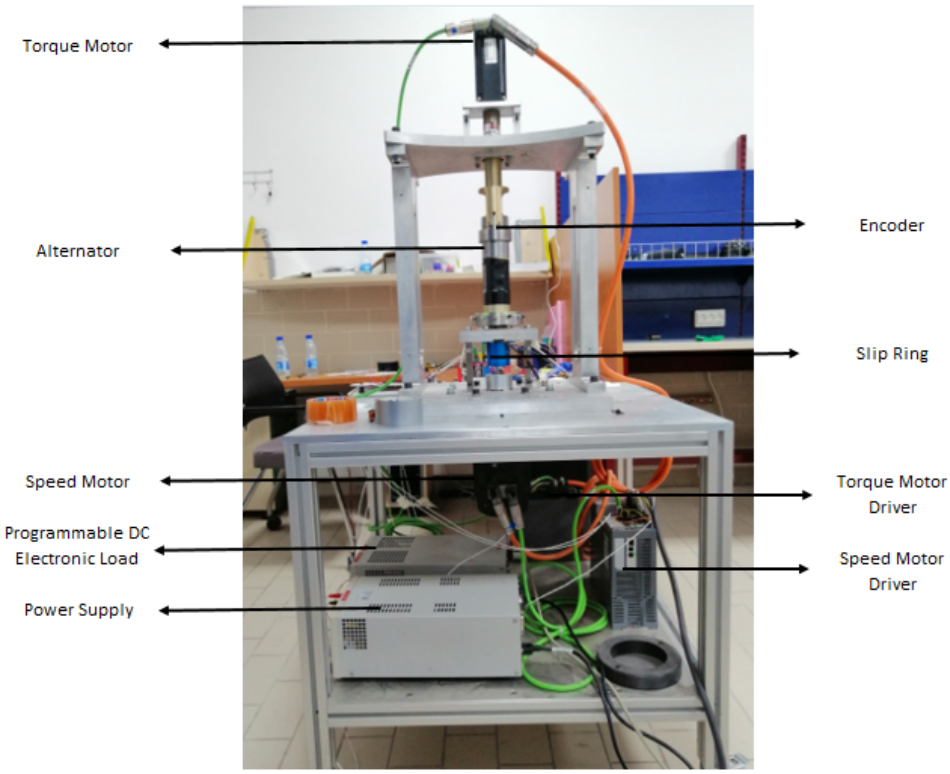

Figure 2.7: General View of Test Set-up

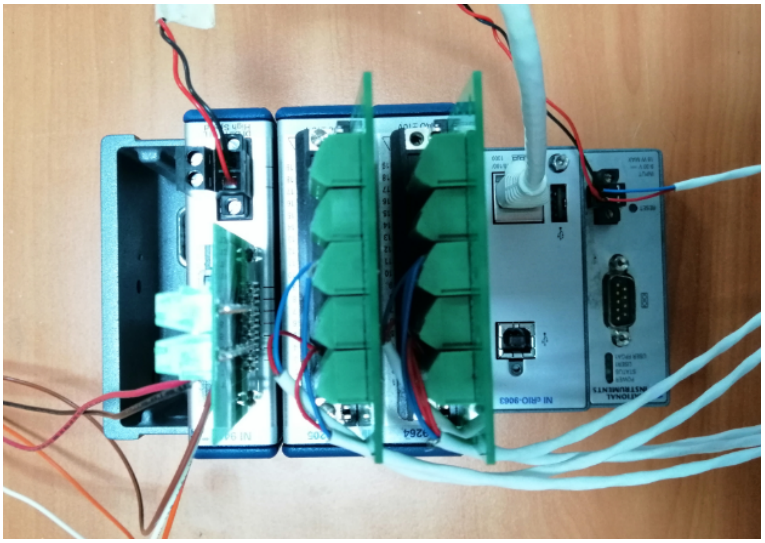

Figure 2.8: Micro-controller Part

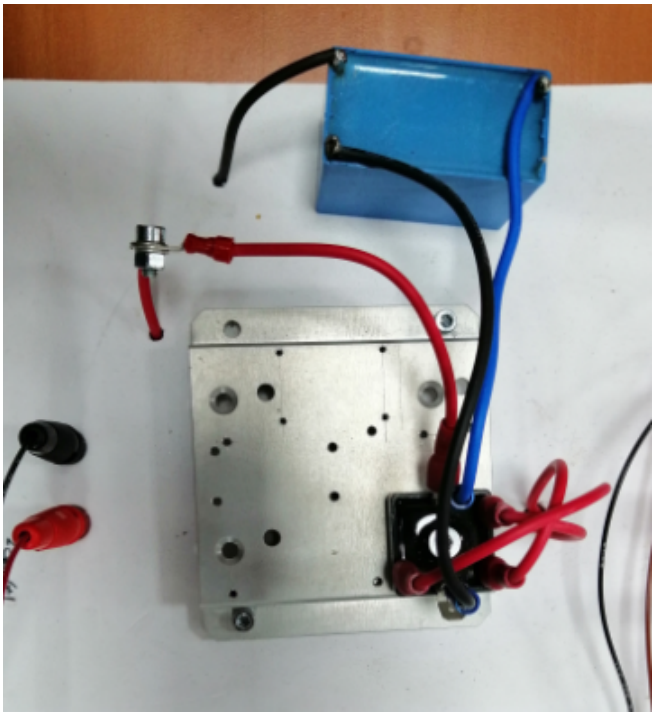

Figure 2.9: AC/DC Converter and Filter Capacitor

This set-up simulates aerodynamic torque on the guidance kit with a BLDC motor used in torque control mode. Also, the angular velocity of the projectile or rocket body is simulated with another BLDC motor used in speed control mode. The stator

of the alternator is fixed to the part that rotates with the speed motor. There is an optical encoder between the rotor and the stator of the alternator to find the relative position between the projectile or rocket body and the guidance kit. A slip ring is used to transform the power of the alternator and encoder signals from rotating to the stationary part. Data acquisition of feedback signals from motor drivers and encoder, evaluation of the data to find control input and generation of output signals is done using the micro-controller in the system.

2.2.2 Specifications of the Test Hardware

The section view of the test set-up is given in Figure 2.10 and a zoomed view of the actuator part is given in Figure 2.11. The mechanical parts which have an inertial load at the alternator are numbered and numerical values are given in Table 2.2.

Table 2.2: Mechanical Parts of the Actuator Part of Test Set-up

Part Number	Value/Name/Type	Inertia (kgm^2)
1	Coupling	4.069×10^{-5}
2	Holding Part	1.678×10^{-4}
3	Alternator Body	7.55×10^{-4}
4	Alternator Magnets	1.485×10^{-4}

The components used in this set-up are listed below with their basic properties.

Speed Motor This is used to simulate the angular velocity of the projectile body. Related specifications with speed motor are given in Table 2.3.

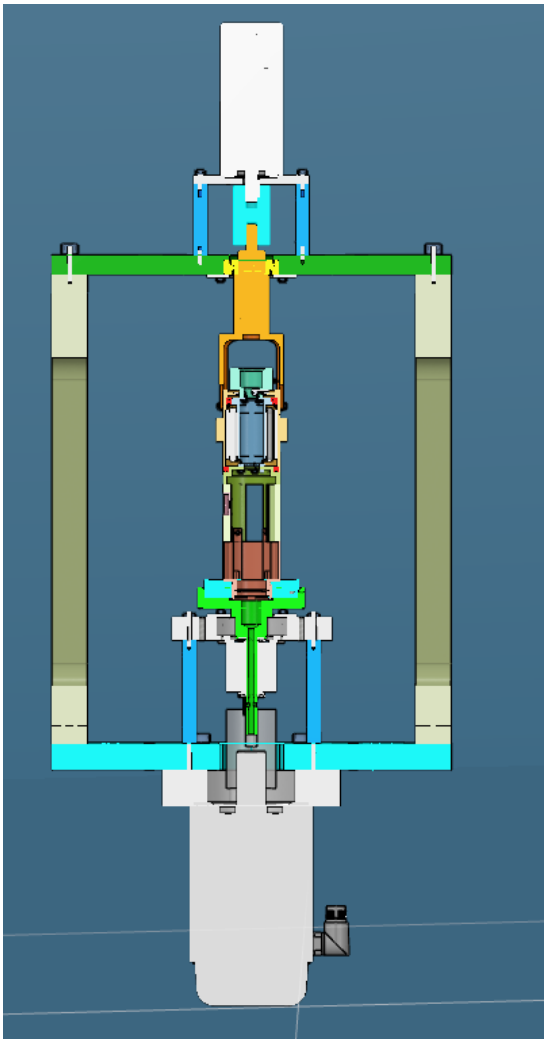

Figure 2.10: Section View of the Test Set-up

Table 2.3: Speed Motor Specifications

Parameter	Value/Name/Type	Unit
Manufacturer	Kollmorgen	NA
Model	AKM63M	NA
Voltage	480	V_{AC}
Torque Constant	1.23	$\frac{Nm}{A}$
Rated Power	4.95	kW
Rated Speed	4500	rpm
Rated Torque	10.5	Nm
Rotor Inertia	24	$kgcm^2$

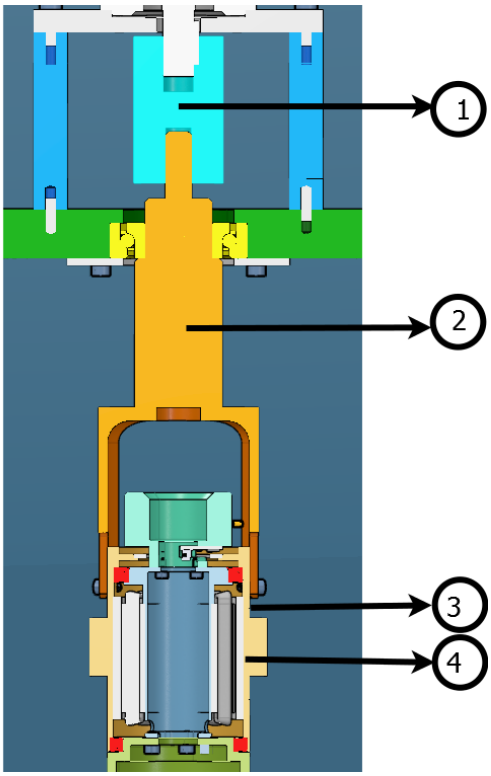

Figure 2.11: Zoomed View of Actuator Part

Torque Motor This is used to simulate the aerodynamic torque at the system. Related specifications with torque motor are given in Table 2.4.

Table 2.4: Torque Motor Specifications

Parameter	Value/Name/Type	Unit
Manufacturer	Kollmorgen	NA
Model	AKM-33H	NA
Voltage	240	V_{AC}
Torque Constant	0.51	$\frac{Nm}{A}$
Rated Power	1.31	kW
Rated Speed	5500	rpm
Rated Torque	2.27	Nm
Rotor Inertia	0.85	$kgcm^2$

Speed Motor Driver This component is used to control the speed motor. Related specifications with speed motor driver are given in Table 2.5.

Table 2.5: Speed Motor Driver Specifications

Parameter	Value/Name/Type	Unit
Manufacturer	Kollmorgen	NA
Model	AKD-P02407	NA
Continuous Current	24	A
Peak Current	48	A
Continuous Power	16	kW

Torque Motor Driver This component is used to control the torque motor. Related specifications with torque motor driver are given in Table 2.6.

Table 2.6: Torque Motor Driver Specifications

Parameter	Value/Name/Type	Unit
Manufacturer	Kollmorgen	NA
Model	AKD-P02207	NA
Continuous Current	12	A
Peak Current	30	A
Continuous Power	8	kW

Encoder This is used to measure the relative angle and velocity between the rotor and the stator of the alternator. Related specifications with the encoder are given in Table 2.7.

Table 2.7: Encoder Specifications

Parameter	Value/Name/Type	Unit
Manufacturer	FENAC	NA
Sensing Type	Optic	NA
Encoder Type	Incremental with index	NA
Resolution	2500	CPT

Alternator This component is the actuator part of the guidance kit. Related specifications with this component are given in Table 2.8.

Table 2.8: Alternator Specifications

Parameter	Value/Name/Type	Unit
Manufacturer	Volt Defence	NA
Torque constant	0.716	$\frac{Nm}{A}$
Speed constant	0.749	$\frac{V}{rad/sec}$
Number of pole pairs	7	NA
Resistance(ph-ph)	6.2	Ohm
Inductance(ph-ph)	8.8	mH
Continuous Power	1.2	kW
Inertia of magnets	1.485	$kgcm^2$

Slip Ring This component is used to transfer alternator power and encoder signals from the rotary part to the stationary part. Related specifications with slip ring are given in Table 2.9.

Table 2.9: Slip Ring Specifications

Parameter	Value/Name/Type	Unit
Manufacturer	Senring	NA
Number of circuit	12	NA
Maximum speed	5000	rpm
Maximum current	5	A

Filter Capacitor This component is used to filter transient components of voltage which is produced due to the effect of the inductance of the alternator under sudden changes in the current. The specifications related to the filter capacitor are given in Table 2.10.

Table 2.10: Filter Capacitor Specifications

Parameter	Value/Name/Type	Unit
Manufacturer	TDK	NA
Maximum voltage	800	V
Capacitance	50	μF
Capacitance tolerance code	K	NA

AC/DC Converter This component is used to convert the AC voltage generated by the alternator to DC voltage. Related specifications with AC/DC converter are given in Table 2.11.

Table 2.11: AC/DC Converter Specifications

Parameter	Value/Name/Type	Unit
Manufacturer	Vishay	NA
Model	VS-36MT140	NA
Maximum continuous DC current	25	A
V_{RRM}	1400	V

Power Supply This component is used to supply the required power for logic supplies of motor drivers, the micro controller, and the encoder. Related specifications with power supply are given in Table 2.12.

Table 2.12: Power Supply Specifications

Parameter	Value/Name/Type	Unit
Manufacturer	Aim TTI	NA
Model	CPX 400D	NA
Maximum current	20	A
Maximum voltage	60	V
Continuous Power	420	W

Programmable DC Electronic Load This component is used to load the alternator at the required current. The specifications related to this component are given in Table 2.13.

Table 2.13: Programmable DC Electronic Load Specifications

Parameter	Value/Name/Type	Unit
Manufacturer	Aim TTI	NA
Model	LD400P	NA
Maximum current	80	A
Maximum voltage	80	V
Continuous Power	400	W
Short term power	600	W

Micro-controller Components These components are used for data acquisition from other components, executing controller software, and producing control input. Related specifications with these components are given in Table 2.14

Table 2.14: Micro-controller Components

Manufacturer	Model	Function
National Instruments	NI-9063	Main controller
National Instruments	NI-9205	Analog Input
National Instruments	NI-9264	Analog Output
National Instruments	NI-9411	Digital Input (Encoder)

2.3 Explanation of the Test Software

The test software is written by using Labview program which is developed by National Instruments company. The software consists of two main parts. The first part is executed at the test computer and it is responsible for taking input and presenting output data. The user interface of this part is given in Figure 2.12.

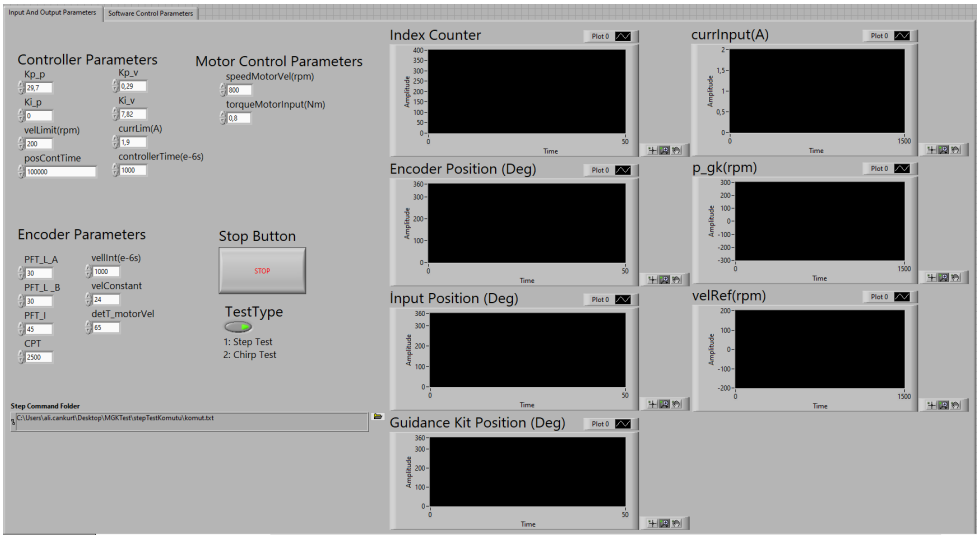

Figure 2.12: User Interface of the Test Software

The second part is programmed by using FPGA target of the NI-9063 to have fast and real-time execution. This part of the program is mainly responsible for finding the velocity and position of the guidance kit by using encoder signals and speed motor position data; executing the control algorithm and generating input signals for DC electronic load, speed motor driver, and torque motor driver.

Data acquisition for encoder signals is done with NI-9411 digital input module. While evaluating encoder data, in order not to take noises as a physical signal an input line filter of 30 μs is used while evaluating A and B line signals of the encoder; and 45 μs input line filter is used for the index signal. The measurement of the velocity is done with 1 ms time intervals. The resolution of this measurement is given in Equation 2.1. The software part which is responsible for the evaluation of encoder data is given in Figure 2.13.

$$\begin{aligned} \delta V &= \frac{1}{2500} \times 1000 \times 2\pi(rad/s) \\ \delta V &= 24(rpm) \end{aligned} \tag{2.1}$$

The controller algorithm is executed at 1kHz and the output is also updated at the same frequency. The controller designed in Chapter 4 is applied in real-life by using this part with saturation dynamics and determination of the direction of the error

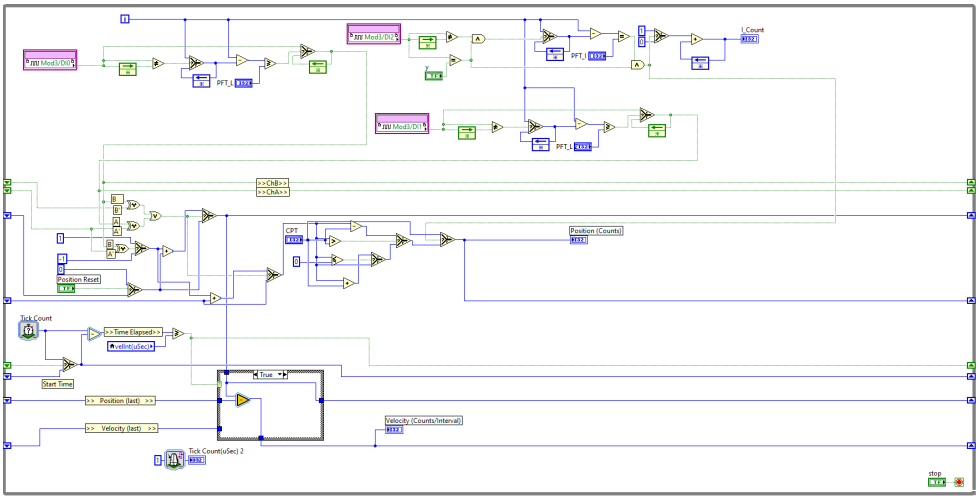

Figure 2.13: Encoder Evaluation Part of the Test Software

to apply minimum control effort. The software part which is responsible for the execution of the control loop is given in Figure 2.14.

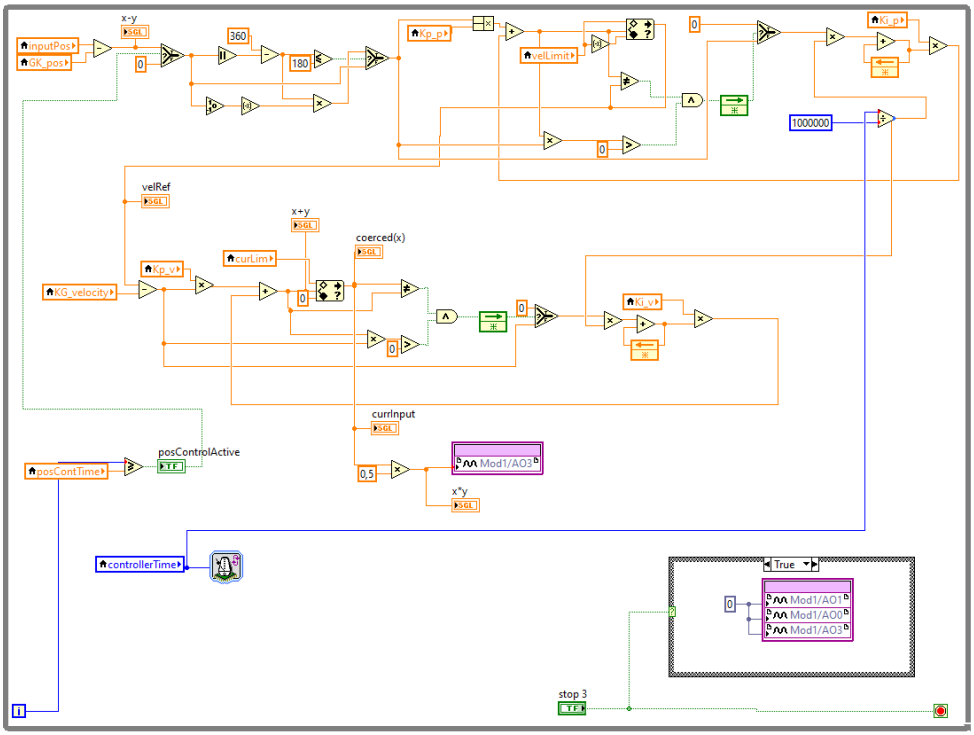

Figure 2.14: Controller Part of the Test Software

CHAPTER 3

MATHEMATICAL MODEL OF THE TEST SYSTEM

A detailed mathematical model of the test system is constructed and simulated in this chapter. Different modeling techniques are used and the results are compared with each other. Lastly, required transfer functions to make controller design is found and the results of the transfer function model and the state space model are compared.

The representations of the physical components of the test system are given in Figure 3.1. Alternator at the system modeled as a voltage source with series connection of resistance and inductance of the alternator. Filter capacitor connected to alternator circuit in parallel connection. Viscous friction between rotating parts is modeled as a damper and the damping coefficient is found by using test results. Lastly, the current at DC electronic load is modeled as a current source at the system. At the real artillery projectile, the angular velocity of the body is an initial condition. Since the test set-up simulates this with a speed controlled BLDC motor, the angular velocity of the projectile body is modeled as a source element.

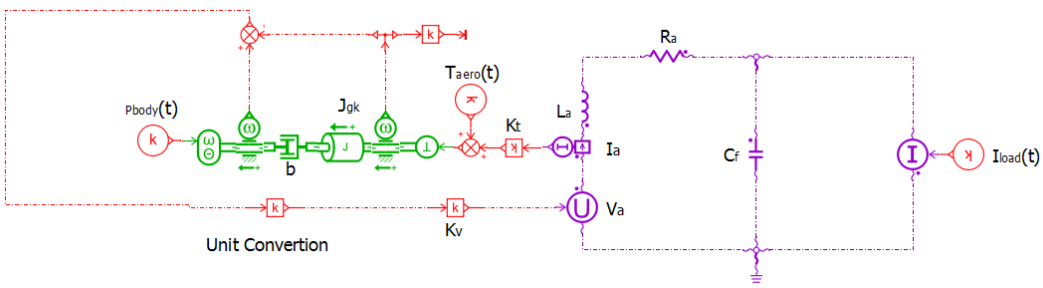

Figure 3.1: Physical Model of Test Set-up

3.1 State Space Model

The Linear Graph Method is used to find the system model systematically. The linear graph model of the system is shown in Figure 3.2. To be consistent with notation used in flight dynamics, angular velocities at the system are presented with p.

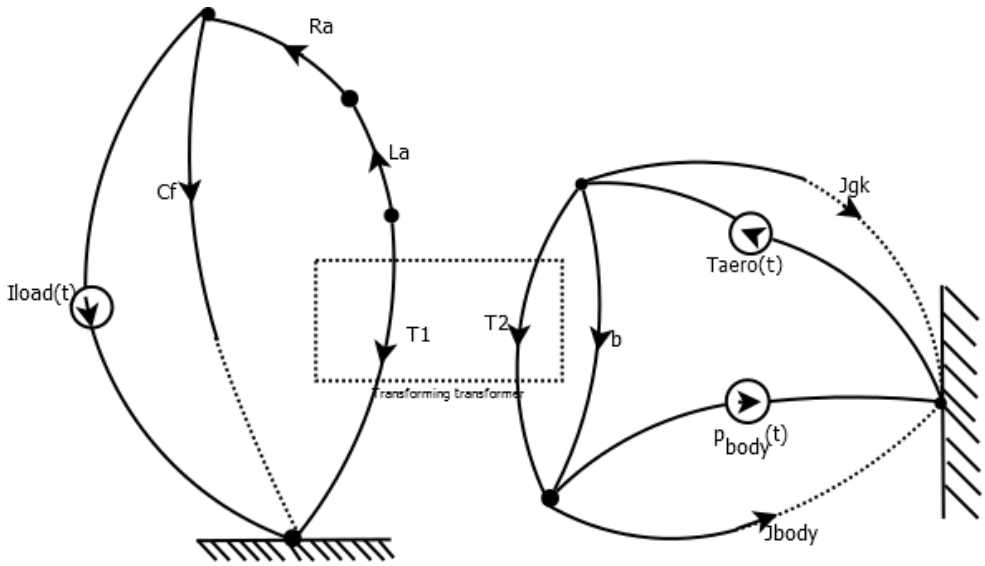

Figure 3.2: Linear Graph Model of Test Set-up

Parameters required to form the tree are given below:

- (Number of nodes) N = 7
- (Number of distinct graph) N_d= 2
- (Total number of branches)B = 11
- (Number of branches at tree) $B_T = N - N_d = 7 - 2 = 5$
- (Number of link) $B_L = B - B_T = 11 - 5 = 6$

The procedure followed to form the tree is given below:

- Step 1: Include all across variable sources as tree branches.

  $p_{body}(t)$ is included. (1 branch)

- Step 2: Include as many as A-type elements with one branch of the transformer.

  J_{gk}, C_f, and T_1 are included. (3 branches)

- Step 3: Complete the tree with resistance elements.

  R_a is included and the required 5 branches are completed.

The tree of the system is given in Figure 3.3; tree branches are shown in red color, and links are shown in black color.

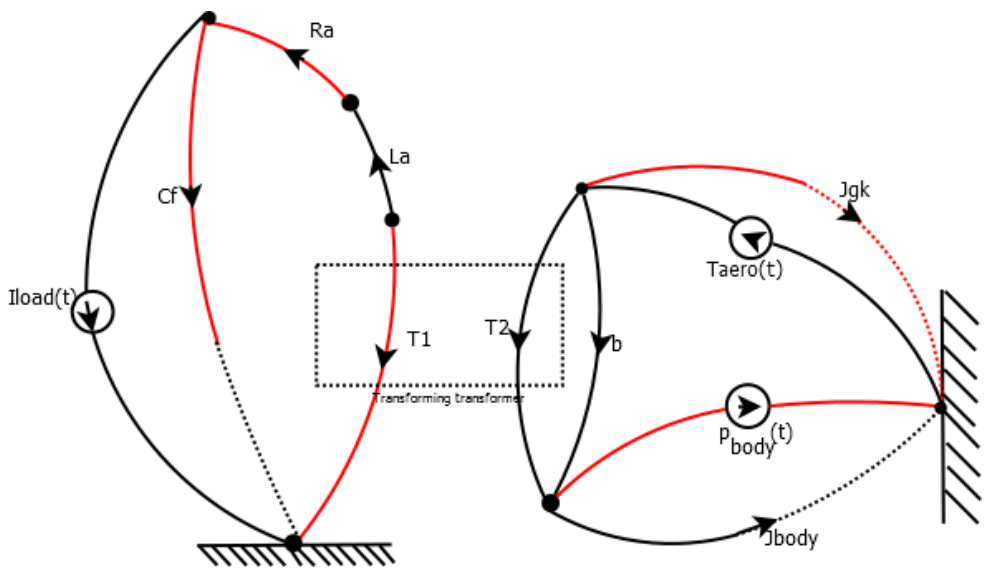

Figure 3.3: System Tree of the Linear Graph Model

All primary and secondary variables of the system, elemental equations, compatibility and continuity equations are given in Appendix A. The states of the system are p_{gk}, V_{C_f} (A-type energy storage elements across variables on the tree branches), and I_{L_a} (T-type energy storage element through variables on the links). p_{gk} refers to the angular velocity of the guidance kit, V_{C_f} refers to the voltage difference between high and low side of the capacitor, and I_{L_a} refers to the current on the alternator. The equations in commonly used matrix form are given in Equation 3.1, Equation 3.2, Equation 3.3, Equation 3.4, and Equation 3.5.

$$\dot{\mathbf{x}} = \mathbf{Ax} + \mathbf{Bu} \tag{3.1}$$

$$\mathbf{x} = \begin{bmatrix} p_{gk} \\ V_{C_f} \\ I_{L_a} \end{bmatrix} \tag{3.2}$$

$$\mathbf{u} = \begin{bmatrix} p_{body}(t) \\ T_{aero}(t) \\ I_{load}(t) \end{bmatrix} \tag{3.3}$$

$$\mathbf{A} = \begin{bmatrix} \frac{-b}{J_{gk}} & 0 & \frac{K_t}{J_{gk}} \\ 0 & 0 & \frac{1}{C_f} \\ \frac{-K_v}{L_a} & \frac{-1}{L_a} & \frac{-R_a}{L_a} \end{bmatrix} \tag{3.4}$$

$$\mathbf{B} = \begin{bmatrix} \frac{b}{J_{gk}} & \frac{1}{J_{gk}} & 0 \\ 0 & 0 & \frac{-1}{C_f} \\ \frac{K_v}{L_a} & 0 & 0 \end{bmatrix} \tag{3.5}$$

The state space model of the system is simulated with Matlab/Simulink environment and the comparison of the results with other modeling techniques is given in Section 3.3. Related Matlab code is given in Appendix C.

3.2 Simulink Model

To be sure of the mathematical model that is found by using the state space approach, a Simulink model is also formed and the results of these models are compared in Section 3.3.

The block diagram of the Simulink model is given in Figure 3.4. The model consists of two main blocks called Mechanical System and Electrical System.

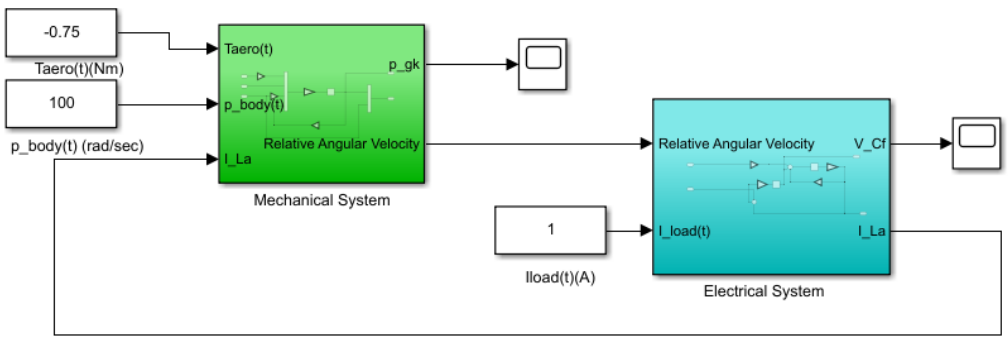

Figure 3.4: Block Diagram of Simulink Model

At the Mechanical System block, the torques on the J_{gk} are taken as input and relative angular velocity between $p_{body}(t)$ and p_{gk} is given as output. The inside of this block is given in Figure 3.5.

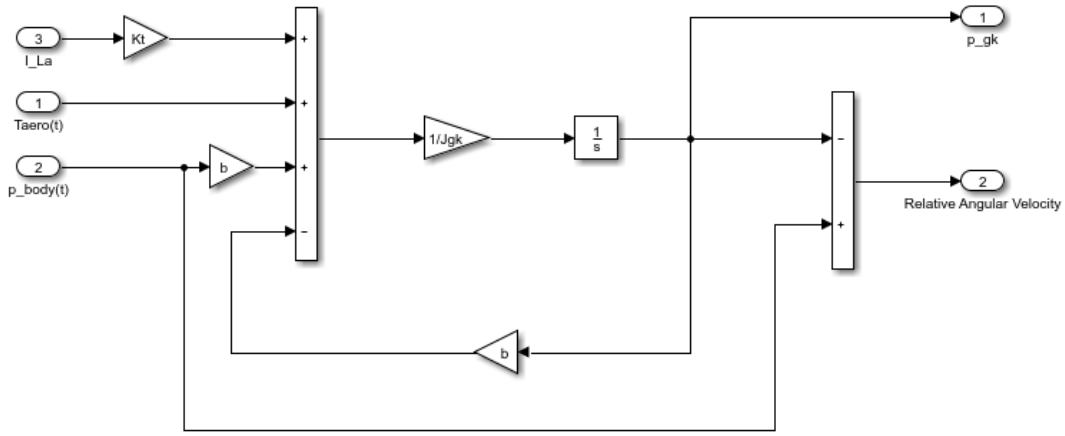

Figure 3.5: Inside of Mechanical System Block

At the Electrical System block, relative velocity and $I_{load}(t)$ are taken as inputs and V_{C_f} and I_{L_a} are calculated and given as outputs. The inside of the Electrical System block is given in Figure 3.6.

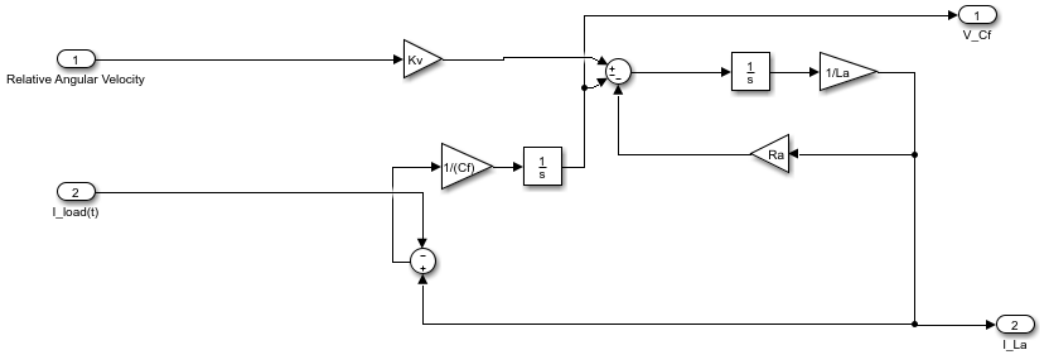

Figure 3.6: Inside of Electrical System Block

3.3 Comparison of the System Models

The Simulink model and the state space model are simulated with the same inputs and the results are compared for system states which are p_{gk}, V_{C_f}, and I_{L_a}. The inputs of the system are given in the list below.

- $p_{body}(t) = 100 rad/sec$
- $T_{aero}(t) = -0.75 Nm$
- $I_{load}(t) = 1A$

The differences between the state variables are given in Figure 3.7. As it is expected, the Simulink model and the state space model are consistent with each other.

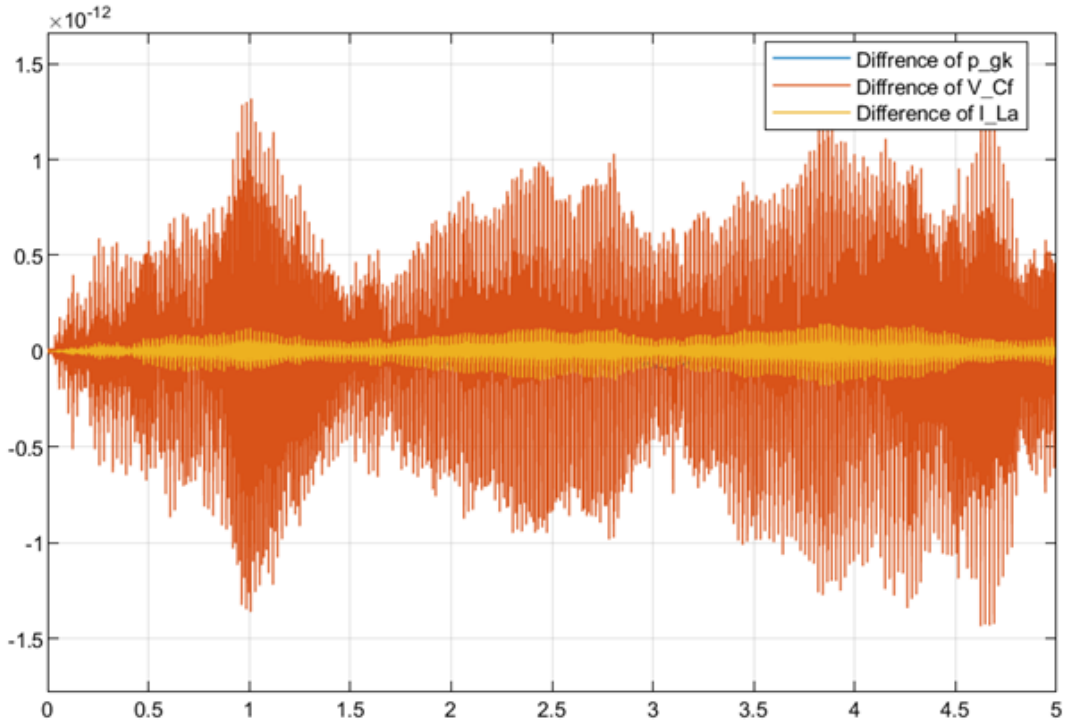

Figure 3.7: The Differences of State Variables Between State Space and Simulink Model

3.4 Transfer Functions Between Inputs and P_{gk}

The free body diagram of the J_{gk} is given in Figure 3.8.

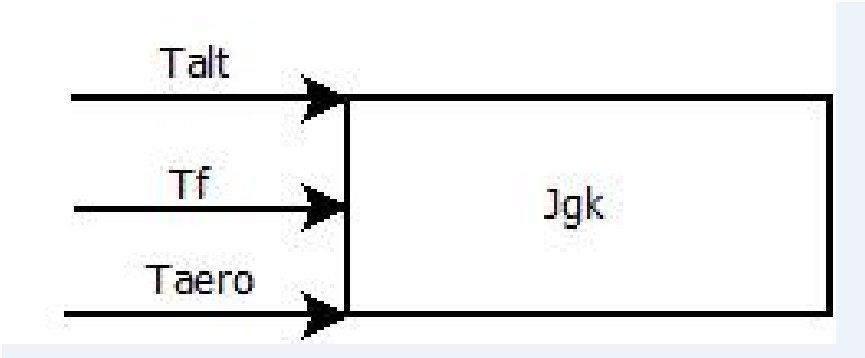

Figure 3.8: Free Body Diagram of J_{gk}

The torques at the J_{gk} are explained in the list below:

- $T_{alt}(t)$ is the torque generated by loading the alternator.

  $T_{alt} = K_t I_a$ and since I_a depends on alternator voltage and $I_{load}(t)$ the function becomes:

  $T_{alt} = T_{alt}(p_{body}(t), T_{aero}(t), I_{load}(t))$

- T_f is the total friction torque on the J_{gk}.

  $T_f = T_f(p_{body}(t), T_{aero}(t), I_{load}(t))$

- T_{aero} is the aerodynamic torque at the system. It is shown here in the positive direction. Due to this, it will have negative values in the simulations.

  $T_{aero} = T_{aero}(t)$

For control purposes, we need to find the transfer function between I_{load} and P_{gk}. To simulate the system correctly, we also need to find the transfer functions between system disturbances and system output. Therefore, we also need to find the transfer functions between P_{body} and P_{gk}, and T_{aero} and P_{gk}.

3.4.1 Transfer Function Between I_{load} and P_{gk}

Derivation of the transfer function between I_{load} and P_{gk} is given in Appendix B. Also, in this appendix consistency of the units is checked for coefficients of the same power of s. The transfer function is given in Equation 3.6.

$$
\begin{aligned}
G_{I_{load}P_{gk}} &= \frac{\beta_0}{\sigma_3 s^3 + \sigma_2 s^2 + \sigma_1 s + \sigma_0} \\
\beta_0 &= \frac{K_t}{L_a C_f J_{gk}} \\
\sigma_0 &= \frac{b}{L_a C_f J_{gk}} \\
\sigma_1 &= \frac{K_v K_t C_f + b R_a C_f + J_{gk}}{L_a C_f J_{gk}} \\
\sigma_2 &= \frac{b L_a C_f + R_a C_f Jgk}{L_a C_f J_{gk}} \\
\sigma_3 &= 1
\end{aligned}
\tag{3.6}
$$

3.4.2 Transfer Function Between T_{aero} and P_{gk}

Derivation of the transfer function between T_{aero} and P_{gk} is given in Appendix B. The transfer function is given in Equation 3.7.

$$
\begin{aligned}
G_{T_{aero}P_{gk}} &= \frac{\beta_2 s^2 + \beta_1 s + \beta_0}{\sigma_3 s^3 + \sigma_2 s^2 + \sigma_1 s + \sigma_0} \\
\beta_0 &= \frac{1}{J_{gk} L_a C_f} \\
\beta_1 &= \frac{R_a}{J_{gk} L_a} \\
\beta_2 &= \frac{1}{J_{gk}} \\
\sigma_0 &= \frac{b}{J_{gk} L_a C_f} \\
\sigma_1 &= \frac{b R_a C_f + K_t K_v C_f + J_{gk}}{J_{gk} L_a Cf} \\
\sigma_2 &= \frac{J_{gk} R_a + L_a b}{J_{gk} L_a} \\
\sigma_3 &= 1
\end{aligned}
\tag{3.7}
$$

3.4.3 Transfer Function Between P_{body} and P_{gk}

Derivation of the transfer function between P_{body} and P_{gk} is given in Appendix B. The transfer function is given in Equation 3.8.

$$
\begin{aligned}
G_{p_{body}(t)P_{gk}} &= \frac{\beta_2 s^2 + \beta_1 s + \beta_0}{\sigma_3 s^3 + \sigma_2 s^2 + \sigma_1 s + \sigma_0} \\
\beta_0 &= \frac{b}{L_a C_f J_{gk}} \\
\beta_1 &= \frac{bR_a + K_t K_v}{L_a J_{gk}} \\
\beta_2 &= \frac{b}{J_{gk}} \\
\sigma_0 &= \frac{b}{L_a C_f J_{gk}} \\
\sigma_1 &= \frac{J_{gk} + bR_a C_f + K_t K_v C_f}{L_a C_f J_{gk}} \\
\sigma_2 &= \frac{R_a J_{gk} + bL_a}{L_a J_{gk}} \\
\sigma_3 &= 1
\end{aligned}
\tag{3.8}
$$

The difference at p_{gk} between the transfer function model and the state space model is compared for the inputs given in Section 3.3. The result is given in Figure 3.9. As expected, the results are consistent with each other.

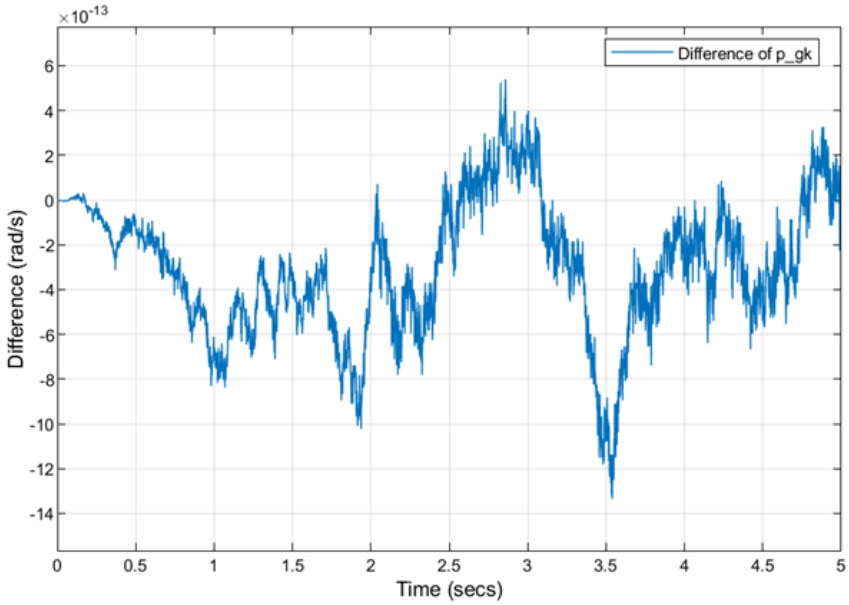

Figure 3.9: Comparison Between Transfer Function Models and State Space Results

3.5 Comparison of the Model Results and Test Results

3.5.1 Comparison of the Open-Circuit Test Results

In this case, p_{gk} is kept at 0 and the speed motor is rotated at different speeds. $I_{load}(t)$ is also kept at 0 and the voltage at the output of the filter V_{C_f} is recorded with respect to $p_{body}(t)$. The comparison of test results and the results of the simulations are given in Table 3.1. In general test and simulation results are consistent with each other but there is an increasing difference with relative velocity. It is possible to update the model for changing K_v but since it is not important for control purposes it is kept constant.

Table 3.1: Open-Circuit Test Results

p_{body} (rad/s)	V_{C_f} Test Result (V)	V_{C_f} Simulation Result (V)	K_v Test Result ($\frac{rad/s}{V}$)
10.5	7.8	7.92	0.74
20.9	16.0	15.7	0.76
31.4	24.6	23.6	0.78
41.9	33.3	31.4	0.79
52.4	41.9	39.3	0.8
62.8	50.4	47.1	0.8
73.3	58.9	55.0	0.8

3.5.2 Comparison of the Closed-Circuit Test Results

In this case, p_{gk} is kept at 0 and the speed motor is rotated at different speeds. $I_{load}(t)$ is also controlled. The voltage at the output of the filter V_{C_f} and T_{gk} is recorded with respect to $p_{body}(t)$ and $I_{load}(t)$.

The comparison of the test results and the results of the simulations is given in Table 3.2. In this table, T_{gk} refers to the total torque generated by the alternator, which means the friction torque is eliminated. In the test results, there is a small change in K_t with changing current. Since the current measurements of the torque motor driver are used to estimate the torque generated by the alternator, the reason behind this can be offset and non-linearity at current measurement.

Table 3.2: Closed-Circuit Test Results

p_{body} (rad/s)	V_{C_f} Test Result(V)	V_{C_f} Simulation Result(V)	T_{gk} (Nm)	I_{load} Test Result(A)	K_t $(\frac{N/m}{A})$
20.9	12.0	12.6	0.37	0.5	0.73
20.9	9.2	9.5	0.72	1	0.72
20.9	6.7	6.4	1.03	1.5	0.69
41.9	28.3	28.3	0.39	0.5	0.77
41.9	25.2	25.2	0.74	1	0.74
41.9	22.2	22.2	1.07	1,5	0.71
41.9	19.6	19	1.44	2	0.72
41.9	16.6	15.9	1.78	2.5	0.71
62.8	44.6	44.0	0.37	0.5	0.75
62.8	41.2	40.9	0.73	1	0.73
62.8	38.0	37.8	1.08	1.5	0.72
62.8	34.8	34.7	1.42	2	0.71
62.8	31.8	31.6	1.75	2.5	0.70
83.8	60.4	59.7	0.37	0.5	0.73
83.8	56.7	56.6	0.72	1	0.72
83.8	53.4	53.5	1.06	1.5	0.71
83.8	50.2	50.4	1.42	2	0.71
83.8	46.5	47.5	1.75	2.5	0.70

CHAPTER 4

CONTROLLER DESIGN

There are many controller types used in servo control and other control problems. Traditional PID controllers are still the most common controller type in the industry despite many other controller types being erased after that [11]. It is possible to tune PID controllers using traditional time and frequency domain approaches such as root locus and bode plots, and in addition to these, it is possible to tune PID controllers on-site by using some automatic tuning algorithms. PID controllers generally give not the best but sufficient results with system dynamics, actuator saturation, and the existence of the disturbance [12].

In general, PID controllers have three terms which are P - proportional with the error signal, I - proportional with the integral of the error signal, and D - proportional with the derivative of the error signal. I - action is generally used for eliminating steady-state error and D - action is generally used for improving the stability of the closed-loop system [13].

The time-domain control input for a PID controller is given in Equation 4.1.

$$u(t) = K_p e(t) + K_i \int e(t)\, dt + K_d \frac{de(t)}{dt} \tag{4.1}$$

Equation 4.1 in the Laplace domain is given in Equation 4.2.

$$U(s) = K_p E(s) + K_i \frac{E(s)}{s} + K_d s E(s) \tag{4.2}$$

Since derivative control amplifies measurement noise [14] it is generally filtered with a first or second-order low pass filter. To prevent amplification of the measurement

noise, derivative action will be the last choice in the controller design.

PID controller structure has some modifications in applications such as cascade control. It is possible to use a cascade control structure if there are more than one measurable states in the system but there is only one of them wanted to be controlled [15]. It is also a suitable control method if it is wanted to eliminate disturbances in the inner loop before they have an impact on the controlled parameter [16]. A cascade control structure is suitable for our system because we want to control the position of J_{gk} and we want to eliminate the impact of the disturbances which are $T_{aero}(t)$ and $p_{body}(t)$. The cascade structure which will be used at the control of the θ_{gk} is given in Figure 4.1. In this block diagram, G_{d1} represents the transfer function between T_{aero} and P_{gk}, G_{d2} represents the transfer function between P_{body} and P_{gk}, and G_u represents the transfer function between I_{load} and P_{gk}.

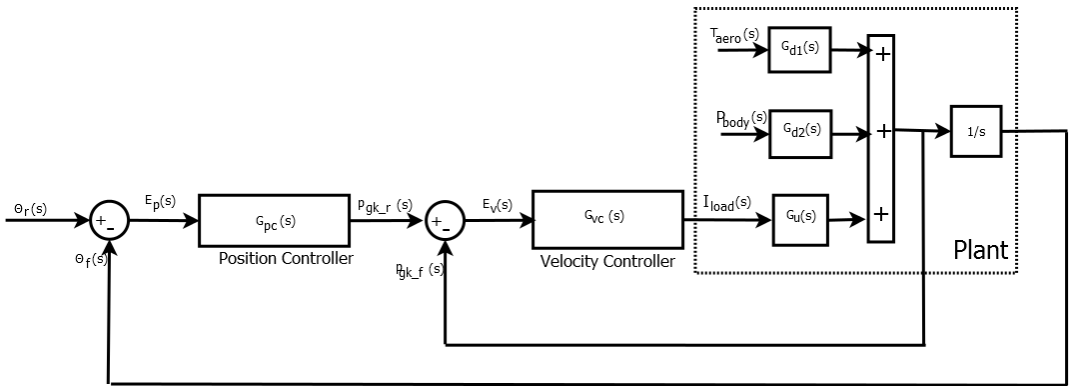

Figure 4.1: Cascade Control Structure

4.1 Requirements for Position and Velocity Controllers

While tuning the cascade controllers, to have sufficient results in the outer loop, the dynamics of the inner loop need to be at least 5 times faster than the outer loop [17]. So, we first need to determine the requirements of the position controller and need to find the requirements of the velocity controller with respect to position controller requirements.

The settling time of the position controller is given as 0.1 s in the literature [10]. Also at this reference, the position, θ_{gk} is examined during flight. And it states that high

dynamics in the reference position is required when the projectile is on the required trajectory, and no need to make guidance to hit the target. Therefore, the position of the fixed canard structure does not need to be controlled after this point and it is allowed to rotate freely. Therefore, a relatively slow cut-off frequency, 4 Hz is sufficient for the position loop. Also, overshoot is not desired at the position loop and steady-state error needs to be zero for a step input. The requirements of the position loop are given in Table 4.1.

Table 4.1: Requirements of the Position Controller

Parameter	Value	Unit
Minimum cut-off frequency	4	Hz
Static position error constant	∞	NA
Maximum settling time	0.1	s
Maximum overshoot	5	%

Requirements of the velocity controller are determined by referencing position loop requirements. The overshoot of the system is not as critical as the position loop. The requirements for the velocity loop are given in Table 4.2.

Table 4.2: Requirements of the Velocity Controller

Parameter	Value	Unit
Minimum cut-off frequency	20	Hz
Static position error constant	∞	NA
Maximum settling time, %5 (T_s)	0.05	s
Maximum overshoot (M_p)	25	%

4.2 Velocity Controller Design

We can determine the locations of the dominant poles by using a second-order system assumption. The standard form of a second-order system transfer function between

input R(s) and output C(s) is given in Equation 4.3. The dynamics of a second-order system can be expressed in terms of ω_n and ζ.

$$\frac{C(s)}{R(s)} = \frac{\omega_n^2}{s^2 + 2\zeta\omega_n s + \omega_n^2} \tag{4.3}$$

We can find ζ by using the maximum overshoot requirement and the relationship given in Equation 4.4.

$$\begin{aligned} M_p &= e^{-(\frac{\sigma}{\omega_d})\pi} \\ \sigma &= \zeta\omega_n \\ \omega_d &= w_n\sqrt{1-\zeta^2} \end{aligned} \tag{4.4}$$

ω_n can be found by using the settling time requirement and the relationship is given in Equation 4.5.

$$\begin{aligned} t_s &= \frac{3}{\sigma} \\ \sigma &= \zeta\omega_n \end{aligned} \tag{4.5}$$

The closed-loop transfer function of the velocity loop and the transfer function between error and reference velocity are given in Equation 4.6.

$$\begin{aligned} G_{clv} &= \frac{P_{gk_f}}{P_{gk_r}} = \frac{G_{vc}G_{I_{load}P_{gk}}}{1 + G_{vc}G_{I_{load}P_{gk}}} \\ \frac{E_v}{P_{gk_r}} &= 1 - \frac{P_{gk_f}}{P_{gk_r}} \\ &= \frac{1}{1 + G_{vc}G_{I_{load}P_{gk}}} \\ E_v &= \frac{P_{gk_r}}{1 + G_{vc}G_{I_{load}P_{gk}}} \end{aligned} \tag{4.6}$$

To choose the velocity controller type, steady-state requirements need to be checked. The Final Value Theorem is a useful tool for checking steady-state requirements in the Laplace domain [11]. This theorem states that the final value of a function can be found by using Equation 4.7.

$$\lim_{s\to 0} sF(s) = \lim_{t\to\infty} f(t) \tag{4.7}$$

Static position error constant is found in Equation 4.8 by using the Final Value Theorem and replacing the Laplace transform of the unit step function, $\frac{1}{s}$, with P_{gk_r} in Equation 4.6.

$$\begin{aligned} \lim_{s\to 0} sF(s) &= \lim_{s\to 0} s\frac{1}{s}\frac{1}{1+G_{vc}G_{I_{load}p_{gk}}} \\ Kp &= \frac{1}{G_{vc}(0)G_{I_{load}p_{gk}}(0)} \end{aligned} \tag{4.8}$$

If Equation 3.6, which gives $G_{I_{load}P_{gk}}$, written in Equation 4.8, static position error constant, K_p becomes:

$$Kp = \frac{1}{(G_{cv}(0))\frac{K_t}{b}} \tag{4.9}$$

To have zero steady-state error for a unit step input, K_p needs to be ∞. Therefore there should be a free integrator at the controller, so a PI controller is a suitable choice. The transfer function of the velocity controller is given in Equation 4.10.

$$G_{vc} = K_{pv} + \frac{K_{iv}}{s} \tag{4.10}$$

Since $p_{body}(t)$ and $T_{aero}(t)$ act on the system as disturbances, it is required to check the steady-state error of the system due to these disturbances. Closed-loop transfer functions between P_{body} and P_{gk} are found in Equation 4.11 by equating reference input to zero.

$$\begin{aligned} P_{gk_f} &= (P_{gk_r} - P_{gk_f})G_{vc}G_{I_{load}P_{gk}} + P_{body}G_{P_{body}P_{gk}} \\ P_{gk_f}(1+G_{cv}G_{I_{load}P_{gk}}) &= P_{body}G_{P_{body}P_{gk}} \\ \frac{P_{gk_f}}{P_{body}} &= \frac{G_{P_{body}P_{gk}}}{1+G_{vc}G_{I_{load}P_{gk}}} \end{aligned} \tag{4.11}$$

Since reference input equated to zero, the error can be found by multiplying the transfer function found in Equation 4.11 with the disturbance P_{body}. Equation of error due to P_{body} is given in Equation 4.12.

$$E_v(s) = -\frac{G_{P_{body}P_{gk}}}{1 + G_{vc}G_{I_{load}P_{gk}}} P_{body} \tag{4.12}$$

If we use Equation 3.6 and Equation 3.8 in Equation 4.12 then apply Final Value Theorem for a step disturbance input the following equation will be found.

$$\begin{aligned} \lim_{s\to 0} sE_v(s) &= -s\frac{G_{P_{body}P_{gk}}(0)}{1 + G_{vc}(0)G_{I_{load}P_{gk}}(0)}\frac{1}{s} = 0 \\ G_{P_{body}P_{gk}}(0) &= 1 \\ G_{I_{load}P_{gk}}(0) &= \frac{K_t}{b} \\ G_{vc}(0) &= \infty \end{aligned} \tag{4.13}$$

Since there is a free integrator at the velocity controller, the disturbance error due to p_{body} is zero at steady-state.

If the same procedure is applied for T_{aero}, Equation 4.14 is found.

$$E_v(s) = -\frac{G_{T_{aero}P_{gk}}}{1 + G_{vc}G_{I_{load}P_{gk}}} T_{aero} \tag{4.14}$$

Using Equation 3.6 and Equation 3.7 in Equation 4.14 and applying Final Value Theorem for a step input to T_{aero} following equation for steady-state error can be found.

$$\begin{aligned} \lim_{s\to 0} sE_v(s) &= -s\frac{G_{T_{aero}P_{gk}}(0)}{1 + G_{vc}(0)G_{I_{load}T_{aero}}(0)}\frac{1}{s} = 0 \\ G_{T_{aero}P_{gk}}(0) &= \frac{1}{b} \\ G_{I_{load}P_{gk}}(0) &= \frac{K_t}{b} \\ G_{vc}(0) &= \infty \end{aligned} \tag{4.15}$$

As it could be expected, the disturbance error due to T_{aero} is zero at steady-state.

Root-Locus of the $G_{I_{load}P_{gk}}$ is given in Figure 4.2. The transfer function has three poles and the locations of the poles are written below.

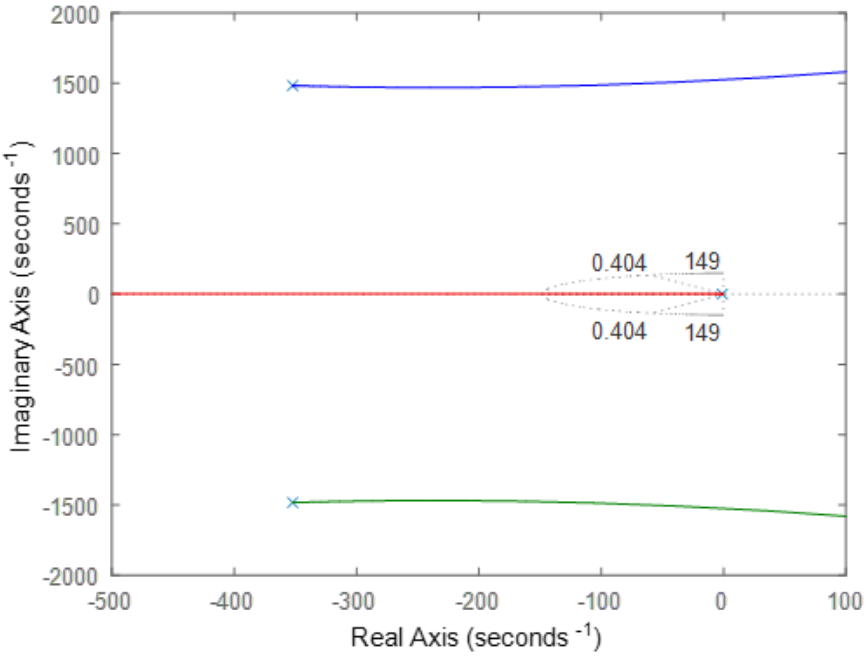

Figure 4.2: Root Locus Graph of $G_{I_{load}P_{gk}}$

- s_1 = -1.04
- s_2 = -352.28 + 1483.20i
- s_3 = -352.28 - 1483.20i

If we make a second-order system assumption, ζ and ω_n can be found by using Equation 4.4 and Equation 4.5. The desired locations of the closed-loop poles are given in Equation 4.16.

$$\begin{aligned} s_1 &= -\zeta\omega_n + \omega_n\sqrt{1-\zeta^2}i = -60 + 136i \\ s_2 &= -\zeta\omega_n - \omega_n\sqrt{1-\zeta^2}i = -60 - 136i \end{aligned} \tag{4.16}$$

PI controller requires the addition of an integrator and a zero to the open-loop transfer function. Since the addition of the integrator shifts the root-locus plot to the right,

zero should be added near the pole to compensate for the effect of the integrator, and the general shape of the root-locus plot will not change. The pole located at -1.03 will move towards to $-\infty$ with increasing gain. The desired locations of the closed-loop poles which are found with the second-order system assumption are less dominant than the pole located at -1.03 if the gain is not high enough to go beyond -60, therefore we need to check the step response of the system to see the effect of the designed controller. With the addition of a zero at -26.98 with an integrator, the root-locus graph of the system is given in Figure 4.3.

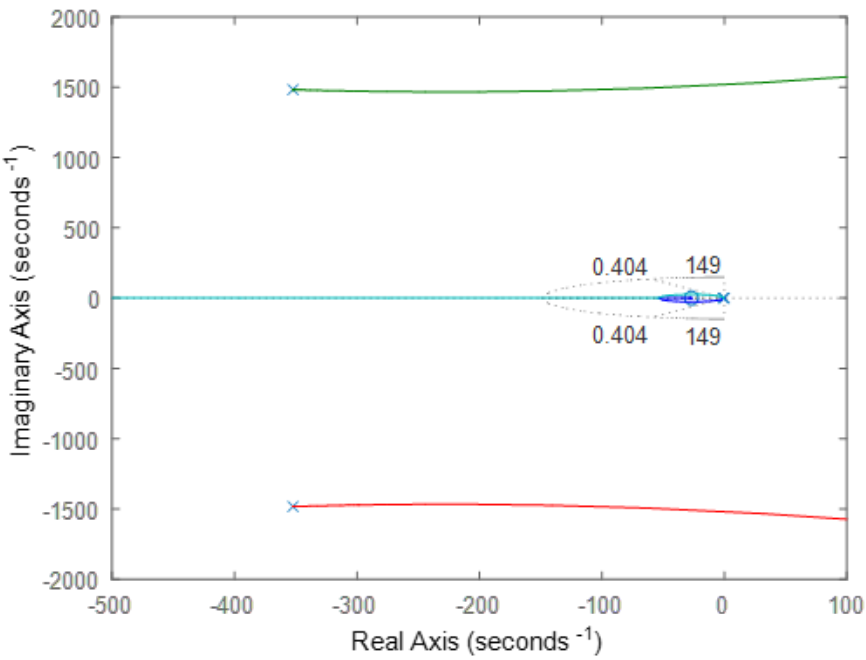

Figure 4.3: Root Locus Graph of Compensated Velocity Loop

If we select gain as 0.29 we would have 2 real poles and 2 complex conjugate poles, so the system becomes a combination of one overdamped and one underdamped system. The pole locations of the closed-loop system are given below.

- s_1 = -33.17
- s_2 = -144.78
- s_3 = -263.82 + 1468.48i

- s_3 = -263.82 - 1468.48i

The step response of the designed controller is given in Figure 4.4 and Bode graph is given in Figure 4.5.

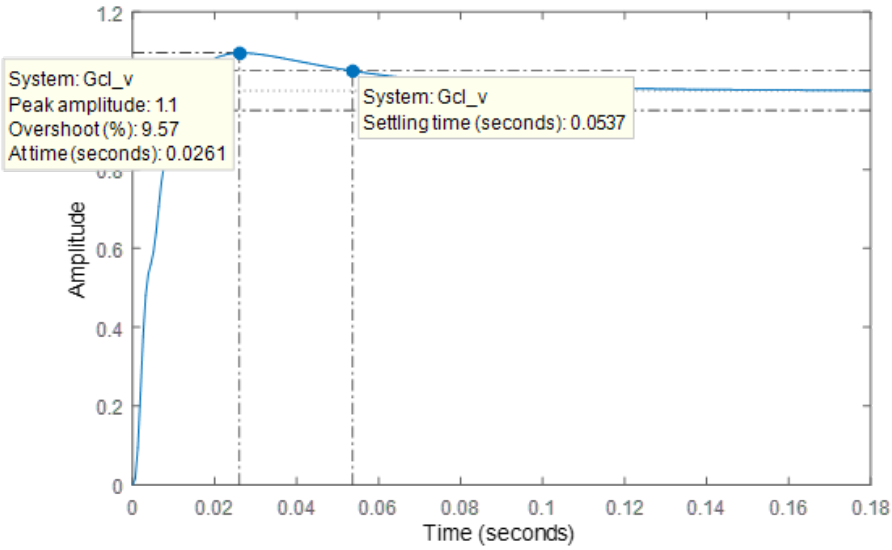

Figure 4.4: Step Response of Velocity Loop

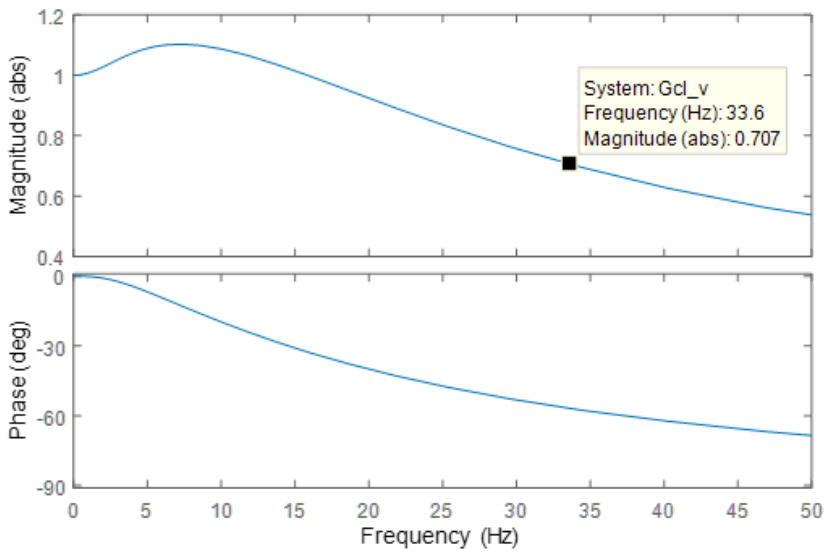

Figure 4.5: Bode Plot of Velocity Loop

Also, we need to check the behavior of the controller to system disturbances. The errors due to step disturbance for T_{aero} and P_{body} are given in Figure 4.6 and Figure 4.7.

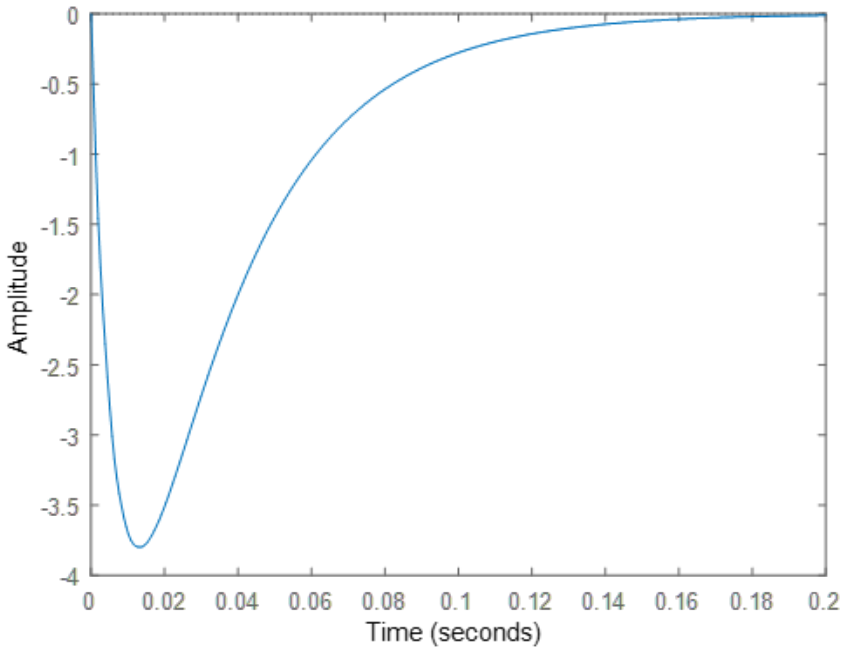

Figure 4.6: Error Due to Step Disturbance at T_{aero}

The errors due to disturbances are zero at steady-state as it is expected.

Since the sources and capability of the actuators are limited, the output of the controller needs to be saturated. Limitation of the controller output can cause overshoot in the system, therefore an anti-windup technique should be used. There are two mainly used integral windup techniques in the literature which are "Back Calculation and Tracking Technique" and "Clamping Technique" [12]. The clamping integration windup technique is selected due to its easy-to-apply algorithm. The windup block is given in Section 4.4.

The comparison of the requirements and designed controller is given in Table 4.3. As can be seen from the table, the designed controller satisfies the requirements.

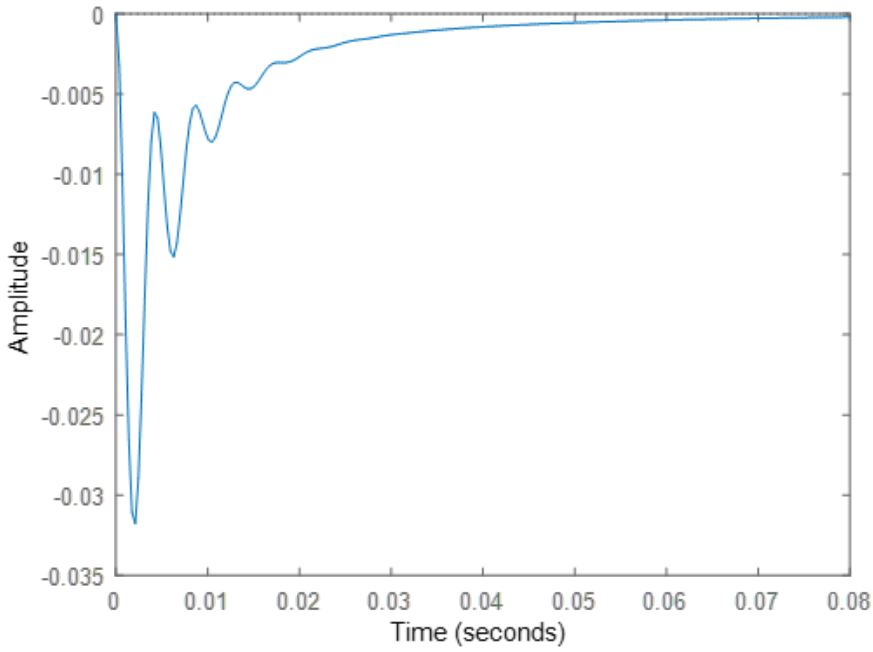

Figure 4.7: Error Due to Step Disturbance at p_{body}

Table 4.3: Result of Velocity Controller Design

Parameter	Requirement	Result	Unit
Minimum cut-off frequency	20	33.6	Hz
Static Position Error Constant	∞	∞	NA
Maximum settling time, %5 (T_s)	0.05	0.05	s
Maximum overshoot (M_p)	25	9.57	%

The transfer function of the velocity controller is given in Equation 4.17.

$$\begin{aligned} G_{vc} &= K_{pv} + \frac{K_{iv}}{s} \\ G_{vc} &= 0.29 + \frac{7.82}{s} \end{aligned} \tag{4.17}$$

4.3 Position Controller Design

Desired closed-loop pole locations of the position loop can be found by making second-order system assumption and using Equation 4.4 and Equation 4.5. The resulting closed loop-pole locations are given below.

$$\begin{aligned} s_1 &= -\zeta\omega_n + \omega_n\sqrt{1-\zeta^2}i = -30.00 + 31.47i \\ s_2 &= -\zeta\omega_n - \omega_n\sqrt{1-\zeta^2}i = -30.00 - 31.47i \end{aligned} \tag{4.18}$$

The open-loop transfer function between input and output position is given in Equation 4.19.

$$G_{olp} = G_{pc}G_{clv}\frac{1}{s} \tag{4.19}$$

Since there is a free integrator in the open-loop transfer function according to Final Value Theorem, the static position error constant is ∞. Therefore there is no need to add an integrator to the controller. Also, the impacts of the disturbances are eliminated in the inner velocity loop, therefore there is no need to check the position controller for disturbance rejection. So, a proportional controller is enough for the position loop.

Root-locus graph for the position loop is given in Figure 4.8.

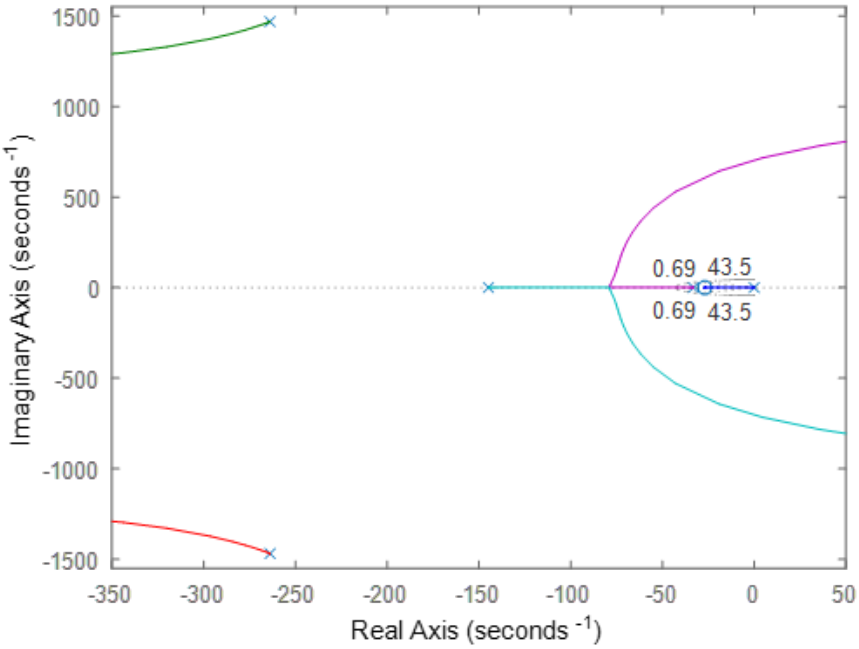

Figure 4.8: Root Locus Graph of G_{olp}

Locations of the open-loop poles are listed below.

- s_1 = 0
- s_2 = -33.17
- s_3 = -144.78
- s_4 = -263.82 + 1468.48i
- s_5 = -263.82 - 1468.48i

As it can be seen from Figure 4.8 one of the closed-loop poles will always remain on the right side of the desired pole locations, therefore the behavior of the system will be dominated by this pole. Gain is adjusted such that the location of this pole will not slow down the system, with a time constant smaller than 0.05. If we adjust the gain to 29.7, the locations of the closed-loop poles are given in the list below.

- s_1 = -21.03
- s_2 = -78.00 + 26.7i
- s_3 = -78.00 - 26.7i

- s_4 = -264.29 + 1466.71i
- s_5 = -264.29 - 1466.71i

The step response of the position loop is given in Figure 4.9 and the Bode plot of the position loop is given in Figure 4.10.

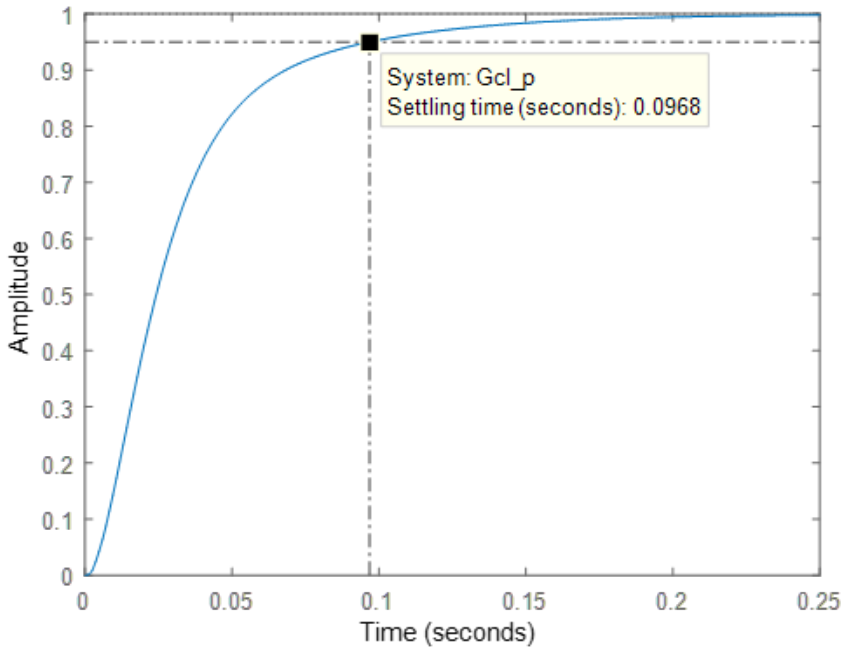

Figure 4.9: Step Response of Position Loop

The comparison of the position controller requirements and designed position controller is given in Table 4.4. Since the system is dominated by the pole near to imaginary axis, the behaviour of the system is like a first-order system.

Table 4.4: Result of Position Controller Design

Parameter	Requirement	Result	Unit
Minimum cut-off frequency	4	6.2	Hz
Static Position Error Constant	∞	∞	NA
Maximum settling time, %5 (T_s)	0.1	0.1	s
Maximum overshoot (M_p)	5	0	%

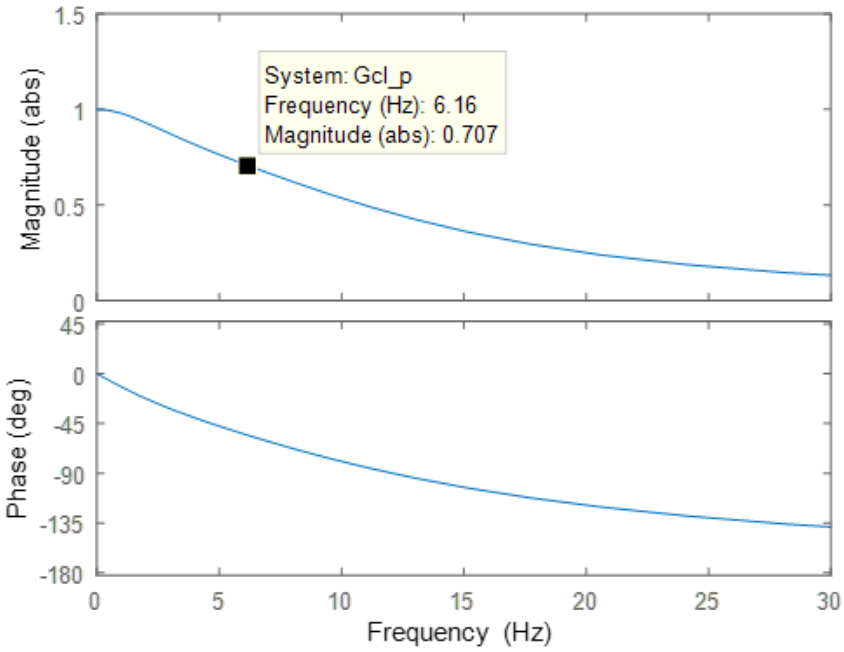

Figure 4.10: Bode Plot of Position Loop

4.4 Test Results and Comparison

The designed controller is simulated with Matlab / Simulink. The block diagram of the simulation is given in Figure 4.11. The block diagram mainly consists of the position and velocity controllers, and the transfer functions represent system dynamics.

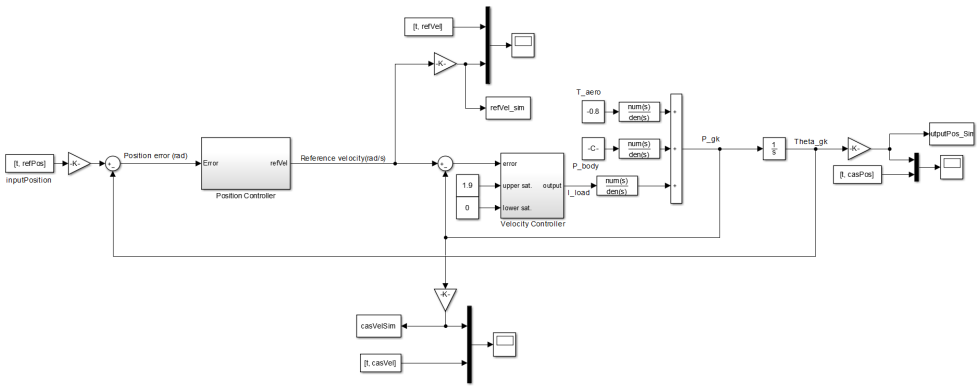

Figure 4.11: Block Diagram of Simulation

Inside of the velocity controller block is given in Figure 4.12. Clamping integration windup algorithm is also implemented in this block with saturation points.

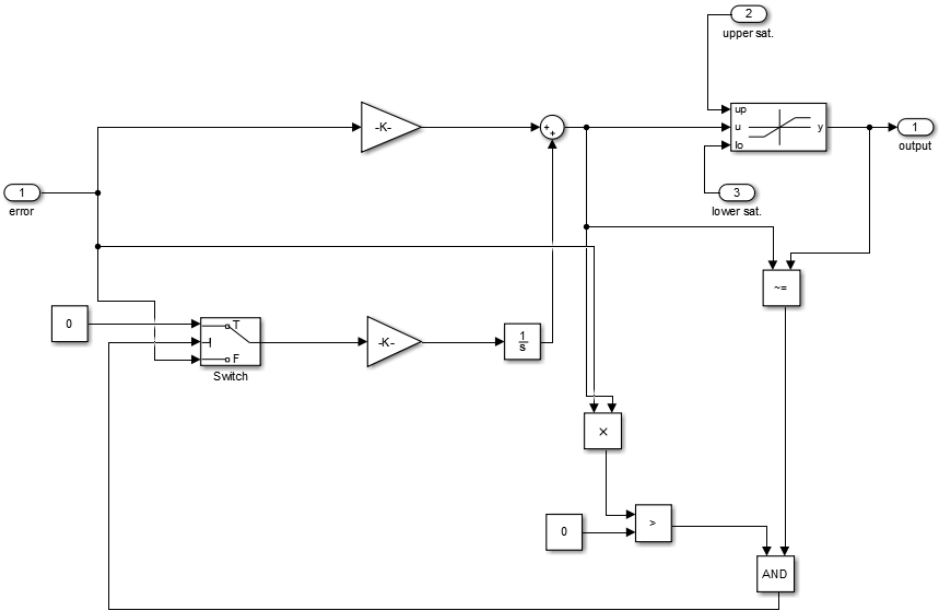

Figure 4.12: Velocity Controller Block

The inside of the position controller block is given in Figure 4.13. This block also contains a part which is called "Calculate Minimum Control Effort" which determines the direction that needs to be rotated to have minimum control effort. Also, the inside of this block is given in Figure 4.14.

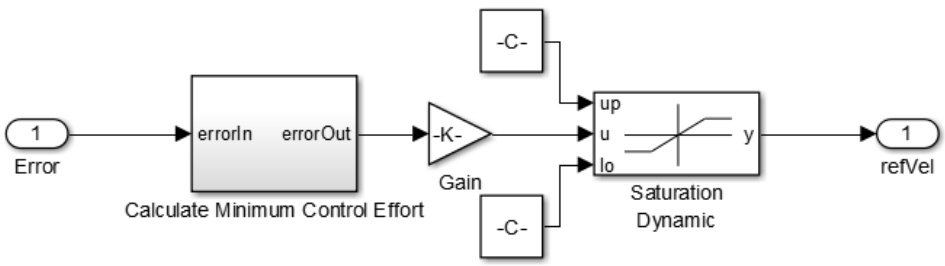

Figure 4.13: Position Controller Block

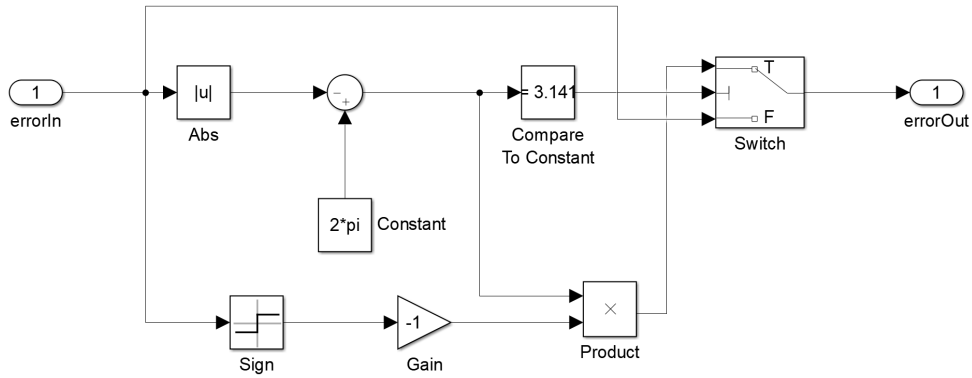

Figure 4.14: Inside of Calculate Minimum Control Effort Block

The inputs and saturation points in the test case are given in Table 4.5.

Table 4.5: Test Conditions

Input	Value	Unit
p_{body}	83.8	rad/s
$p_{gk_{max}}$	20.9	rad/s
$p_{gk_{min}}$	-20.9	rad/s
$I_{load_{max}}$	1.9	A
$I_{load_{min}}$	0	A

4.4.1 Comparison of the Step Test Results

At this test, step input positions are given to the system. Input position, test results, and simulation results are given in Figure 4.15. A zoomed view of this figure is given in Figure 4.16. As it can be seen from these figures, simulation results and test results are consistent with each other. While the system is stationary, there are oscillations at the position in test results that do not exist in simulation results. The reason behind this is measurement error in encoder signals. Also, non-linear friction in the test set-up can cause this situation.

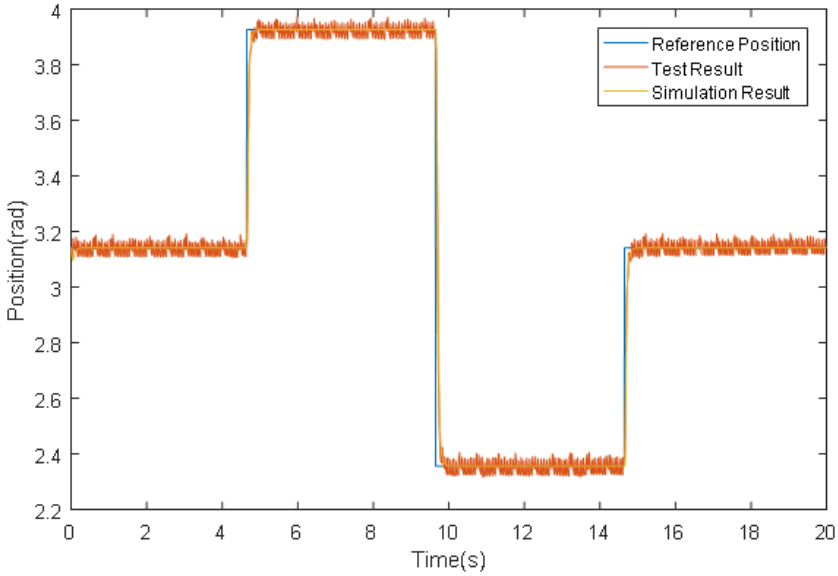

Figure 4.15: Input, Simulation, and Test Results for Step Test

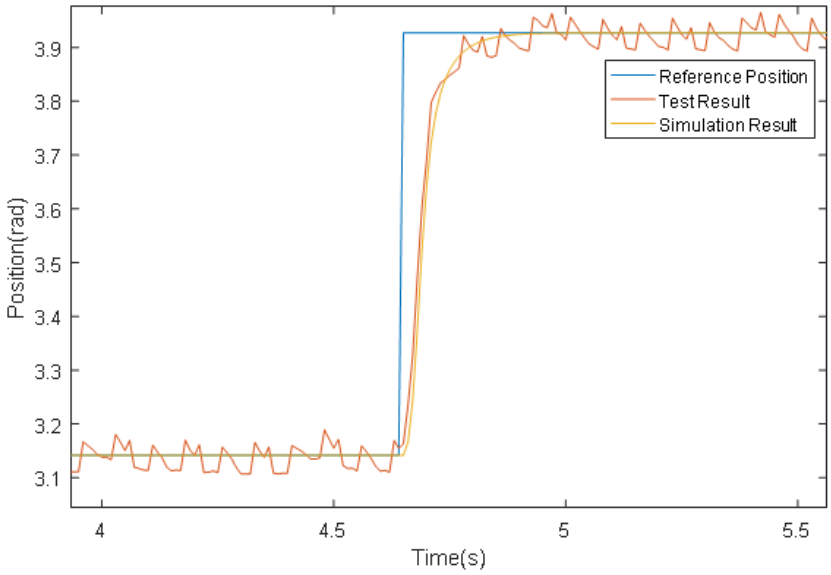

Figure 4.16: Input, Simulation and Test Results for Step Test with Zoomed View

Position controller outputs for test and simulation results are given in Figure 4.17 and a zoomed view of this figure is given in Figure 4.18.

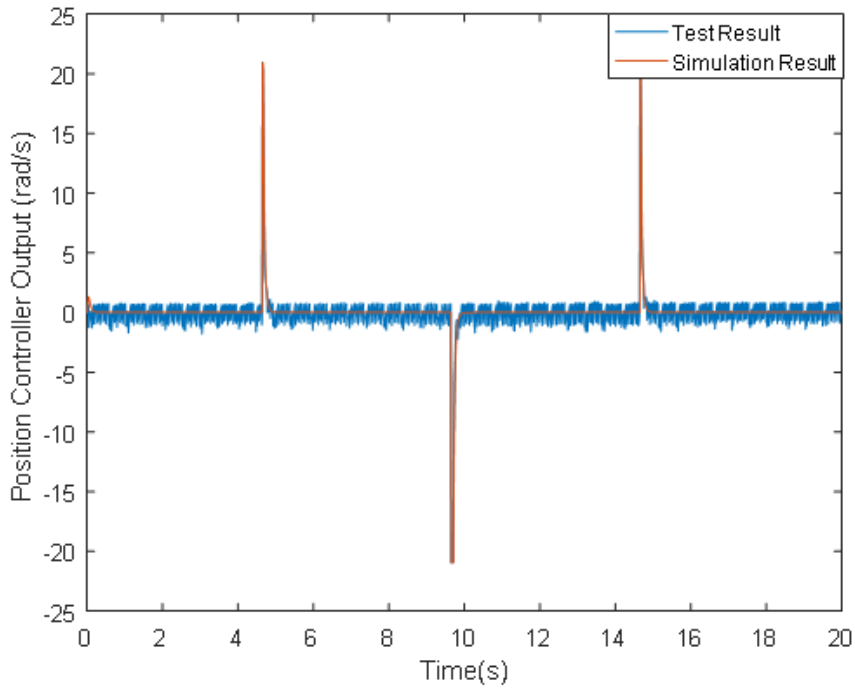

Figure 4.17: Output of Position Controller at Step Test

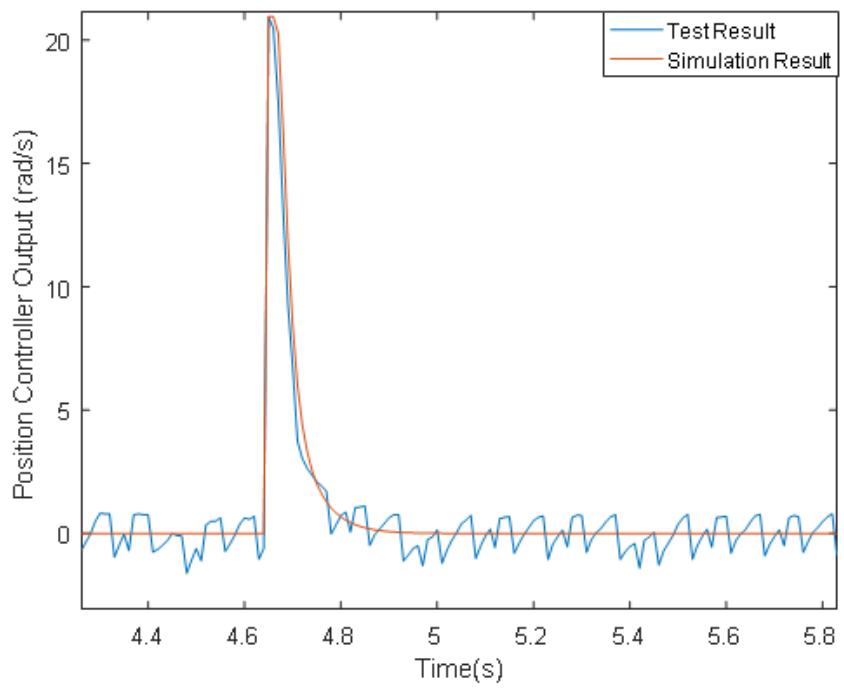

Figure 4.18: Output of Position Controller at Step Test with Zoomed View

p_{gk} at simulation and test results are given in Figure 4.19 and zoomed view of this figure is given in Figure 4.20. The results are consistent with each other when the system is moving but there are fluctuations in test results while the system is stationary. The reasons for this behavior are measurement errors and the resolution of the velocity measurements.

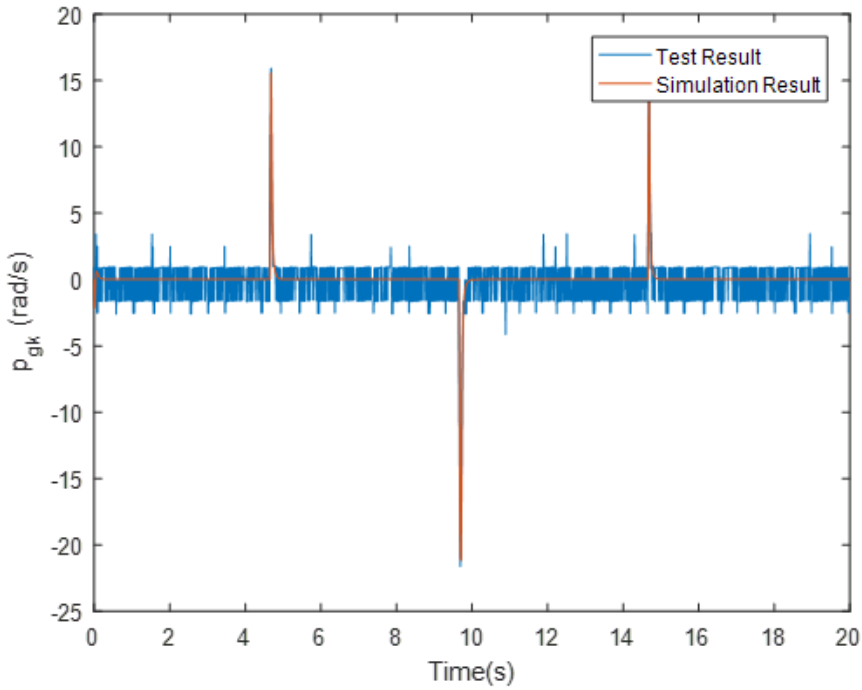

Figure 4.19: p_{gk} at Simulation and Test Results

4.4.2 Comparison of the Chirp Test Results

At this test, a chirp signal is given to the system as a reference position. The amplitude of the given signal is pi/8 and the frequency of the signal is changing from 0.01 to 7.5 Hz in 15s. The sinusoidal signal is applied with pi rad offset. Input position, output position of simulation, and test results for the chirp test are given in Figure 4.21. A zoomed view of Figure 4.21 is given in Figure 4.22. Test results are consistent with simulation results. The amplitude at the cut-off frequency is 3.4192 rad with the addition of pi rad offset. The response of the system reduced to this amplitude after 12.5s. The corresponding frequency is 6.23 Hz which is consistent with design results.

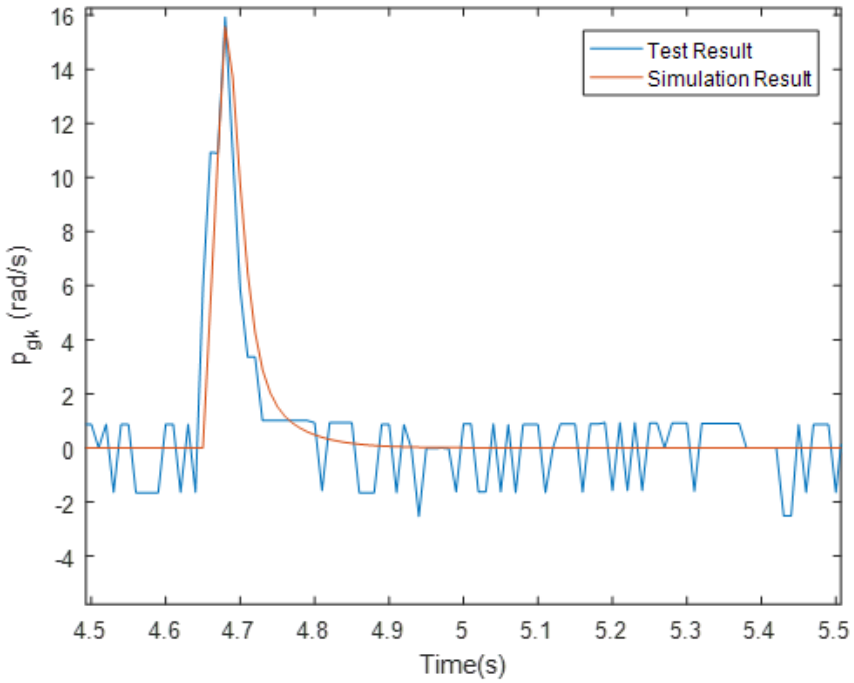

Figure 4.20: p_{gk} at Simulation and Test Results with Zoomed View

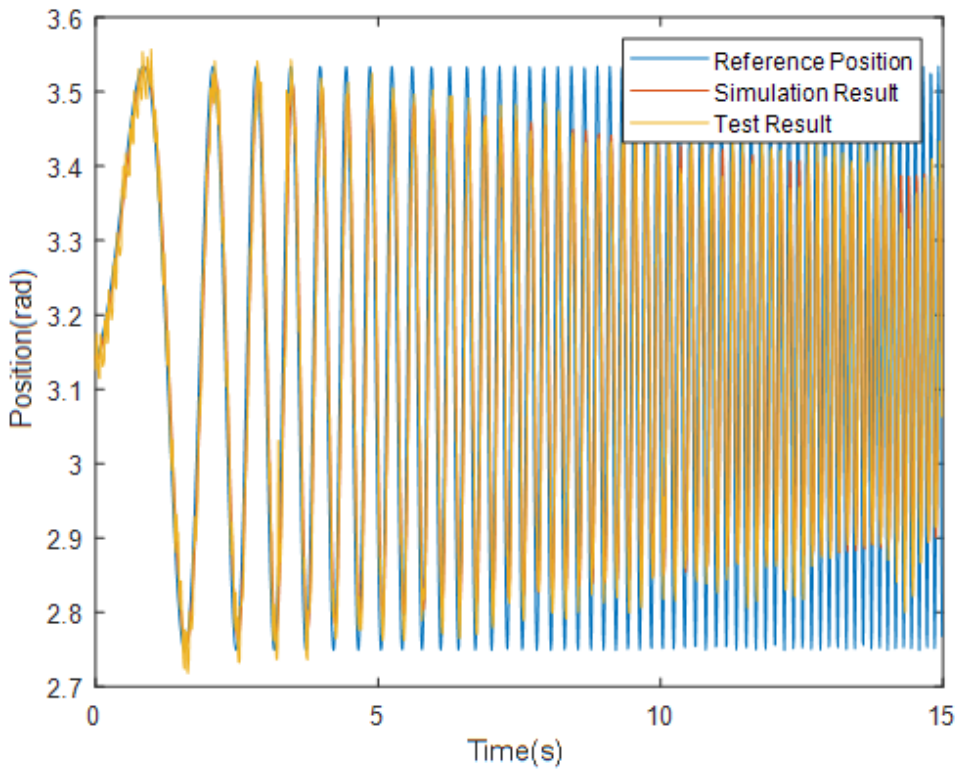

Figure 4.21: Input, Simulation, and Test Results for Chip Test

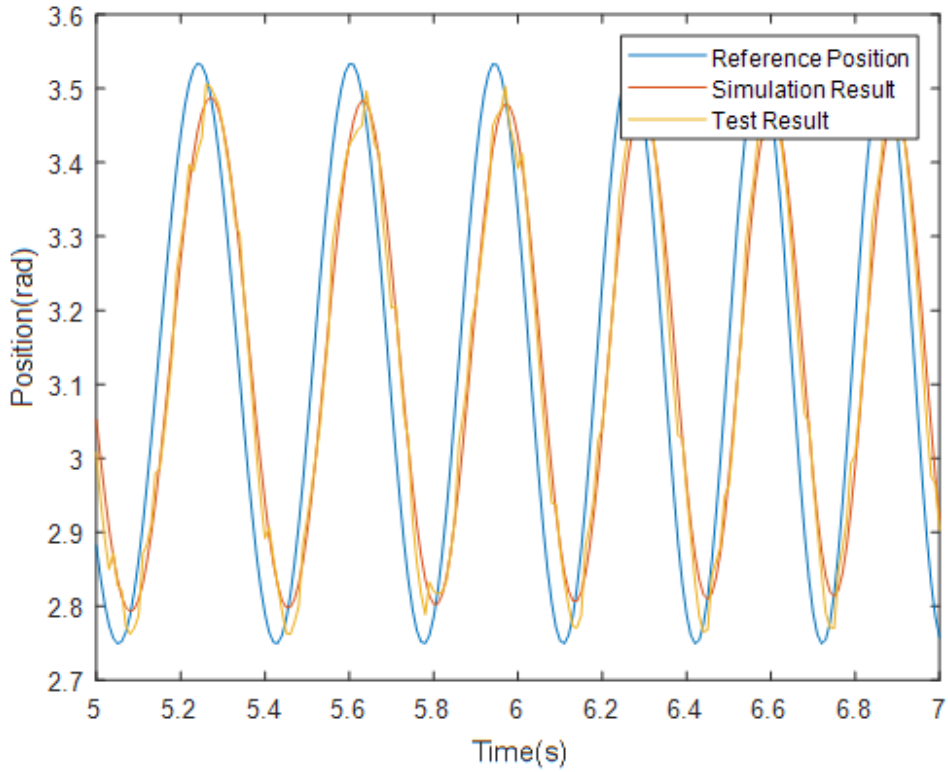

Figure 4.22: Input, Simulation, and Test Results for Chip Test with Zoomed View

The output of the position controller is compared in Figure 4.23. Also, feedback velocities are compared in Figure 4.24. The difference between test results and simulation results is larger than the position difference since as an inner loop, the velocity controller compensates for model uncertainties. The uncertainties mainly come from non-linear Coulomb friction and the change in friction coefficient due to misalignment of center lines of torque and velocity motors.

.

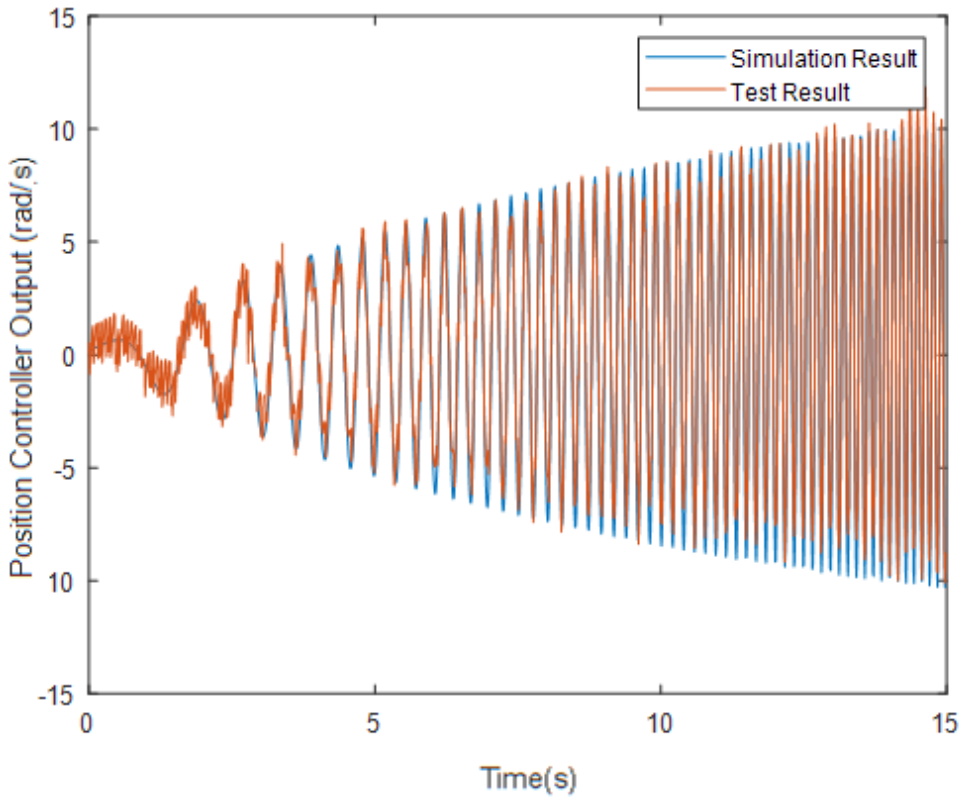

Figure 4.23: Output of the Position Controller Results for Chip Test

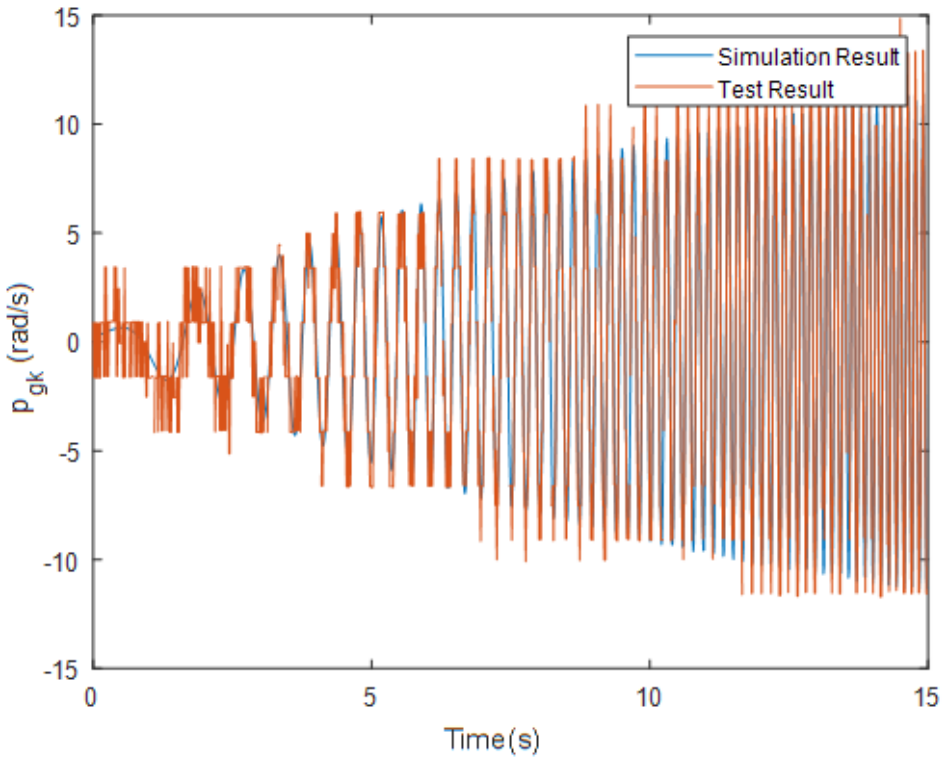

Figure 4.24: p_{gk} at Simulation and Test Results

CHAPTER 5

FLIGHT DYNAMICS OF THE ARTILLERY PROJECTILE

The torques on the fixed canard structure are given in Figure 5.1. It is possible to neglect aerodynamic damping torque while the angular velocity of the guidance kit is low and it is the case when position control is active. As it can be seen from Figure 5.1, the torque in the direction of body angular velocity is the sum of the friction torque and alternator torque. It is possible to control the torque generated by the alternator, but there is no control ability on friction torque. In the opposite direction with body angular velocity, aerodynamic torque is available but it is the output of the flight conditions that we have no control.

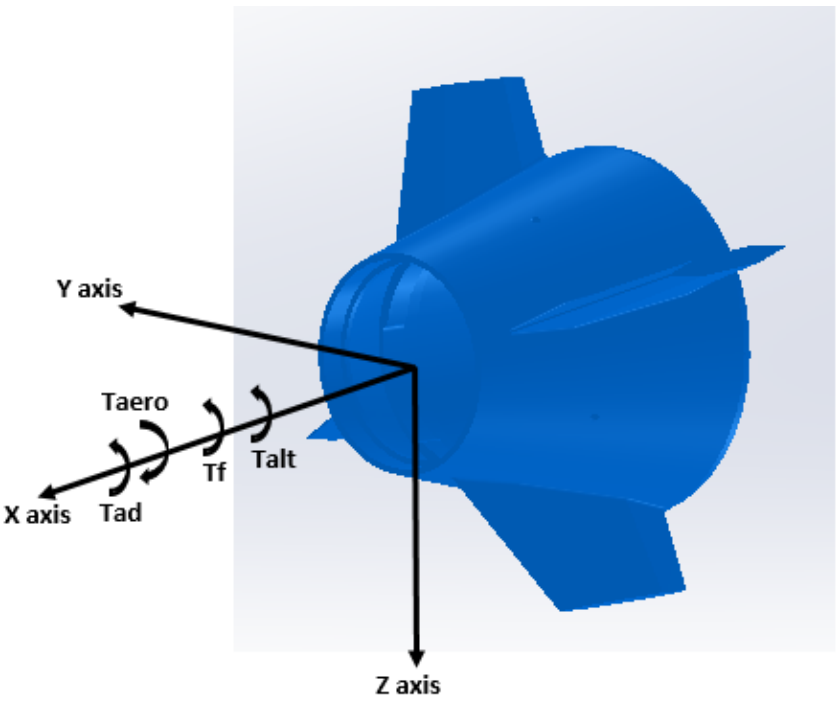

Figure 5.1: Torques on the Guidance Kit

The torques at the +X and -X directions are given in Equation 5.1 and Equation 5.2.

$$T_{+x} = T_{alt} + T_f - T_{aero} \tag{5.1}$$

$$T_{-x} = -T_{alt} - T_f + T_{aero} \tag{5.2}$$

As it can be seen from equations 5.1 and 5.2, friction torque needs to be smaller than aerodynamic torque to have control ability in the -X direction.

To find aerodynamic torque and friction torque in the system, a 6-DOF mathematical model is constructed and the model is extended to 7-DOF.

5.1 Coordinate Frames

As an inertial frame, a flat Earth reference frame is used. This frame does not include the curvature of the Earth's surface. Earth Fixed Reference Frame which is used as the inertial frame is given in Figure 5.2.

There are three possible coordinate systems to make 6-DOF simulation of a spinning projectile. These coordinate systems and their advantages & disadvantages are given in the subsections below.

5.1.1 Body Coordinate Frame

In general, to model an air vehicle, the Body Coordinate System is used. In this coordinate system, the origin is placed at the Cg of the vehicle. X-axis points directly to the nose, Y-axis is perpendicular to X-axis, and Z-axis is found by using the right-hand rule. This frame is rolling with the projectile therefore it has the same angular and linear velocity with the projectile. Since the computational power required to simulate a model directly depends on the highest frequency of the system, the change in roll angle while using the body coordinate frame leads to very long simulation

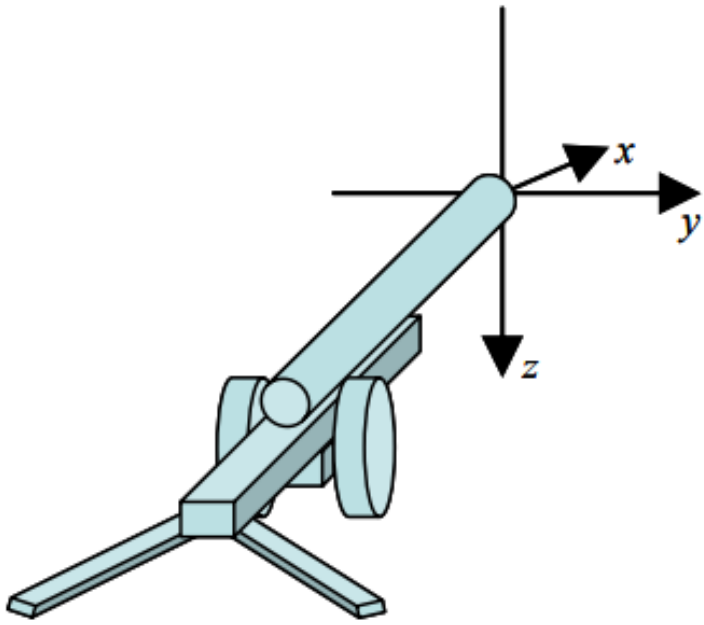

Figure 5.2: Flat Earth Inertial Reference Frame

times. Therefore defining a middle coordinate system that has no rolling motion is useful[9] [18].

The rotational velocity of a reference frame can be expressed by using following ways:

$$\vec{w_F} = \dot{\phi}\vec{x}_3 + \dot{\theta}\vec{y}_2 + \dot{\psi}\vec{z}_1$$

$$\vec{w_F} = p_F\vec{x}_{BR} + q_F\vec{y}_{BR} + r_F\vec{z}_{BR}$$

F subscript indicates "Frame", BR indicates "Body Reference Frame", 1, 2, and 3 indicate "Middle reference frames" in Euler rotation sequences.

No rolling can be guaranteed by using two approaches. The first is having zero roll at angular velocity components of the reference frame and the other is having zero roll rate at the Euler angles [19].

5.1.2 Body Fixed Plane Coordinate System

This coordinate system has no change in the Euler roll angle. In other words, if the initial roll angle is equal to zero, ϕ and $\dot{\phi}$ are zero through to flight time.

The relationship between change in Euler angles and angular velocity of a reference frame is given below [20].

$$\begin{bmatrix} \dot{\phi} \\ \dot{\theta} \\ \dot{\psi} \end{bmatrix} = \begin{bmatrix} 1 & \tan\theta\sin\phi & \tan\theta\cos\phi \\ 0 & \cos\phi & \sin\phi \\ 0 & \sec\theta\sin\phi & \sec\theta\cos\phi \end{bmatrix} \begin{bmatrix} p_F \\ q_F \\ r_F \end{bmatrix} \tag{5.3}$$

If we extract $\dot{\phi}$ from the Equation 5.3:

$$\dot{\phi} = p_F + q_F \tan\theta\sin\phi + r_F \tan\theta\cos\phi \tag{5.4}$$

If we substitute 0 to ϕ and $\dot{\phi}$ in the equation above we get:

$$\begin{aligned} 0 &= p_F + r_F \tan\theta \\ p_F &= -r_F \tan\theta \end{aligned} \tag{5.5}$$

Where q_F and r_F are the same with angular velocities of the body which is written in the Body Fixed Plane coordinate system. So, it is possible to eliminate subscript F and use q, and r for angular velocity components of the Y and Z axis of the coordinate frame.

The advantage of using this reference frame is Y-axis always remains parallel to the Earth's surface. This property will be useful for guidance and control purposes, therefore this reference frame will be used for simulation [9].

5.1.3 Body Non-Spinning Frame

This reference frame assumes that $p_F = 0$. This is simpler than the non-rolling body frame and requires less computational time.

5.2 Mathematical Model and Simulation of 6-DOF Projectile Dynamics

The mathematical model of spin-stabilized projectile dynamics is contracted with some simplifications. The Earth's surface is assumed to be flat which means the curvature of the Earth's surface is neglected. Also, the change in gravitational force with respect to altitude is neglected. In general, aerodynamic coefficients change with changing velocity, incidence angle, and sideslip angle but it is assumed that the coefficients are only changing with respect to Mach number. Since the aim of these simulations is to find aerodynamic torque and body velocity, it is possible to make these assumptions. To use this model for guidance purposes these simplifications need to be included in the model.

5.2.1 6-DOF Dynamical Model in Body Fixed Plane Coordinate System

The explanations and formulas related to forces and moments are given in Appendix G. These equations are also valid in the Non-rolling Body Fixed Plane Reference Frame, but now incidence and sideslip angle need to be calculated in the non-rolling Body Reference Frame.

Linear and angular equation of motion in a non-inertial frame can be written as:

$$\begin{aligned} \mathbf{F} &= m\left(\frac{d\mathbf{V}}{dt}\bigg|_{BFP} + \boldsymbol{\omega}_{BFP} \times \mathbf{V}\right) \\ \mathbf{M} &= \mathbf{I}\frac{d\boldsymbol{\omega}}{dt}\bigg|_{BFP} + \boldsymbol{\omega}_{BFP} \times \mathbf{I}\boldsymbol{\omega} \end{aligned} \tag{5.6}$$

where $\mathbf{V}$ represents the body velocity vector, $\boldsymbol{\omega}$ represents the body angular velocity vector in 6DOF, $\boldsymbol{\omega}_{BFP}$ represents the angular velocity vector of the reference Body Fixed Plane coordinate system, and $\mathbf{I}$ represents the inertia matrix.

The equations which explain the dynamics of the spinning projectile are given in Equation 5.7 and Equation 5.8. In these equations; L, M, and N represent total moment on X, Y, and Z axis; X, Y, and Z represent the total force on X, Y, and Z axis. The derivation of the equations is given in Appendix D.

$$\begin{bmatrix} \dot{p} \\ \dot{q} \\ \dot{r} \end{bmatrix} = \mathbf{I}^{-1} \left(\begin{bmatrix} L \\ M \\ N \end{bmatrix} - \begin{bmatrix} 0 & -r & q \\ r & 0 & r\tan\theta \\ -q & -r\tan\theta & 0 \end{bmatrix} \mathbf{I} \begin{bmatrix} p \\ q \\ r \end{bmatrix} \right) \tag{5.7}$$

$$\begin{bmatrix} \dot{u} \\ \dot{v} \\ \dot{w} \end{bmatrix} = \begin{bmatrix} \frac{X}{m} \\ \frac{Y}{m} \\ \frac{Z}{m} \end{bmatrix} - \begin{bmatrix} 0 & -r & q \\ r & 0 & r\tan\theta \\ -q & -r\tan\theta & 0 \end{bmatrix} \begin{bmatrix} u \\ v \\ w \end{bmatrix} \tag{5.8}$$

The equations which represent the kinematics of the system are given in Equation 5.9 and Equation 5.10. The derivation of these equations is given in Appendix D.

$$\begin{bmatrix} \dot{\theta} \\ \dot{\psi} \end{bmatrix} = \begin{bmatrix} 1 & 0 \\ 0 & \frac{1}{\cos\theta} \end{bmatrix} \begin{bmatrix} q \\ r \end{bmatrix} \tag{5.9}$$

$$\begin{bmatrix} \dot{x_E} \\ \dot{y_E} \\ \dot{z_E} \end{bmatrix} = \begin{bmatrix} \cos\theta\cos\psi & -\sin\psi & \sin\theta\cos\psi \\ \cos\theta\sin\psi & \cos\psi & \sin\theta\sin\psi \\ -\sin\theta & 0 & \cos\theta \end{bmatrix} \begin{bmatrix} u \\ v \\ w \end{bmatrix} \tag{5.10}$$

5.2.2 6-DOF Simulink Model and Results

The overall structure of the Simulink model is given in Figure 5.3. This model is formed by modifying Simulink Aerospace Block-set as it will work at Body Fixed Plane Coordinate System.

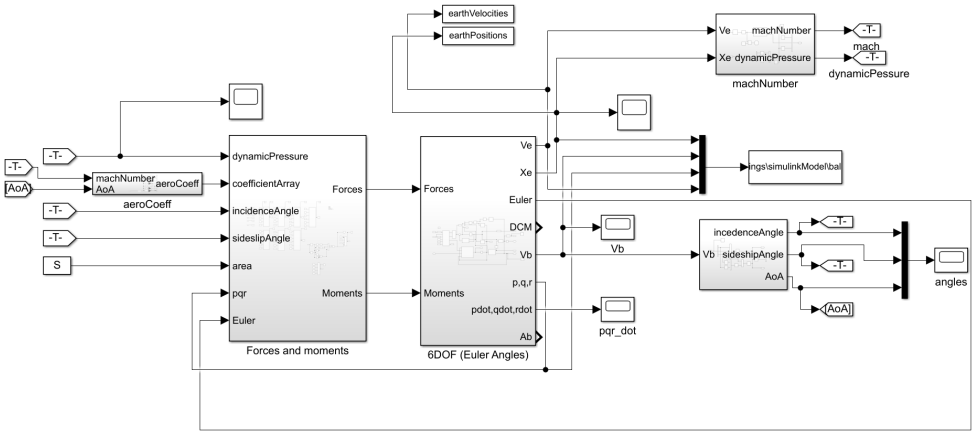

Figure 5.3: Overall Structure of 6-DOF Simulation

The physical properties of the simulated projectile and initial conditions are given in Table 5.1.

Table 5.1: Physical Properties and Initial Conditions

Parameter	Value	Unit
Projectile diameter (d)	155	mm
Projectile mass (M)	43	kg
I_{xx}	0.144	kgm^2
V_i	800	m/s
pqr_i	[1600, 0, -3.5]	rad/sec
Firing elevation angle θ_i	63	°
$I_{yy} = I_{yy}$	1.216	kgm^2

The results of the simulation for the position and velocity of the projectile in the Earth Fixed Reference Frame are given in Figure 5.4 and Figure 5.5. Since the positive z-direction is inside the Earth's surface, position and velocity in Z-axis are given after multiplying with -1 in the figures.

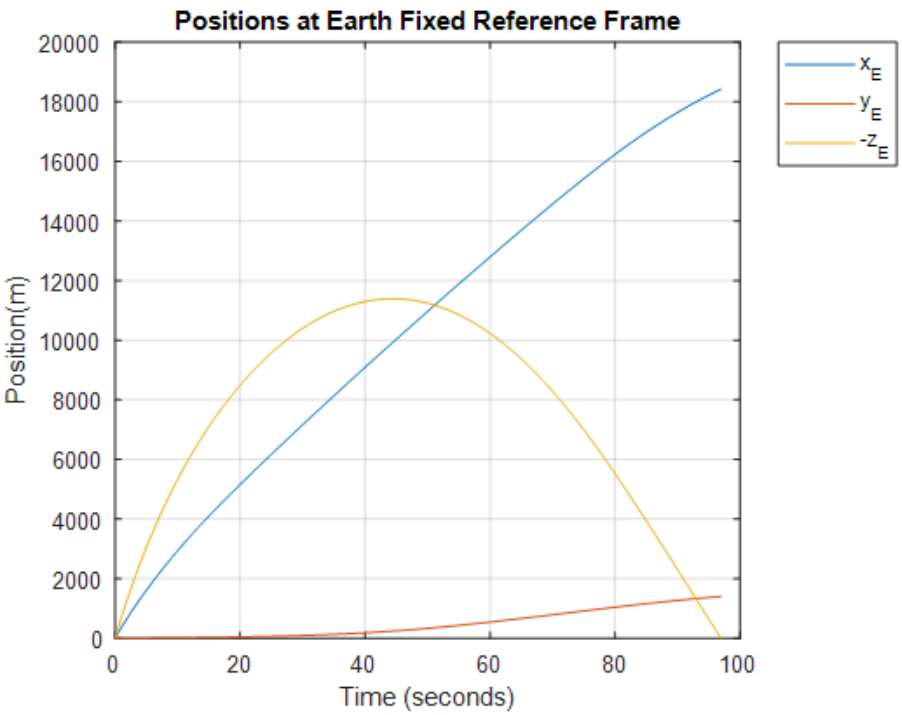

Figure 5.4: Positions at Earth Fixed Reference Frame

5.3 Mathematical Model and Simulation of 7-DOF Projectile Dynamics

Since a projectile with the guidance kit has one additional DOF due to the free rotating part, we need to take this into account. Linear and angular equation of motion for 7-DOF is given in Equation 5.11.

$$\begin{aligned} \mathbf{F}_{7DOS} &= m\left(\frac{d\mathbf{V}}{dt}\bigg|_{BFP} + \boldsymbol{\omega}_{BFP} \times \mathbf{V}\right) \\ \mathbf{M}_{7DOF} &= \mathbf{I}\frac{d\boldsymbol{\omega}_{7DOF}}{dt}\bigg|_{BFP} + \boldsymbol{\omega}_{BFP} \times \mathbf{I}\boldsymbol{\omega}_{7DOF} \end{aligned} \tag{5.11}$$

Equations to represent 7-DOF dynamics of the guided projectile are presented below in Equation 5.12 and Equation 5.13. The reasons for the modifications done to the equation of motion of the system are given in Appendix E.

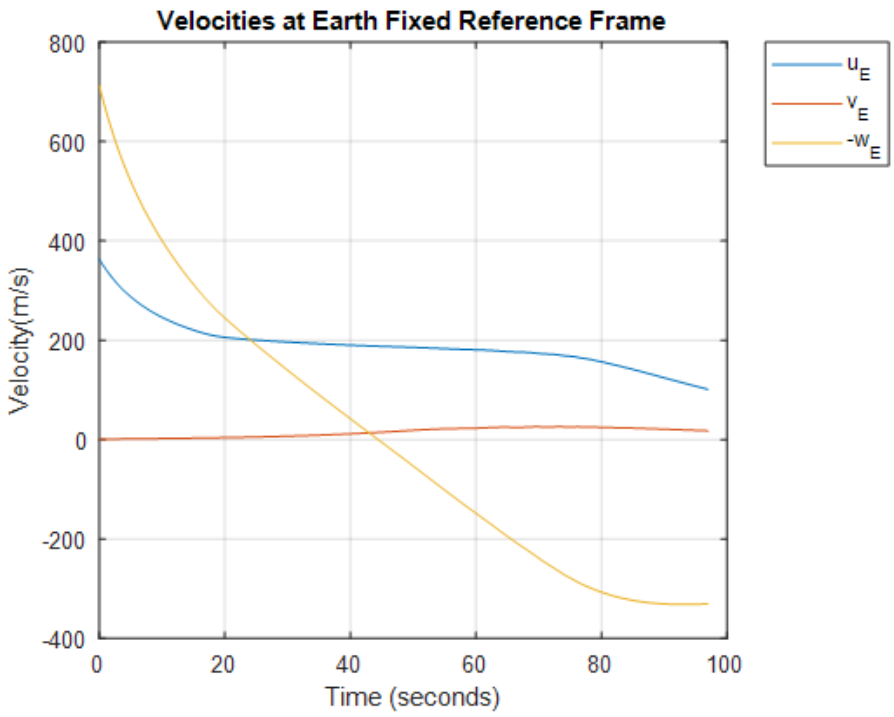

Figure 5.5: Velocities at Earth Fixed Reference Frame

$$\begin{bmatrix} \dot{p}_F \\ \dot{p}_A \\ \dot{q} \\ \dot{r} \end{bmatrix} = \mathbf{I}^{-1} \left(\begin{bmatrix} L_{gk-7DOF} \\ L_{B-7DOF} \\ M_{7DOF} \\ N_{7DOF} \end{bmatrix} - \begin{bmatrix} 0 & 0 & -r & q \\ 0 & 0 & -r & q \\ 0 & r & 0 & r\tan\theta \\ 0 & -q & -r\tan\theta & 0 \end{bmatrix} \mathbf{I} \begin{bmatrix} p_{gk} \\ p_{body} \\ q \\ r \end{bmatrix} \right) \tag{5.12}$$

$$\begin{bmatrix} \dot{u} \\ \dot{v} \\ \dot{w} \end{bmatrix} = \begin{bmatrix} \frac{X_{7DOF}}{m} \\ \frac{Y_{7DOF}}{m} \\ \frac{Z_{7DOF}}{m} \end{bmatrix} - \begin{bmatrix} 0 & -r & q \\ r & 0 & r\tan\theta \\ -q & -r\tan\theta & 0 \end{bmatrix} \begin{bmatrix} u \\ v \\ w \end{bmatrix} \tag{5.13}$$

The inertia matrix in Equation 5.12, **I**, is given in Equation 5.14.

$$\begin{bmatrix} I_{x_{gk}} & 0 & 0 & 0 \\ 0 & I_{x_{body}} & 0 & 0 \\ 0 & 0 & I_y & 0 \\ 0 & 0 & 0 & I_z \end{bmatrix} \tag{5.14}$$

Since the kinematics of the system is not change with the addition of 1-DOF, it is possible to use the same equations with the 6-DOF model. The kinematic equations are given in Equation 5.15 and Equation 5.16.

$$\begin{bmatrix} \dot{\theta} \\ \dot{\psi} \end{bmatrix} = \begin{bmatrix} 1 & 0 \\ 0 & \frac{1}{\cos\theta} \end{bmatrix} \begin{bmatrix} q \\ r \end{bmatrix} \tag{5.15}$$

$$\begin{bmatrix} \dot{x_E} \\ \dot{y_E} \\ \dot{z_E} \end{bmatrix} = \begin{bmatrix} \cos\theta\cos\psi & -\sin\psi & \sin\theta\cos\psi \\ \cos\theta\sin\psi & \cos\psi & \sin\theta\sin\psi \\ -\sin\theta & 0 & \cos\theta \end{bmatrix} \begin{bmatrix} u \\ v \\ w \end{bmatrix} \tag{5.16}$$

5.3.1 Simulink Model and Results

The same initial conditions are used with the 6-DOF model. There is no control input is applied to the guidance kit. It is a ballistic simulation of a projectile with the guidance kit.

There is no significant change in positions and velocities at Earth Fixed Reference Frame since the guidance kit rotates freely through the flight. Positions and velocities at Earth Fixed Reference Frame are given in Figure 5.6 and Figure 5.7.

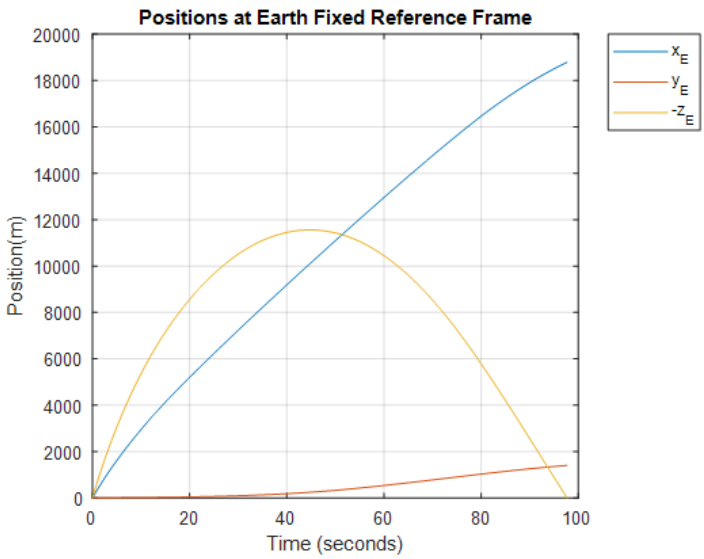

Figure 5.6: Positions at Earth Fixed Reference Frame

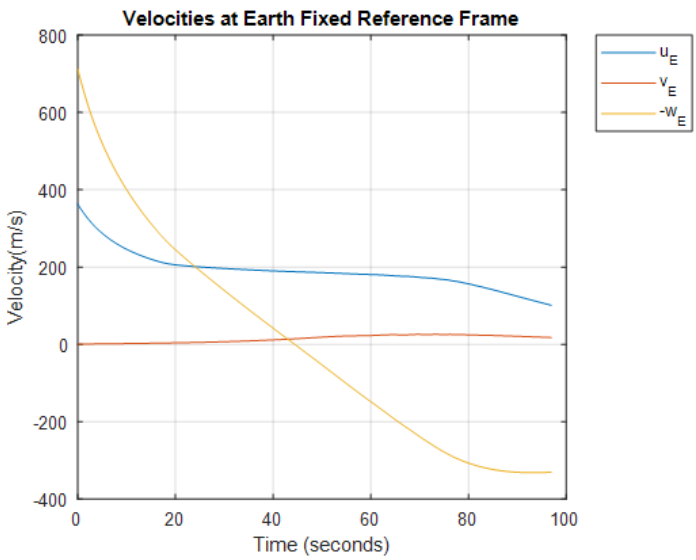

Figure 5.7: Velocities at Earth Fixed Reference Frame

The control forces and moments that arise from the addition of the guidance kit are shown in Figure 5.8 and Figure 5.9. The magnitude of the forces and moments are higher at the beginning of the flight and end of the flight because of the high velocity and air density.

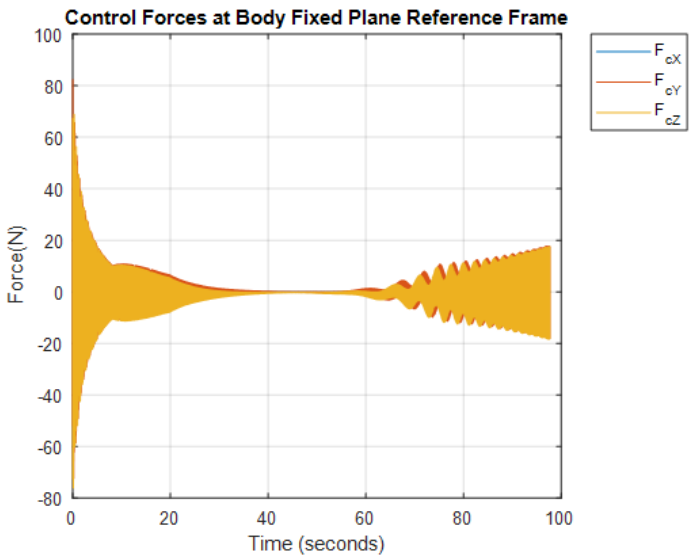

Figure 5.8: Control Forces at Body Fixed Plane Reference Frame

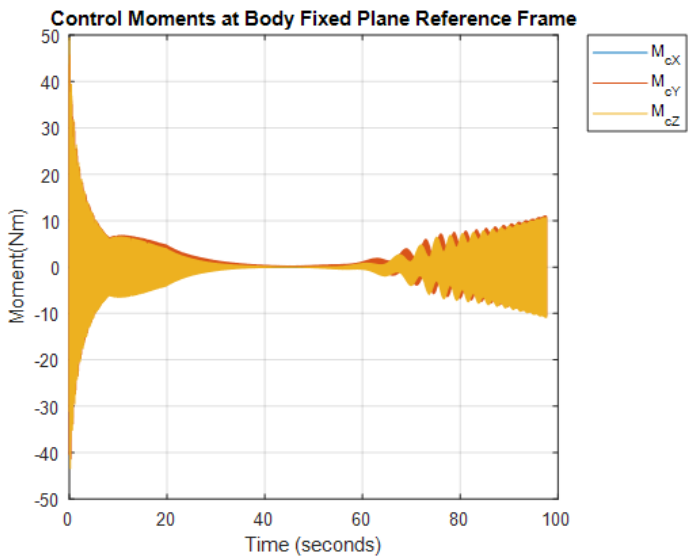

Figure 5.9: Control Moments at Body Fixed Plane Reference Frame

Aerodynamic torque T_{aero} and aerodynamic damping torque T_{ad} on the guidance kit are given in Figure 5.10 and Figure 5.11. In Figure 5.10, the results are given for different firing elevation angles to show the change in the aerodynamic torque. These torques are high at the beginning and end of the flight due to high velocity and air density. At the apogee point, which is the point that has the highest altitude, aerodynamic torque reduces to nearly zero due to low air density and velocity. Therefore, if the proposed guidance kit is used for guidance, the friction torque at this point should be smaller than the aerodynamic torque to have control ability. If the friction torque exceeds the aerodynamic torque at the apogee point, it is needed to begin the guidance after that point.

In Figure 5.10 and 5.11, there are some sudden changes that are not possible physically. The reason is related to the aerodynamic coefficient set that is found in the literature. Since the coefficients are available only at 0.9, 0.95, 1.1, 1.5, and 2.0 Mach, the data set is not comprehensive enough to cover all parts of the flight.

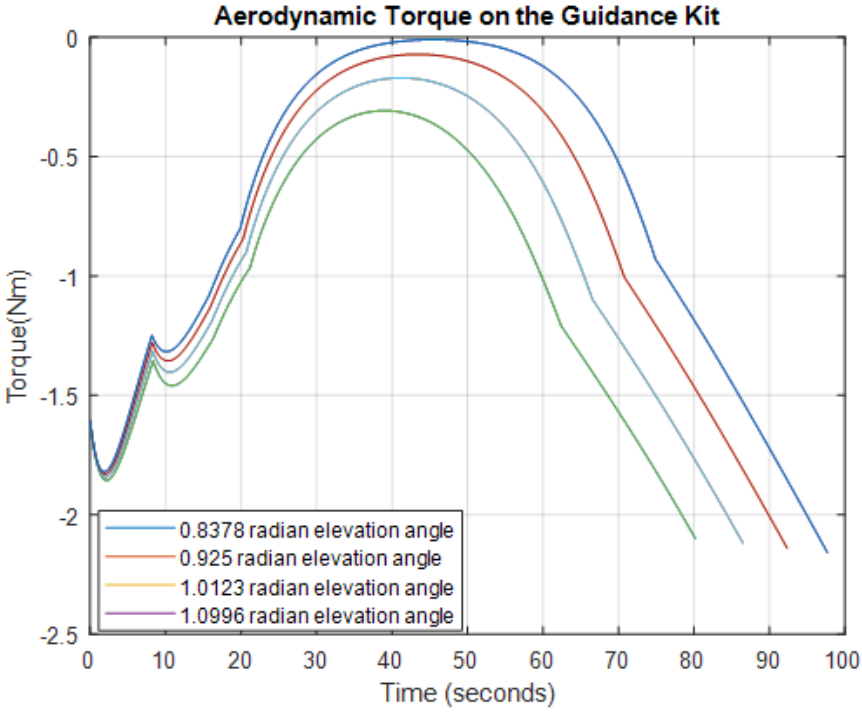

Figure 5.10: Aerodynamic Torque T_{aero} on Guidance Kit

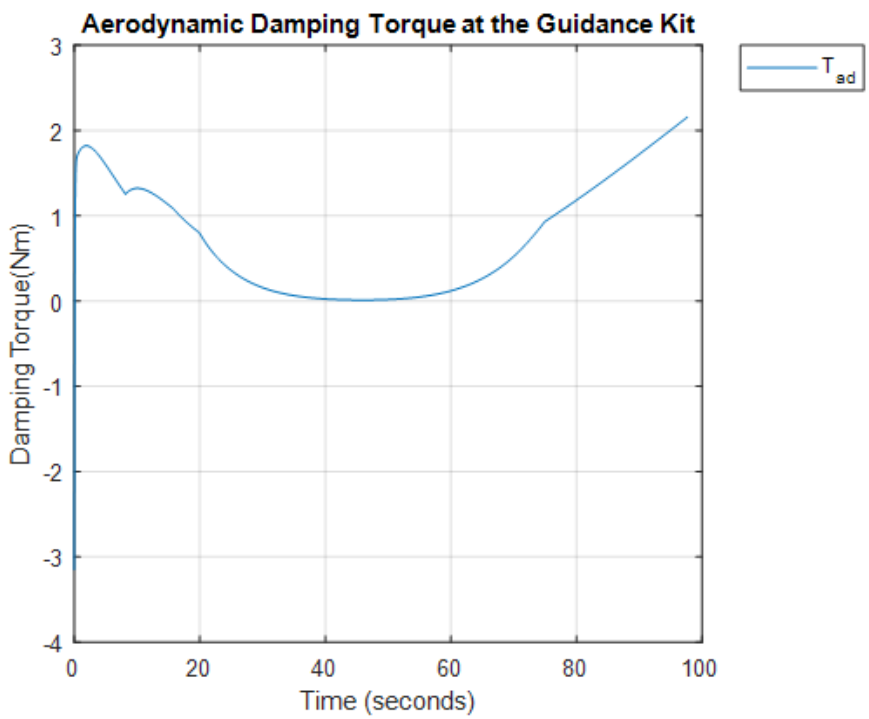

Figure 5.11: Aerodynamic Damping Torque T_{ad} on Guidance Kit

CHAPTER 6

MODIFICATION OF THE CONTROLLER FOR CHANGING AERODYNAMIC TORQUE AND BODY ANGULAR VELOCITY

To have a symmetric response for positive and negative directions, aerodynamic torque needs to be less than or equal to half of the total friction torque generated by body angular velocity and alternator torque. Maximum alternator torque is determined by the current capacity of the programmable DC electronic load which is 8A. Maximum aerodynamic torque is found in Equation 6.1. Friction torque is found by testing for 800 rpm relative angular velocity between alternator rotor and stator.

$$\begin{aligned} T_{aero_{max}} &= \frac{T_{alt_{max}} + T_{friction}}{2} \\ T_{alt_{max}} &= K_t \times 8 = 5.76 \\ T_{friction} &= 0.1 \\ T_{aero_{max}} &= 2.93Nm \end{aligned} \tag{6.1}$$

Minimum aerodynamic torque needs to be bigger than the friction torque generated by body angular velocity. The condition for minimum aerodynamic torque is given in Equation 6.2.

$$T_{aero_{min}} = T_{friction} = 0.1Nm \tag{6.2}$$

Since we have no control over aerodynamic torque, the system can make large overshoots if the aerodynamic torque is not high enough to slow down the system. Large overshoots can lead to instability in the system because of the non-linearity formed by full rotation. To overcome these problems, the designed controller needs to be

modified for low aerodynamic torque inputs.

6.1 Flight Scenario to be Tested

Initial conditions for the selected flight scenario are given in Table 6.1.

Table 6.1: Initial Conditions

Initial Condition	Value	Unit
$V_{initial}$	800	m/s
$pqr_{initial}$	[1600, 0, -3.5]	rad/s
$\theta_{initial}$	0.925	rad

Also, the aerodynamic torque and angular velocity of the projectile body are given in Figure 6.1 and Figure 6.2. The flight scenario is selected such that aerodynamic torque is always bigger than friction torque in order to test the control ability through flight. The maximum angular velocity of the projectile body is nearly 15500 rpm which is 1623.2 rad/s. It is possible to apply aerodynamic torque directly but it is not possible to use body angular velocity directly because of the limits of the speed motor and programmable DC electronic load. Therefore, it is needed to scale body angular velocity. The scale factor is determined by the maximum voltage of the DC electronic load which is 80 V. Scale factor, C, is given in Equation 6.3.

$$\begin{aligned} p_{relative_{max}} &= 80/K_v = 106.6 rad/s \\ p_{body_{max}} &= p_{relative_{max}} - p_{gk_{max}} \\ &= 106.6 - 31.42 = 75.18 \\ C &= 1623/75.18 = 21.6 \end{aligned} \tag{6.3}$$

Since the angular velocity of the projectile body is decreasing with respect to time the scale factor is updated such that the maximum angular velocity of the body is 800 rpm, 83.7 rad/s.

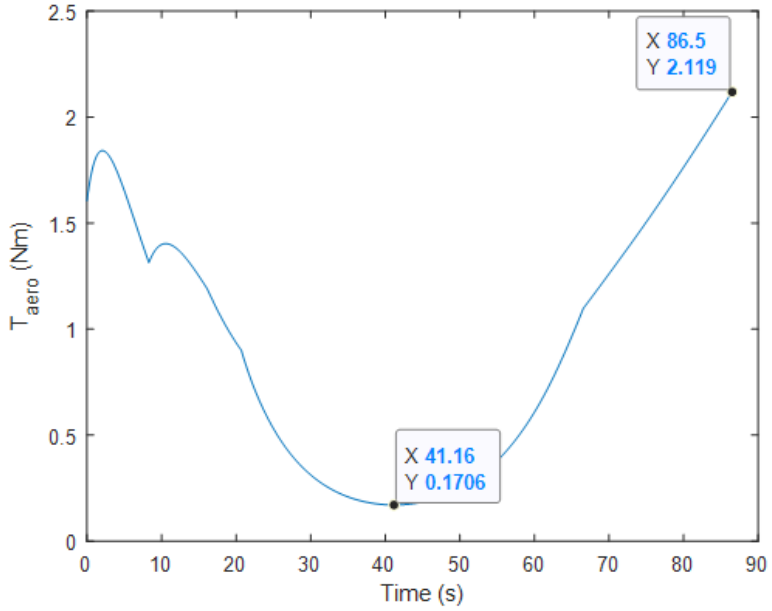

Figure 6.1: Aerodynamic Torque for Selected Flight Conditions

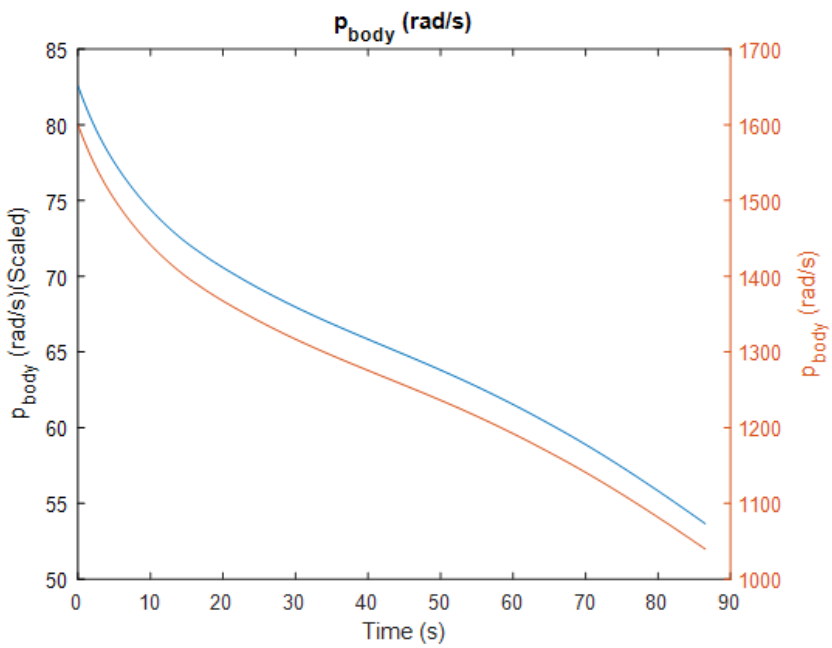

Figure 6.2: Body Angular Velocity for Selected Flight Conditions

6.2 Results for Current Control Structure

Aerodynamic torque and scaled body angular velocity are applied to the simulation with respect to time. The output of the velocity controller is saturated at 8 A to use the full capacity of the system under large torque values. The output of the position controller is saturated at 31.42 rad/s because of the voltage limit of the programmable DC electronic load.

A square wave signal is given to the system through the flight period to examine the response of the system to different torque and body angular velocity conditions. The amplitude of the signal is pi/4 with pi offset. The response of the system for this reference signal is given in Figure 6.3. From Figure 6.3 it is possible to observe that control ability is lost between the 30s and 50s because at this region aerodynamic torque is not enough to slow down the system and therefore the system makes very large overshoots. Also, the comparison of the reference velocity and actual velocity is given in Figure 6.4. It is found that the velocity controller is not capable of responding to the output of the position controller in the direction of aerodynamic torque.

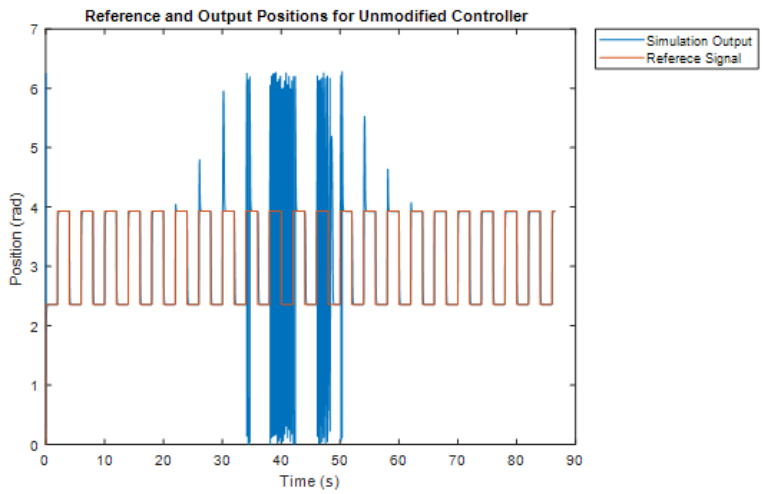

Figure 6.3: Input and Output Positions for Unmodified Controller

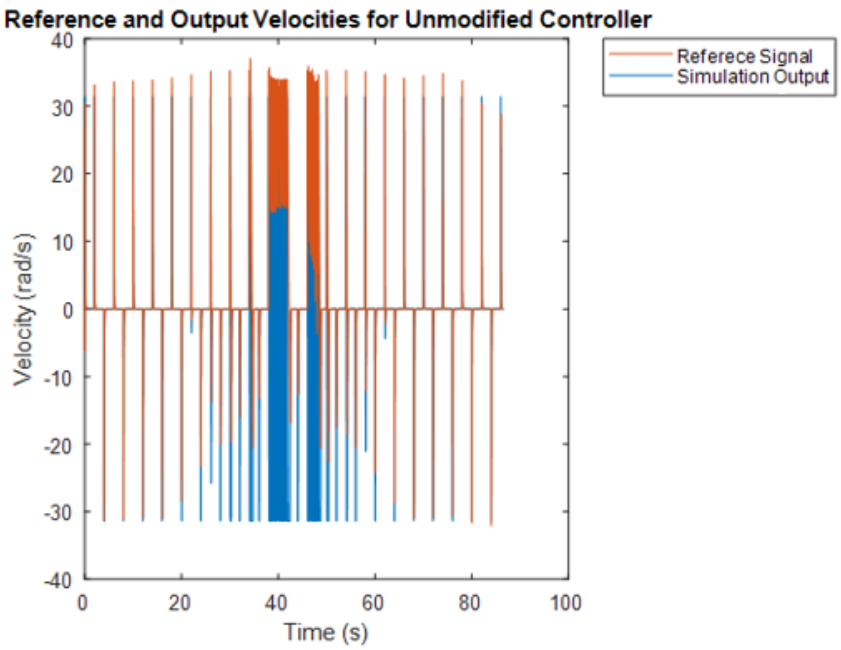

Figure 6.4: Input and Output Velocities for Unmodified Controller

From the results of the unmodified controller it is possible to state that near to apogee point, the response of the system needs to be adjusted in the direction of the alternator torque. Therefore, the total disturbance torques in the system, friction, and aerodynamic torque, need to be observed.

6.3 Disturbance Observer Design

There are two main approaches to observe the disturbance in a dynamic system. The first one is the frequency-domain approach which is designed in the Laplace domain. The second is time-domain approach. The frequency-domain approach only uses the input and output of the system. It is simple to apply but it gives less precise results with respect to the time-domain approach which uses all the state variables to estimate disturbance. Also, being able to use the time-domain approach requires measurement or estimation of all the state variables [21]. In this case, since it is not possible to measure voltage and current at the DC electronic load at the same time, the frequency-domain approach is used. The block diagram of the disturbance observer is given in

Figure 6.5. Since this model uses the inverse of the plant, the input current and output velocity need to be filtered to make the system physically applicable, which means the product of the inverse of the system and the filter transfer function is proper, therefore the system is causal.

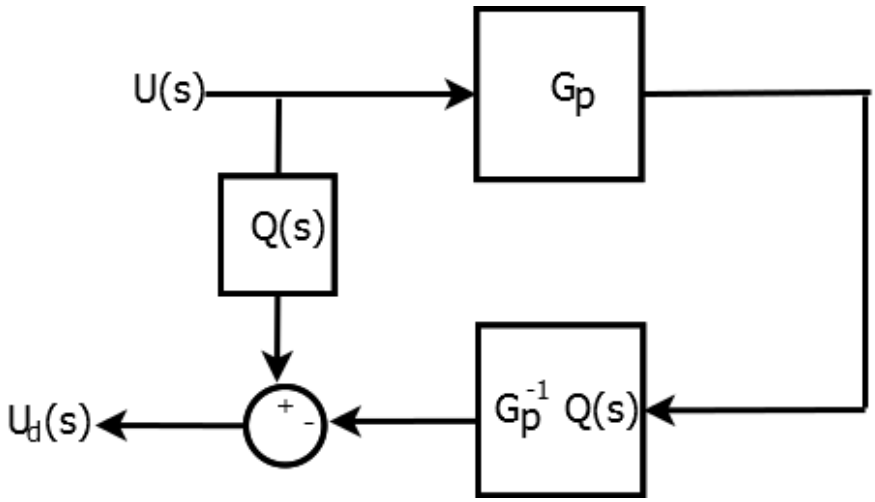

Figure 6.5: Block Diagram of Disturbance Observer

To have a simple filter design and spend less computational time in real-life applications, the transfer function of the plant is simplified. The simplified transfer function between I_{load} and p_{gk} is given in Equation 6.4. A first-order low pass filter is selected such that the rise time of the filter 1.1 seconds and the transfer function of the filter is given in Equation 6.5. A relatively large rise time is selected to filter the inputs due to measurement noise. A relatively large time constant is not a problem for examined system because the change of the aerodynamic torque does not have high-frequency components. The details of the simplification of the transfer function, the comparison of the original transfer function with the reduced transfer function, and the filter design are given in Appendix F.

$$\hat{G} = \frac{588.4}{s + 1.04} \tag{6.4}$$

$$Q = \frac{1}{0.5s + 1} \tag{6.5}$$

The comparison of the designed disturbance observer and real disturbance current at

the system is given in Figure 6.6. Since aerodynamic torque and friction torque do not have high-frequency components, the designed observer is enough for changing the limits of the current and velocity during flight.

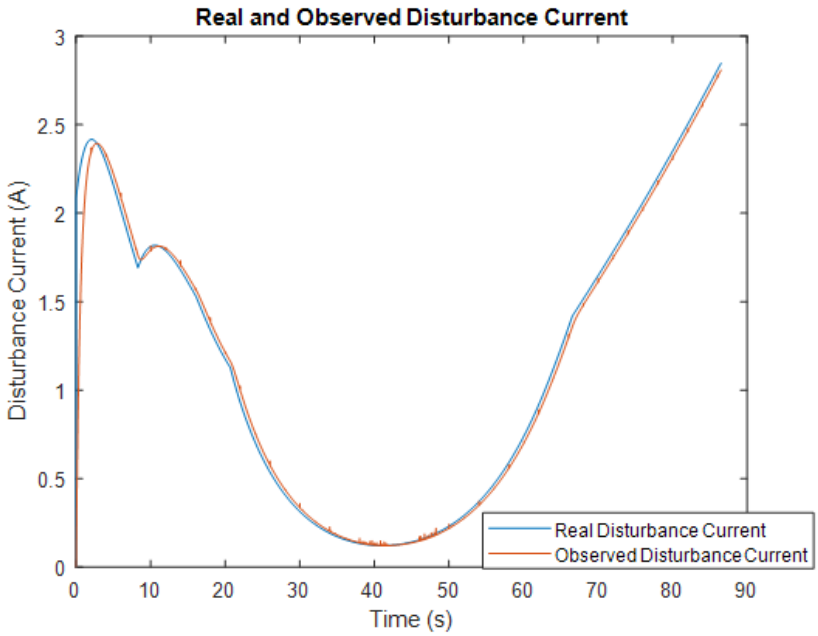

Figure 6.6: Real and Observed Disturbance Current

6.4 Possible Solution Approaches

Three possible solutions are examined to overcome this problem. The first solution is limiting the output of the velocity controller with respect to changing aerodynamic torque such that the control ability of the system is adjusted symmetrically in the direction of the alternator torque and in the direction of the aerodynamic torque. The second solution is limiting the output of the position controller with respect to changing aerodynamic torque. The third solution is the combination of the first and second approaches.

6.4.1 Changing Current Limit Dynamically with Aerodynamic Torque

This approach changes the upper saturation point of the velocity controller with respect to time by using the estimated disturbance current. The saturation point needs to

be equal to two times of the disturbance observer result to have symmetric responses in both directions.

The input and output positions are given in Figure 6.7. Also, the output of the velocity controller with the result of the disturbance observer is given in Figure 6.8. It is possible to observe from these figures that the system is controllable throughout the flight. The control ability is always equal in positive and negative directions but since we have no control at the velocity limit it is not possible to control the system without having overshoots due to the low current limit and the high velocity limit which is 300 rpm. It is possible to observe this situation at the time between 35s and 55s.

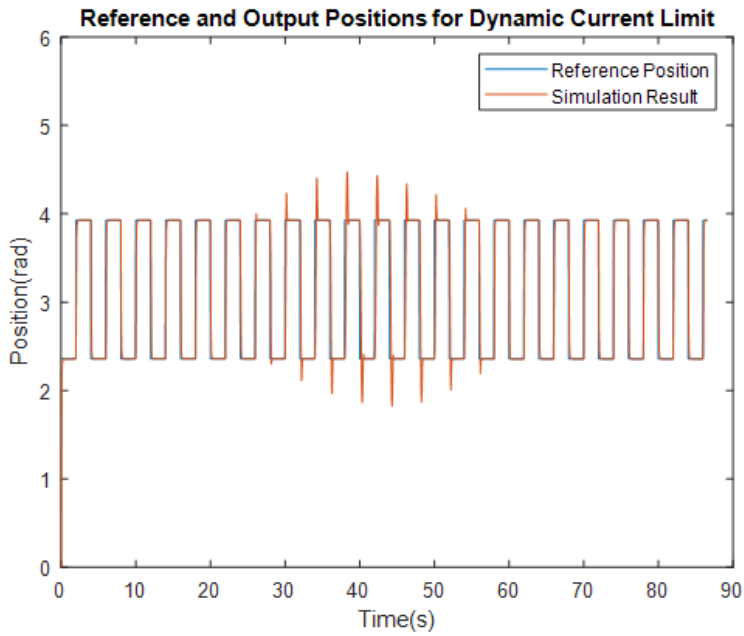

Figure 6.7: Input and Output Positions for Dynamic Current Limit

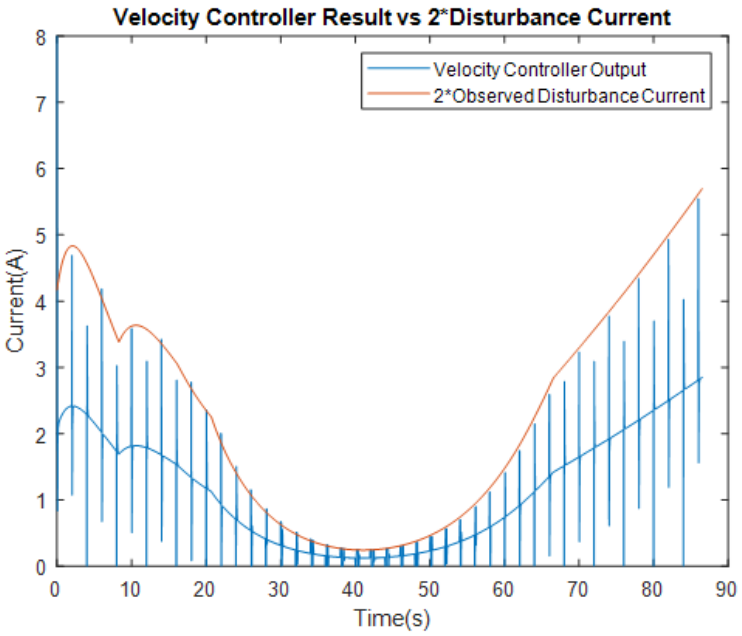

Figure 6.8: Velocity Controller Result for Dynamic Current Limit and Observed Current

6.4.2 Changing Velocity Limit Dynamically with Aerodynamic Torque

This approach changes the upper and lower saturation points of the position controller with respect to time by using the result of the disturbance observer. The maximum value of the velocity limit at the minimum aerodynamic torque is found by using the simulation of the system and which is 5.2 rad/s for 0.2 A disturbance current. The maximum and minimum limit of the position controller is scaled such that the output is equal to 5.2 rad/s for 0.2 A disturbance current. The velocity scale factor is given in Equation 6.6. To be inside of the capability of the load resistor, the output of the position controller is saturated at 31.4 rad/s if the output of the velocity limit found by using disturbance current is higher than this.

The input and output positions for this approach are given in Figure 6.9. It can be observed from Figure 6.9 that it is possible to control the system through to flight time without having any overshoot. Also, the output of the velocity controller is given in Figure 6.10 and a closed view of this figure is given in Figure 6.11. As it can be seen from Figure 6.11, the system has asymmetric responses to both sides since

the changes of the reference angle at 40th s and 42th s are the same but the shape of the current demands are different.

$$VSF = \frac{5.2(rad/s)}{0.2(A)} = 26\frac{rad}{A\ s}$$
$$VL = 26\frac{rad}{As}\hat{I}(A)$$

Where VSF stands for "Velocity Scale Factor", and VL stands for "Velocity Limit". (6.6)

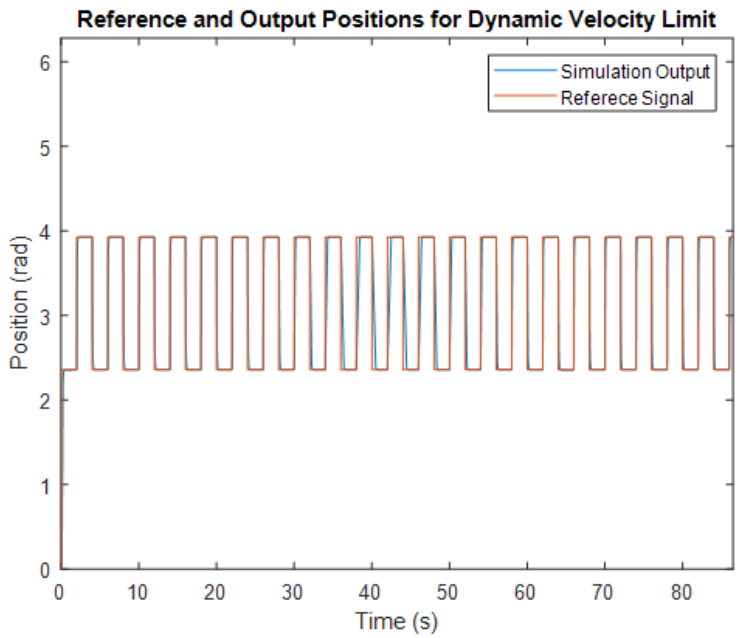

Figure 6.9: Input and Output Positions for Dynamic Velocity Limit

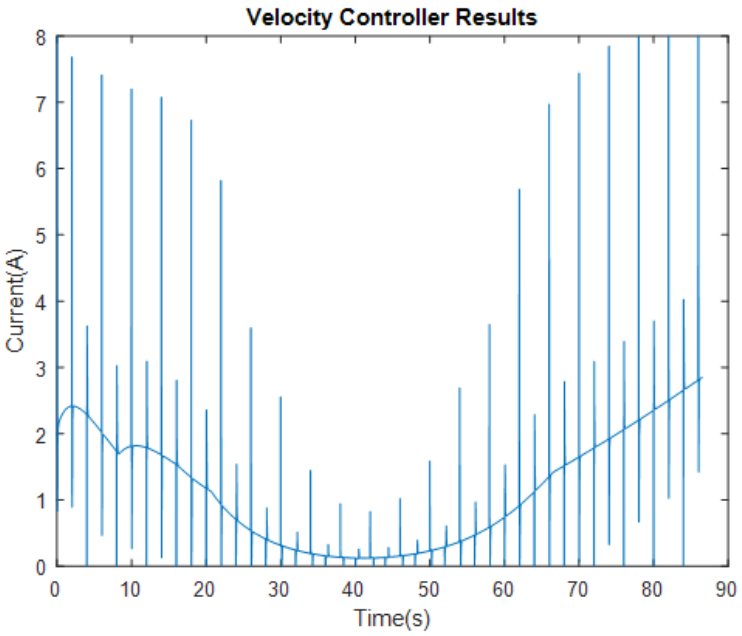

Figure 6.10: Velocity Controller Result for Dynamic Velocity Limit

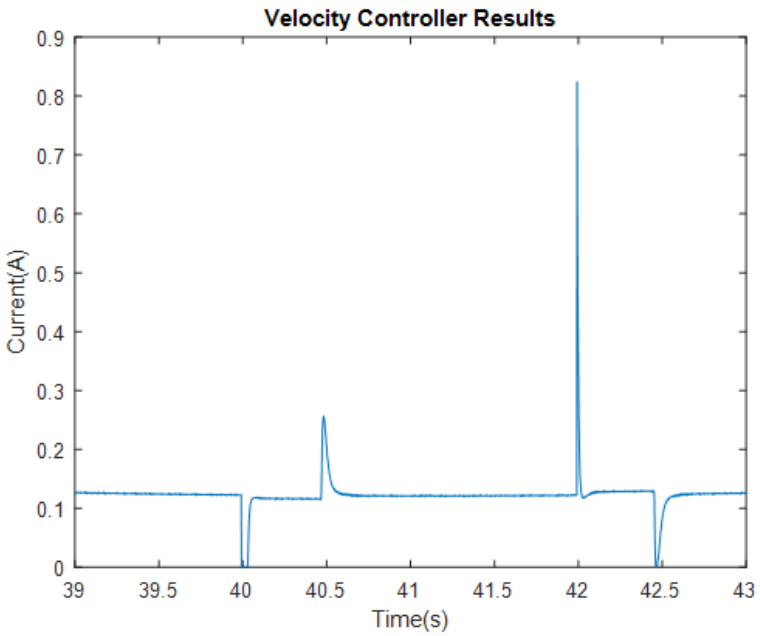

Figure 6.11: Velocity Controller Result for Dynamic Velocity Limit - Zoomed View

6.4.3 Changing Velocity and Current Limit Dynamically with Aerodynamic Torque

This solution approach is formed to have symmetric control capacity in both directions and at the same time to have no overshot through to flight. It is the combination of the first and the second solutions.

Input and output positions for this case are given in Figure 6.12. It can be seen from this figure that we have control ability through to flight without having any overshoot. The output of the velocity controller is given in Figure 6.13. A zoomed view of this figure is given in Figure 6.14 which shows the same part with Figure 6.11. It is clear that the asymmetric shape of the current demand is eliminated.

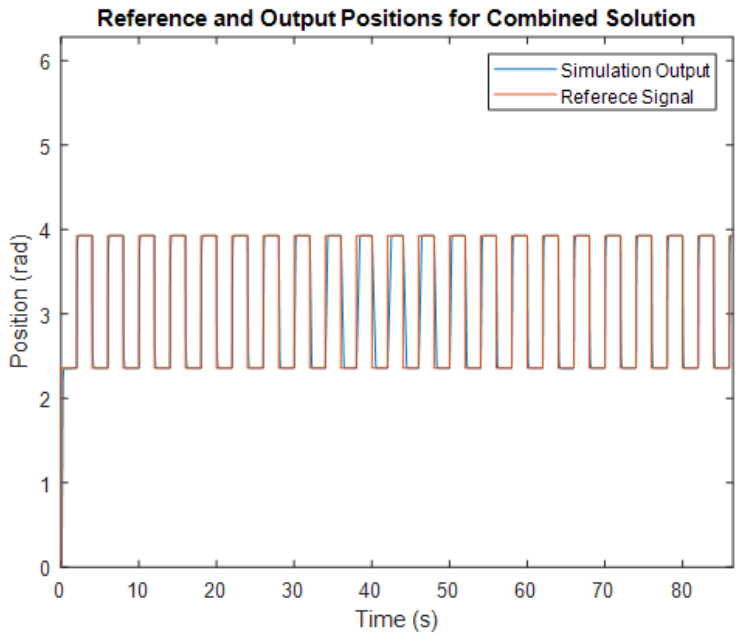

Figure 6.12: Input and Output Positions for Combined Solution

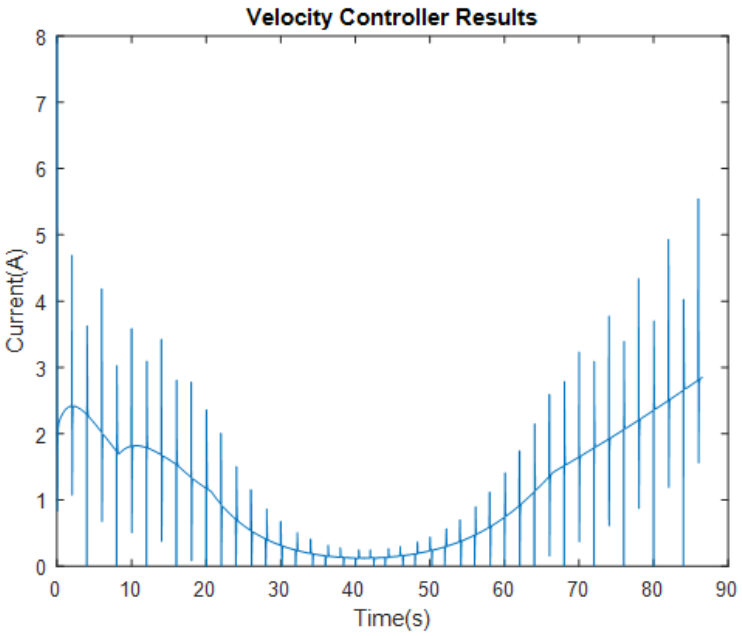

Figure 6.13: Velocity Controller Result for Combined Solution

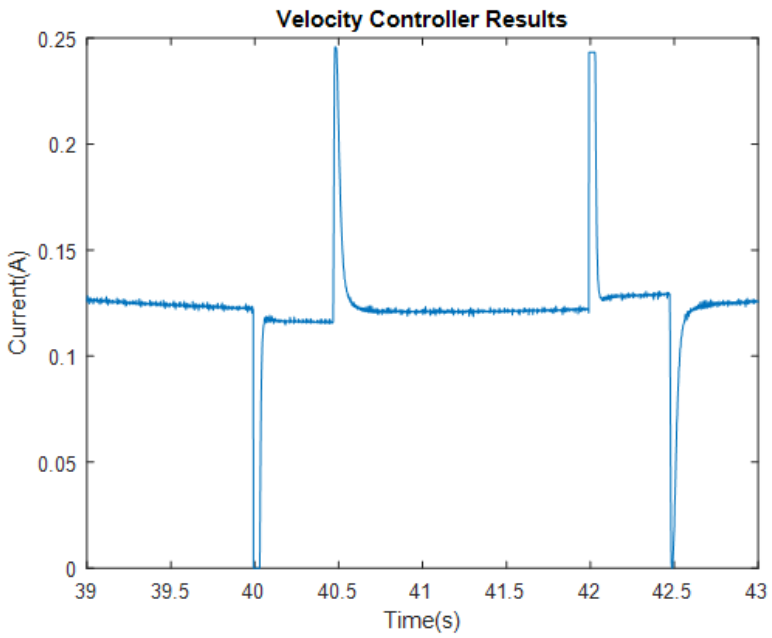

Figure 6.14: Velocity Controller Result for Combined Solution - Zoomed View

CHAPTER 7

TEST RESULTS FOR MODIFIED CONTROLLERS

All the three solutions are tested in real-life and the results are presented in the related sections. The transfer functions of the disturbance observer and filter are converted to discrete-time to be applicable in real-life. At this operation Matlab "c2d" function is used with "First-Order Hold" method and the time step is 1/1000s. Discretized transfer functions of the observer and filter are given in Equation 7.1 and 7.2.

$$G_{observer}(z) = \frac{0.003397z - 0.003394}{z - 0.998} \tag{7.1}$$

$$Q(z) = \frac{0.0009993z + 0.0009987}{z - 0.998} \tag{7.2}$$

These transfer functions are implemented to FPGA target and the results are presented in the next three sections. Also, the test results for the unmodified controller are given in this chapter.

7.1 The Results for Unmodified Controller

The input and output positions for test results and simulation results are presented in Figure 7.1. Zoomed views of this figure are given in Figure 7.2 and Figure 7.3. In the test case, the control ability is lost at a larger part of the flight in comparison to the simulation. Possible reasons for this situation are the dynamics of the programmable DC electronic load, continuous & discrete-time differences, and non-linear friction in the mechanical test system. Also, in the FPGA code, it is needed to use fixed-point numbers to implement the transfer functions. And also analog inputs and outputs

require fixed-point numbers. The losses at the conversion between floating point and fixed point can be a part of these differences. Also, in the test results, there are large overshoots that do not exist in the simulation. The reason behind this is the ability of the alternator to generate the required current with respect to relative velocity. The maximum current can be taken from the alternator, and the output of the velocity controller are given in Figure 7.4. This figure shows that the overshoot points match with the time that the velocity controller demands the maximum current that can be taken from the alternator. In real-life, this phenomenon causes an accumulation of error at the controller of the programmable DC load and it requires time to begin loading the alternator properly. Therefore, it causes overshoots in the system.

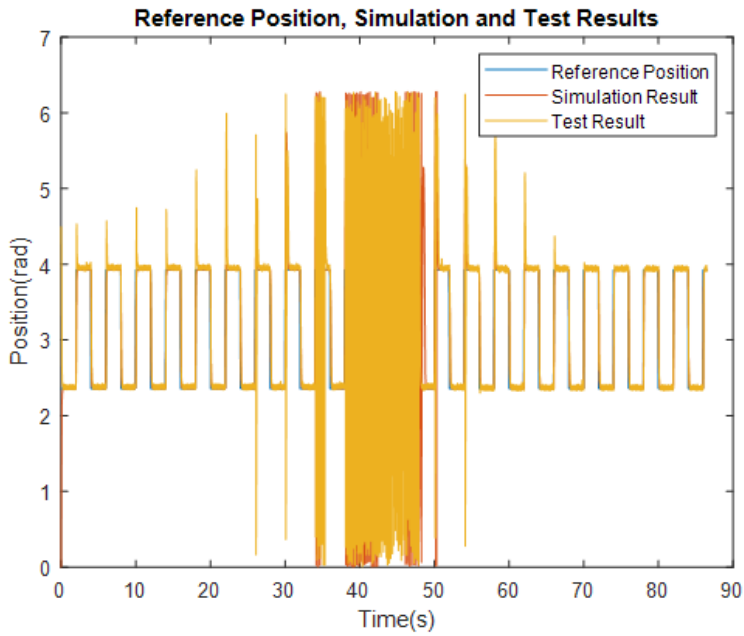

Figure 7.1: Input Position, Simulation, and Test Results for Unmodified Controller

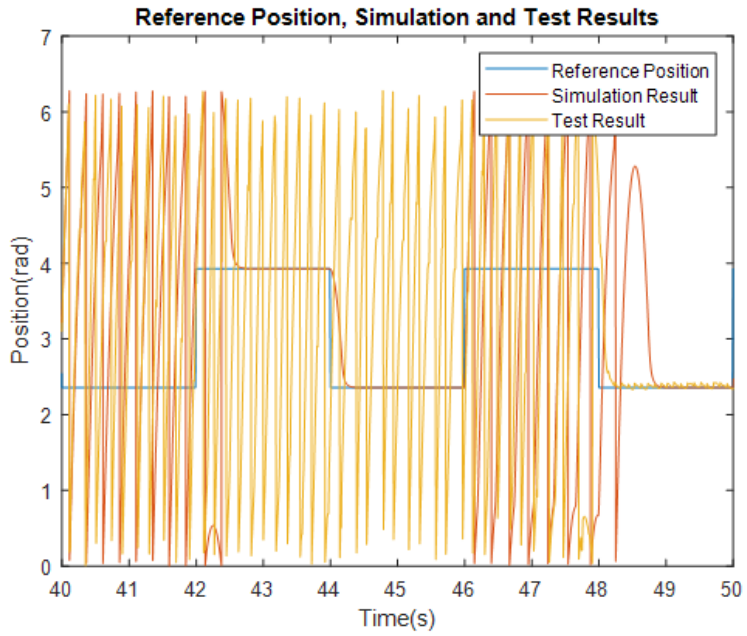

Figure 7.2: Input Position, Simulation, and Test Results for Unmodified Controller-Zoomed View

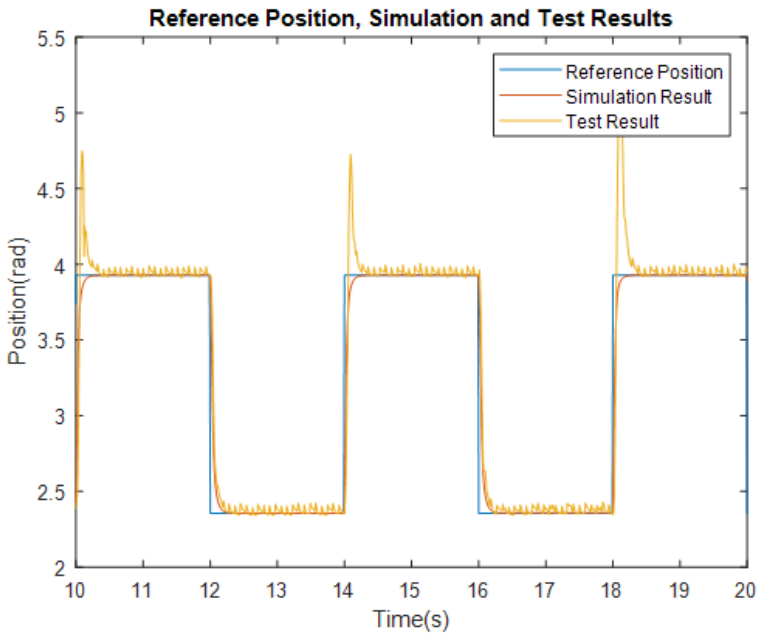

Figure 7.3: Input Position, Simulation, and Test Results for Unmodified Controller-Zoomed View

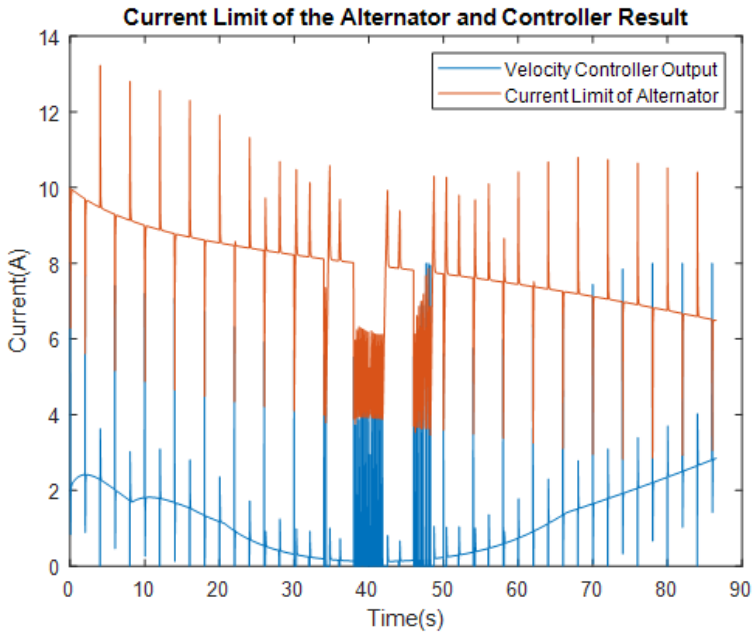

Figure 7.4: Alternator Saturation Points and Velocity Controller Results

7.2 Test Results for Changing Current Limit

This case is applied at the test set-up and the results for input and output positions are presented in Figure 7.5. Since we are not at the limit of the alternator, the test results are consistent with the simulation results. Also in this part, the test results and simulation results for the disturbance observer are compared and it is given in Figure 7.6. Since the results of the disturbance observer are nearly the same for all test conditions, it is not presented in the other sections. The result of the disturbance observer is consistent with simulation results at low aerodynamic torques. There is a difference between simulation and test results for high aerodynamic torque values.

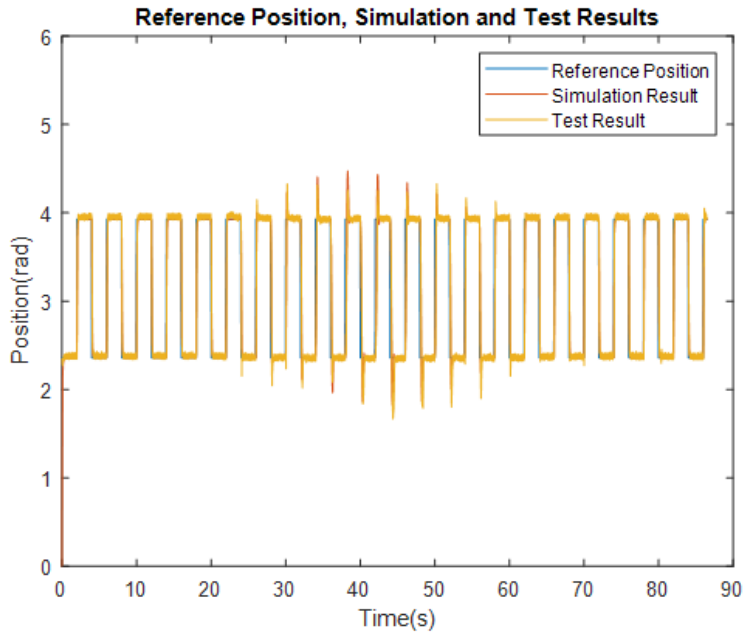

Figure 7.5: Input Position, Simulation, and Test Results for Changing Current Limit

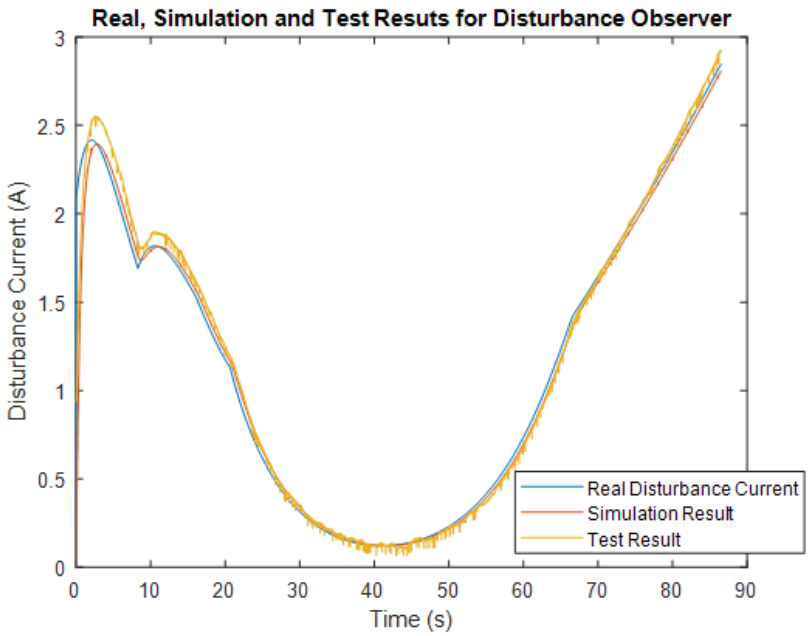

Figure 7.6: Comparison of the Disturbance Observer Results

7.3 Test Results for Changing Velocity Limit

The comparison of the test results and simulation results for changing the velocity limit is given in Figure 7.7. In this case, the same problem mentioned in section 7.1 is also happened. There are overshoots in the test results due to the load limit of the alternator with respect to the relative velocity between its rotor and stator. When the guidance kit rotates in the same direction with the body, the results of the velocity controller exceed the limit of the alternator and it causes large overshoots. To eliminate this, the output of the controller can also be saturated to be inside of the alternator load limit and it can be found by using present relative velocity which is an available data.

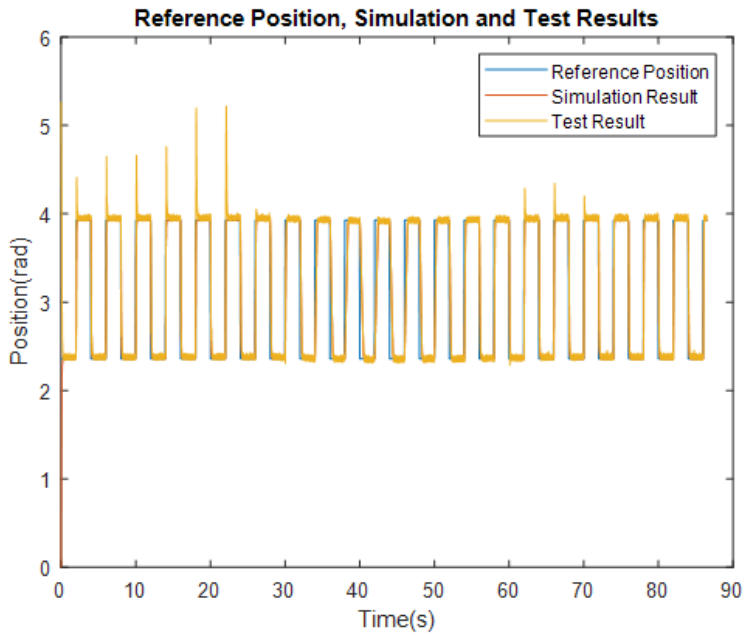

Figure 7.7: Input Position, Simulation, and Test Results for Changing Velocity Limit

7.4 Test Results for Combined Solution

The combined solution is also applied in real-life and the results are presented in Figure 7.8 for input and output positions. It is the best solution because we have no overshoot and we have symmetric responses in both directions. Also, since we are limiting the current with respect to aerodynamic torque, the limit of the alternator is

not reached.

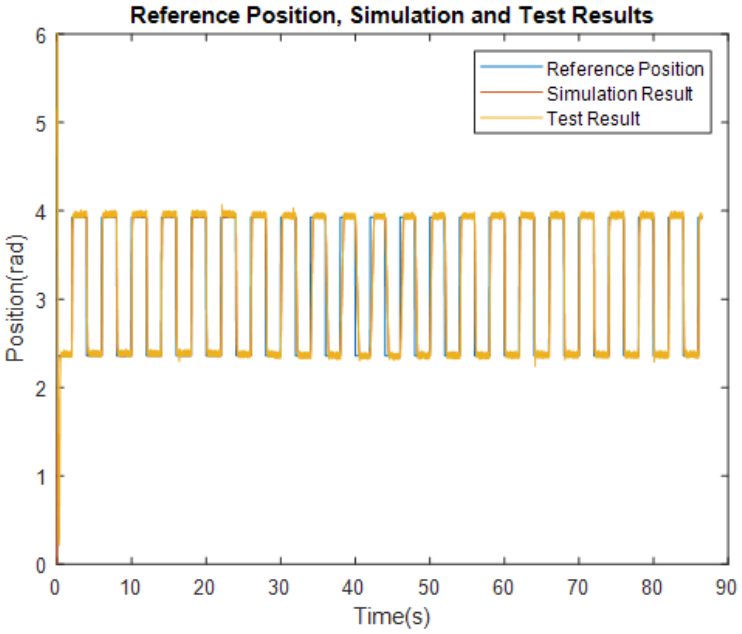

Figure 7.8: Input Position, Simulation, and Test Results for Combined Solution

The best solution is the combined solution due to symmetric response characteristics in both directions. Also in this solution, the transient response is consistent with design requirements which means there is no overshoot. The first solution is not applicable at the guidance of artillery projectiles in real-life because of the large overshoot which is an unwanted property for this application. The second solution can be applied to the real artillery projectile since the angular velocity of the projectile body always dominate the angular velocity of the guidance kit. The overshoot problem arises at the test setup since the velocity of the projectile body is scaled down. This makes the ratio of guidance kit angular velocity to the projectile body angular velocity larger.

CHAPTER 8

CONCLUSION AND FUTURE WORK

8.1 Conclusion

In this thesis subject, the feasibility of a guidance method for spin-stabilized munitions is examined.

In Chapter 1, the problem definition and motivation behind this study are explained. Also, the literature survey related to the solution of the guidance problem of spin-stabilized munitions and the flight dynamics of these munitions is presented. In addition, the outline of the thesis and contribution to the literature are explained in the first chapter.

In Chapter 2, the test set-up which is contracted to test the feasibility of the actuation system is explained. Specifications of the components that are used in the set-up are given in this chapter. The test software is also explained in Chapter 2.

In chapter 3, the mathematical model of the test set-up is established and different modeling techniques are compared. Also, test result related to the mathematical model is given in this chapter.

In chapter 4, controller design is explained. A cascade control structure is used to control the position of the guidance kit. Test results of the designed controller are given in this chapter.

In chapter 5, 6-DOF and 7-DOF dynamics of a spin-stabilized artillery projectile are modeled. Established models are simulated with Matlab / Simulink and results are given. The aerodynamic torque on the guidance kit and body angular velocity are

found in this section.

In chapter 6, the aerodynamic torque and body angular velocity, which are found in Chapter 5, are applied to the controller in the simulation environment. It is found that the system has large overshoots when the aerodynamic torque is low. At the apogee point, it is possible to lose the control ability of the system. 3 possible solutions are applied in the simulation environment and the results are compared in this section. The first solution is changing the current limit dynamically with respect to disturbance current. This solution solves the instability problem but it can not solve the overshoot problem. The second solution is changing the velocity limit dynamically with respect to the disturbance current. This solution solves instability and overshoot problems but the system responds asymmetrically in positive and negative directions. The third solution is the combination of the first and second solutions. This approach solves overshoot and instability problems. In the third solution, the system also has symmetric responses.

In chapter 7, the proposed solutions in Chapter 6 are applied to the test system. The results are compared with simulation results. As it is expected, the best solution is to change the saturation points of the velocity and current controller with respect to disturbance current. For this case, there is no overshoot through to flight and the system has symmetric behavior in both directions.

8.2 Future Work

By referencing the work done in this thesis, it is possible to state that the studied actuation method can be applied to spin-stabilized munitions.

In the scope of this thesis, the flight dynamics of the projectile is modeled at 6-DOF and 7-DOF. But Earth curvature, change in gravity with respect to altitude, and change in aerodynamic coefficients with incidence and sideslip angles are neglected. And guidance strategy is not worked in this thesis. The simulations can be extended to include these assumptions, and the guidance algorithm can be implemented in the future.

Aerodynamic torque found by simulations is applied directly to the test system. To be inside the limit of the test system, body velocity is scaled down. In the future, it is possible to design a test system and an alternator to simulate flight conditions directly.

In Chapter 7, the aerodynamic torque and body velocity are applied to the test system but the change in flight conditions due to guidance kit position is not considered. In the future, it is possible to make hardware-in-the-loop (HIL) simulations to include the impact of the guidance kit position on the flight parameters. And the guidance algorithm can also be included in HIL simulations to test the guidance algorithm with real actuator performance.

REFERENCES

[1] Y. Wang, X.-m. Wang, and J.-y. Yu, "Influence of control strategy on stability of dual-spin projectiles with fixed canards," *Defence technology*, vol. 14, no. 6, pp. 709–719, 2018.

[2] J. Spagni, S. Theodoulis, and P. Wernert, "Flight control for a class of 155 mm spin-stabilized projectile with reciprocating canards," in *AIAA Guidance, Navigation, and Control Conference*, p. 4685, 2012.

[3] A. Barton, "155-mm m795 aerofuze test at the kofa range, yuma proving ground, arizona, 19 may 2015," tech. rep., ARDEC, METC, RDAR-MEF-I Picatinny Arsenal United States, 2017.

[4] J. W. Robinson and F. Berefelt, *On Guidance and Control for Guided Artillery Projectiles, Part 1: General Considerations*. Defence & Security, Systems and Technology, Swedish Defence Research Agency . . . , 2011.

[5] J. A. Clancy, T. D. Bybee, and W. A. Friedrich, "Fixed canard 2-d guidance of artillery projectiles," Jan. 3 2006. US Patent 6,981,672.

[6] Y. Zhang, P. Li, L. Xiao, and F. Tian, "Research on control scheme of dual-spin projectile with fixed canards," in *2016 IEEE International Conference on Mechatronics and Automation*, pp. 144–148, IEEE, 2016.

[7] T. Yin, F. Jia, and J. Yu, "Research on roll control system for fixed canard rudder of the dual-spin trajectory correction projectile," *Wireless Personal Communications*, vol. 103, no. 1, pp. 83–98, 2018.

[8] M. Costello, "Modeling and simulation of a differential roll projectile," in *AIAA Modeling and Simulation Technologies Conference and Exhibit*, p. 4543, 1998.

[9] P. Wernert, S. Theodoulis, and Y. Morel, "Flight dynamics properties of 155 mm spin-stabilized projectiles analyzed in different body frames," in *AIAA atmospheric flight mechanics conference*, p. 7640, 2010.

[10] X. Zhang, Y. Xiaoxian, and Q. Zheng, "Impact point prediction guidance based on iterative process for dual-spin projectile with fixed canards," *Chinese Journal of Aeronautics*, vol. 32, no. 8, pp. 1967–1981, 2019.

[11] K. Ogata, *Modern Control Engineering*. Instrumentation and controls series, Prentice Hall, 2010.

[12] T. H. K. J. Astrom, *Advanced PID Control*. ISA Instrumentation, Systems and Automation Society, 2006.

[13] T. H. Karl J. Astrom, *PID Controllers*. International Society for Measurement and Con, 2 sub ed., 1995.

[14] A. Visioli, *Practical PID Control*. Advances in Industrial Control, Springer, 2006 ed., 2006.

[15] D. W. Smith, J. Crawford, and P. Moore, *Marine auxiliary machinery*. Elsevier, 2016.

[16] D. M. Soares, H. A. M. Calil, and R. M. Stephan, "Cascade control vs full-state feedback," in *2019 IEEE 15th Brazilian Power Electronics Conference and 5th IEEE Southern Power Electronics Conference (COBEP/SPEC)*, pp. 1–6, 2019.

[17] U. Karapinar, Z. Esen, M. Şahin, and F. Kanburoğlu, "Cascaded controller algorithm design for a brushless dc motor with matlab/simulink and mcu implementation," in *2013 21st Signal Processing and Communications Applications Conference (SIU)*, pp. 1–8, 2013.

[18] P. Wernert and S. Theodoulis, "Modelling and stability analysis for a class of 155 mm spin-stabilized projectiles with course correction fuse (ccf)," in *AIAA atmospheric flight mechanics conference*, p. 6269, 2013.

[19] P. Wernert and S. Theodoulis, "Modelling and stability analysis for a class of 155 mm spin-stabilized projectiles with course correction fuse (ccf)," in *AIAA atmospheric flight mechanics conference*, p. 6269, 2011.

[20] N. Sinha and N. Ananthkrishnan, *Advanced Flight Dynamics with Elements of Flight Control*. CRC Press, 2017.

[21] S. Li, J. Yang, W.-H. Chen, and X. Chen, *Disturbance observer-based control: methods and applications*. CRC press, 2014.

[22] J. Guan and W. Yi, "Modeling of dual-spinning projectile with canard and trajectory filtering," *International Journal of Aerospace Engineering*, vol. 2018, 2018.

[23] M. Khalil, H. Abdalla, *et al.*, "Dispersion analysis for spinning artillery projectile," in *International Conference on Aerospace Sciences and Aviation Technology*, vol. 13, pp. 1–12, The Military Technical College, 2009.

Appendix A

To be consistent with flight dynamics notation, angular velocity on X-axis is presented with p in all the equations.

Primary variables (Across-variables of tree branches and through variables of the links) and secondary variables (Through variables of the branches and across variables of the links) are listed below:

- Primary variables: $p_{body}(t)$, p_{gk}, V_{T_1}, V_{R_a}, V_{C_f}, $I_{load}(t)$, I_{L_a}, T_b, T_{T2}, $T_{aero}(t)$, T_{body}
- Secondary variables: $T_{body}(t)$, $T_{J_{gk}}$, I_{T1}, I_{R_a}, I_{C_F}, $V_{Load}(t)$, V_{L_a}, p_b, p_{T2}, $p_{T_{aero}}$, p_{body}

So the system states become (Across variables of A-Type elements on the normal tree, and through variables of T-type elements on the link) p_{gk}, V_{C_f} and I_{L_a}.

The elemental equations which relate across and through variables of the system are listed below:

$$\frac{dp_{gk}}{dt} = \frac{1}{J_{gk}} T_{J_{gk}} \tag{A.1}$$

$$V_{T1} = -K_v p_{T2} \tag{A.2}$$

$$V_{R_a} = I_{R_a} R_a \tag{A.3}$$

$$I_{C_f} = C_f \frac{dV_{C_f}}{dt} \tag{A.4}$$

$$\frac{dI_{L_a}}{dt} = \frac{1}{L_a} V_{L_a} \tag{A.5}$$

$$T_{T2} = K_t I_{T1} \tag{A.6}$$

$$T_b = b p_b \tag{A.7}$$

$$\frac{dp_{body}}{dt} = \frac{1}{J_{body}} T_{body} \tag{A.8}$$

Continuity equations of the system are listed below:

$$I_{R_a} = I_{L_a} \tag{A.9}$$

$$I_{R_a} - I_{C_f} - I_{load}(t) = 0 \tag{A.10}$$

$$I_{T1} + I_{L_a} = 0 \tag{A.11}$$

$$-T_{J_{gk}} + T_{aero}(t) - T_b - T_{T2} = 0 \tag{A.12}$$

Compatibility equations of the system are listed below:

$$V_{R_a} + V_{C_f} - V_{T1} + V_{L_a} = 0 \tag{A.13}$$

$$-p_{gk} + p_{T2} + p_{body}(t) = 0 \tag{A.14}$$

$$p_{body}(t) - p_{body} = 0 \tag{A.15}$$

$$p_b + p_{body}(t) - p_{gk} = 0 \tag{A.16}$$

By using the 16 equations listed above, the derivative of system states can be expressed in terms of input and states of the system. These equations are given below.

$$\frac{dp_{gk}}{dt} = \frac{b}{J_{gk}} p_{body}(t) - \frac{b}{J_{gk}} p_{gk} + \frac{K_t I_{L_a}}{J_{gk}} + \frac{T_{aero}(t)}{J_{GK}} \tag{A.17}$$

$$\frac{dV_{C_f}}{dt} = \frac{I_{L_a}}{C_f} - \frac{I_{load}(t)}{C_f} \tag{A.18}$$

$$\frac{dI_{L_a}}{dt} = \frac{-K_v p_{gk}}{L_a} + \frac{K_v p_{body}(t)}{L_a} - \frac{V_{C_f}}{L_a} - \frac{R_a I_{L_a}}{L_a} \tag{A.19}$$

Appendix B

To be consistent with flight dynamics notation, angular velocity on X-axis is presented with p in all the equations.

The circuit at the electrical part is given in Figure B.1.

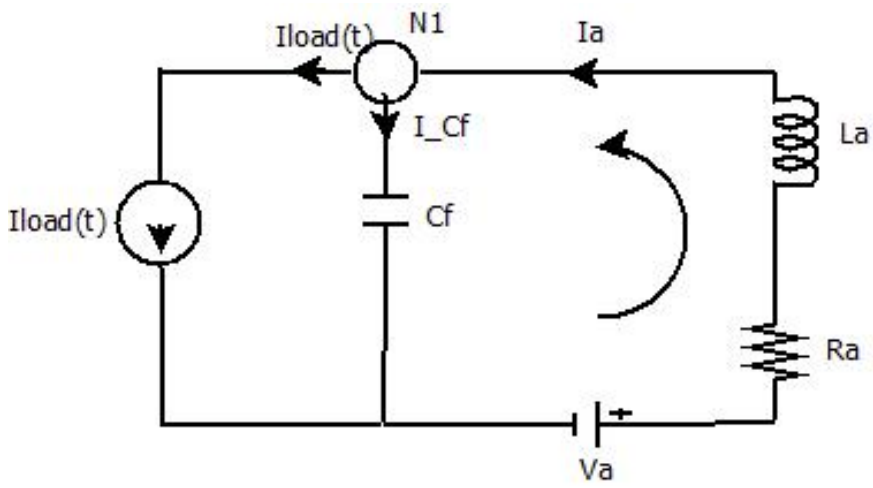

Figure B.1: Circuit of the Electrical Part

If we apply Kirchhoff's current law at N1 and take the Laplace transform:

$$I_{load} = I_a - I_{C_f} \tag{B.1}$$

If we apply Kirchhoff's voltage law and take the Laplace transform:

$$\begin{aligned} -Va + RI_a + L_a s I_a + \frac{1}{Cs} I_{C_f} &= 0 \\ -K_v(P_{body} - P_{gk}) + RI_a + L_a s I_a + \frac{1}{Cs} I_{C_f} &= 0 \end{aligned} \tag{B.2}$$

If we extract I_{C_f} from Equation B.1 and use it in Equation B.2:

$$-K_v(P_{body} - P_{gk}) + R_a I_a + L_a s I_a + \frac{1}{C_f s}(I_a - I_{load}) = 0 \tag{B.3}$$

B.1 Derivation of the Transfer Function Between I_{load} and P_{gk}

The free body diagram of J_{gk} for I_{load} is given in Figure B.2.

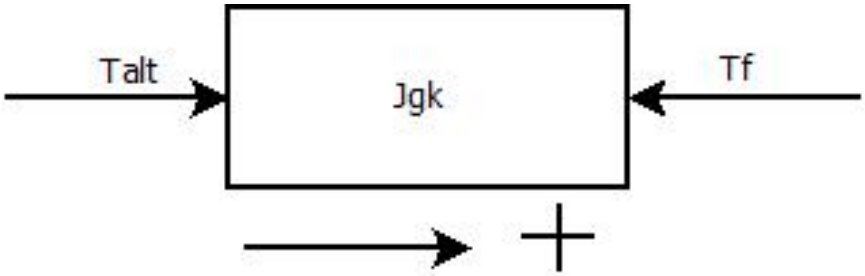

Figure B.2: Free Body Diagram of J_{gk} for I_{load}

Equation of the motion of the system is found as:

$$\begin{aligned} T_{alt} - T_f &= J_{gk}\frac{dp_{gk}}{dt} \\ T_{alt} &= K_t I_a \\ T_f &= bp_{gk} \end{aligned} \tag{B.4}$$

If we take Laplace transform of Equation B.4 and extract I_a in terms of P_{gk}:

$$I_a = \frac{P_{gk}(b + J_{gk}s)}{K_t} \tag{B.5}$$

If we take the input other than I_{load} as zero and make some algebraic manipulations in Equation B.3 we can find the following equation:

$$K_v P_{gk} + I_a(\frac{L_a C_f s^2 + R_a C_f s + 1}{C_f s}) = \frac{I_{load}}{C_f s} \tag{B.6}$$

If we use Equation B.5 and write I_a in terms of P_{gk} in Equation B.6 we can find the following transfer function:

$$
\begin{aligned}
G_{I_{load}P_{gk}} &= \frac{\beta_0}{\sigma_3 s^3 + \sigma_2 s^2 + \sigma_1 s + \sigma_0} \\
\beta_0 &= \frac{K_t}{L_a C_f J_{gk}} \\
\sigma_0 &= \frac{b}{L_a C_f J_{gk}} \\
\sigma_1 &= \frac{K_v K_t C_f + b R_a C_f + J_{gk}}{L_a C_f J_{gk}} \\
\sigma_2 &= \frac{b L_a C_f + R_a C_f Jgk}{L_a C_f J_{gk}} \\
\sigma_3 &= 1
\end{aligned}
\tag{B.7}
$$

We need to check the units of the parts added at σ_1 and σ_2.

$$
\begin{aligned}
K_v K_t C_f &= (Vs)(\frac{Nm}{A})(F) = (\frac{kgm^2}{As^3}s)(\frac{kgm}{s^2}m\frac{1}{A})(\frac{s^4A^2}{m^2kg}) \\
&= kgm^2 \\
bR_aC_f &= (\frac{kgm}{s^2}ms)(\frac{kgm^2}{s^3A^2})(\frac{s^4A^2}{m^2kg}) \\
&= kgm^2 \\
J_{gk} &= kgm^2
\end{aligned}
\tag{B.8}
$$

$$
\begin{aligned}
bL_aC_f &= (\frac{kgm}{s^2}ms)(\frac{kgm^2}{s^2A^2})(\frac{s^4A^2}{m^2kg}) \\
&= kgm^2s \\
R_aC_fJ_{gk} &= (\frac{kgm^2}{s^3A^2})(\frac{s^4A^2}{m^2kg})(kgm^2) \\
&= kgm^2s
\end{aligned}
\tag{B.9}
$$

The units of the added terms are consistent with each other. At the other transfer functions, the additive components of the denominator will not be checked since they are the same for the same systems.

B.2 Derivation of the Transfer Function Between $T_{aero}(t)$ and P_{gk}

The free body diagram of J_{gk} for T_{aero} is given in Figure B.3.

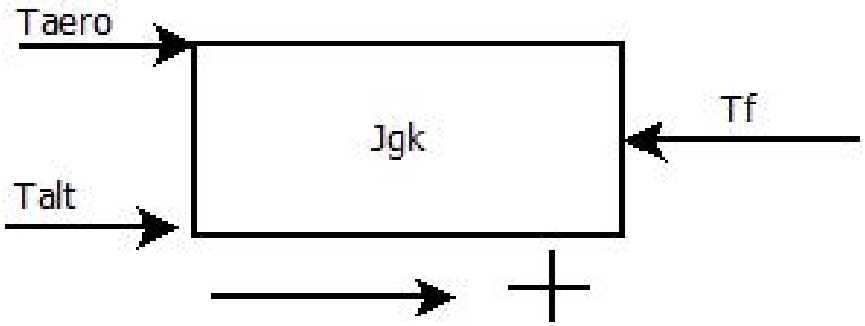

Figure B.3: Free Body Diagram of J_{gk} for T_{aero}

Since there will be a voltage change at the alternator due to changing p_{gk} we need to include this torque in the free body diagram. Equation of motion of is given in Equation B.10 in Laplace domain.

$$T_{aero} + K_t I_a = P_{gk}(b + J_{gk}s) \tag{B.10}$$

If we take P_{body} and I_{load} in Equation B.3 to zero and find I_a in therms of P_{gk} and system variables, this gives Equation B.11.

$$I_a = \frac{-K_v P_{gk} C_f s}{L_a C_f s^2 + R_a C_f s + 1} \tag{B.11}$$

If we write I_a as it is found in Equation B.11 in Equation B.10 it gives Equation B.12.

$$T_{aero} = P_{gk}(b + J_{gk}s + \frac{K_t K_v C_f s}{L_a C_f s^2 + R_a C_f s + 1}) \tag{B.12}$$

And the transfer function becomes:

$$
\begin{aligned}
G_{T_{aero}P_{gk}} &= \frac{\beta_2 s^2 + \beta_1 s + \beta_0}{\sigma_3 s^3 + \sigma_2 s^2 + \sigma_1 s + \sigma_0} \\
\beta_0 &= \frac{1}{J_{gk} L_a C_f} \\
\beta_1 &= \frac{R_a}{J_{gk} L_a} \\
\beta_2 &= \frac{1}{J_{gk}} \\
\sigma_0 &= \frac{b}{J_{gk} L_a C_f} \\
\sigma_1 &= \frac{b R_a C_f + K_t K_v C_f + J_{gk}}{J_{gk} L_a C_f} \\
\sigma_2 &= \frac{J_{gk} R_a + L_a b}{J_{gk} L_a} \\
\sigma_3 &= 1
\end{aligned}
\tag{B.13}
$$

There is no need to check units at this transfer function.

B.3 Derivation of the Transfer Function Between P_{body} and P_{gk}

The free body diagram of J_{gk} for p_{body} is given in Figure B.4.

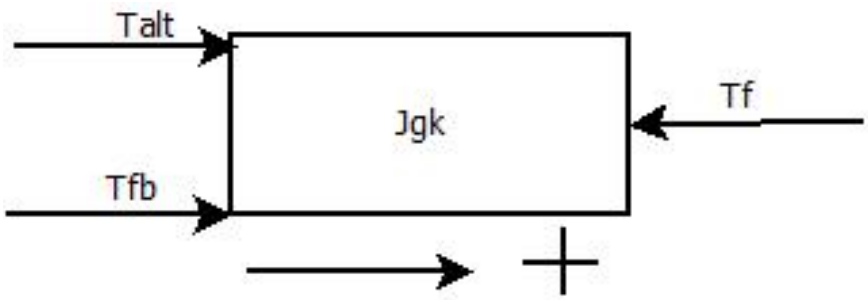

Figure B.4: Free Body Diagram of J_{gk} for p_{body}

In Figure B.4, T_{alt} represents the torque generated by the alternator due to the change in voltage with respect to p_{body} and p_{gk}, T_f represents friction due to velocity of p_{gk} and T_{fb} represents the friction due to velocity of the p_{body}. The expressions related to these torques are given in Equation B.14.

$$
\begin{aligned}
T_{alt} &= K_t I_a \\
T_{fb} &= bp_{body} \\
T_f &= bp_{gk}
\end{aligned}
\tag{B.14}
$$

The equation of motion is given in Equation B.14 in Laplace domain.

$$
bP_{body} + K_t I_a = P_{gk}(b + J_{gk}s) \tag{B.15}
$$

If we take I_{load} as zero and find I_a in terms of P_{gk} and P_{body} in Equation B.3 it gives Equation B.16.

$$
I_a = \frac{C_f s K_v (P_{body} - P_{gk})}{L_a C_f s^2 + R_a C_f s + 1} \tag{B.16}
$$

If we put the result of Equation B.16 into Equation B.15 it gives Equation B.17.

$$
P_{body}(b + \frac{K_t K_v C_f s}{L_a C_f s^2 + R_a C_f s + 1}) = P_{gk}(b + s(J_{gk} + \frac{K_t K_v C_f}{L_a C_f s^2 + R_a C_f s + 1})) \tag{B.17}
$$

The transfer function becomes:

$$
\begin{aligned}
G_{P_{body}P_{gk}} &= \frac{\beta_2 s^2 + \beta_1 s + \beta_0}{\sigma_3 s^3 + \sigma_2 s^2 + \sigma_1 s + \sigma_0} \\
\beta_0 &= \frac{b}{L_a C_f J_{gk}} \\
\beta_1 &= \frac{bR_a + K_t K_v}{L_a J_{gk}} \\
\beta_2 &= \frac{b}{J_{gk}} \\
\sigma_0 &= \frac{b}{L_a C_f J_{gk}} \\
\sigma_1 &= \frac{J_{gk} + bR_a C_f + K_t K_v C_f}{L_a C_f J_{gk}} \\
\sigma_2 &= \frac{R_a J_{gk} + bL_a}{L_a J_{gk}} \\
\sigma_3 &= 1
\end{aligned}
\tag{B.18}
$$

We need to check the units of added terms in β_1.

$$
\begin{aligned}
bR_a &= (Nms)(Ohm) \\
&= ((\frac{kgm}{s^2})ms)(\frac{kgm^2}{s^3A^2}) \\
&= \frac{kg^2m^4}{s^4A^2} \\
K_tK_v &= (\frac{Nm}{A})(Vs) \\
&= (\frac{kgm}{s^2}m\frac{1}{A})(\frac{kgm^2}{As^3}s) \\
&= \frac{kg^2m^4}{A^2s^4}
\end{aligned}
\tag{B.19}
$$

The units are consistent with each other.

Appendix C

Contents

- Velocity Controller Design
- Position Controller Design

```
clc
clear all
close all


% System parameters
Cf = 5*(10^-5);                          % in Farad
La = 8.8*10^-3;                          % in Hennry
Ra = 6.2;                                % in ohm
J_holder = 1.678*10^-4;                  % in kg*m^2
J_alternator_body = 7.55*10^-4;          % in kg*m^2
J_coupling = 4.069*10^-5;                % in kg*m^2
J_magnets = 1.485*10^-4;                 % in kg*m^2
J_motor = 0.85*10^-4;                    % in kg*m^2
Jgk = J_holder + J_alternator_body +J_coupling...
+ J_magnets +J_motor ;
b = 0.2/(1500/60*2*pi)                   % in Nm/(rad/sec)
Kt = 0.72 ;                              % in Nm/A
Kv = 0.75 ;                                % V/(rad/sec)
```

```
% Form system and input matrices
A1_1 = -b/Jgk;
A1_2 = 0;
A1_3 = Kt/Jgk;

A2_1 = 0;
A2_2 = 0;
A2_3 = 1/Cf;

A3_1 = -Kv/La;
A3_2 = -1/La;
A3_3 = -Ra/La;

A = [A1_1, A1_2, A1_3;
     A2_1, A2_2, A2_3;
     A3_1, A3_2, A3_3];

B1_1 = b/Jgk;
B1_2 = 1/Jgk;
B1_3 = 0;
B2_1 = 0;
B2_2 = 0;
B2_3 = -1/Cf;
B3_1 = Kv/La;
B3_2 = 0;
B3_3 = 0;


B = [B1_1, B1_2, B1_3;
     B2_1, B2_2, B2_3;
     B3_1, B3_2, B3_3];

% Form system output matrices - OmegaGk
```

```
C =[1, 0, 0];
D =[0, 0, 0];



stateSpaceModel = ss(A, B, C, D)

G_sys = tf(stateSpaceModel)

% Transfer function between Iload(t) and Omega_Jgk
beta0= Kt/(La*Cf*Jgk) ;
sigma0 = b/(La*Cf*Jgk) ;
sigma1_1 = Kv*Kt*Cf/(La*Cf*Jgk) ;
sigma1_2 = b*Ra*Cf/(La*Cf*Jgk) ;
sigma1_3 = Jgk/(La*Cf*Jgk) ;
sigma1 = sigma1_1+sigma1_2+sigma1_3 ;
sigma2_1 = b*La*Cf/(La*Cf*Jgk) ;
sigma2_2 = Ra*Cf*Jgk/(La*Cf*Jgk) ;
sigma2 = sigma2_1+sigma2_2 ;
sigma3 = 1;
num1 = [beta0] ;
denum1 = [sigma3, sigma2, sigma1, sigma0] ;
G_Iload_pgk = tf(num1, denum1)


% Transfer function between Taero(t) and Omega_Jgk
beta0 = 1/(Jgk*La*Cf);
beta1 = Ra/(Jgk*La);
beta2 = 1/Jgk;
sigma0 = b/(Jgk*La*Cf);
sigma1 = (b*Ra*Cf+Kt*Kv*Cf+Jgk)/(Jgk*La*Cf);
sigma2 = (Jgk*Ra+La*b)/(Jgk*La);
```

```
sigma3 = 1;
num2= [beta2, beta1, beta0];
denum2 = [sigma3, sigma2, sigma1, sigma0];
G_Taero_pgk = tf(num2, denum2)

% Transfer function between Omega_body(t) and Omega_Jgk
beta0 = b/(Jgk*La*Cf);
beta1 = (b*Ra+Kt*Kv)/(Jgk*La);
beta2 = b/Jgk;
sigma0 = b/(Jgk*La*Cf);
sigma1 = (b*Ra*Cf+Kt*Kv*Cf+Jgk)/(Jgk*La*Cf);
sigma2 = (Jgk*Ra+La*b)/(Jgk*La);
sigma3 = 1;
num3= [beta2, beta1, beta0];
denum3 = [sigma3, sigma2, sigma1, sigma0];
G_OmegaBody_pgk = tf(num3, denum3)
```

Velocity Controller Design

```
s = tf('s');
pole_G_Iload_pgk = pole(G_Iload_pgk)
rlocus(G_Iload_pgk)
title('G_Iload_pgk')
xlim([-500 100])
ylim([-2000 2000])
% Velocity Controller Reuirements
syms zeta wn
ts_v = 0.05 % %5 settling time
Mp = 25     % Max overshoot, %
Eq1 = 25 == 100*(exp(-(zeta/(sqrt(1-zeta^2)))*pi))
zeta_v = double(solve(Eq1))
zeta_v = max(zeta_v)
wn_v = 3/(ts_v*zeta_v)
```

```
sgrid(zeta_v, wn_v)
figure

rlocus(G_Iload_pgk*((s+26.98)/s))
title('Compansated G_Iload_pgk ')
xlim([-500 100])
ylim([-2000 2000])
sgrid(zeta_v, wn_v)
figure
Gvc = 0.289860532841818*(s+26.98)/s
Gol_v = G_Iload_pgk*Gvc
Gcl_v = feedback(Gol_v,1)
pole_clv = pole(Gcl_v)
step(Gcl_v)
title('Closed Loop Velocity')
figure
bode(Gcl_v)
title('Bode-Closed Loop Velocity')
figure

% Check disturbance rejection
Ev_Taero = -G_Taero_pgk/(1+Gvc*G_Iload_pgk)
step(Ev_Taero)
title('Step Response for Step T_a_e_r_o Disturbance')
figure
%
%
Ev_OmegaGk = -G_OmegaBody_pgk/(1+Gvc*G_Iload_pgk)
step(Ev_OmegaGk )
title('Step Response for Step P_b_o_d_y Disturbance')
figure
```

Position Controller Design

```
Gol_p = Gcl_v*1/s
pole_olp = pole(Gol_p)
rlocus(Gol_p)
title('Open Loop Position')
%Position controller requirements
ts_p = 0.1 % %5 settling time
Mp = 5     % Max overshoot
Eq1 = Mp == 100*(exp(-(zeta/(sqrt(1-zeta^2)))*pi))
zeta_p = double(solve(Eq1))
zeta_p = max(zeta_p)
wn_p = 3/(ts_p*zeta_p)
sgrid(zeta_p, wn_p)
xlim([-350 50])
ylim([-1550, 1550])
figure
Gcl_p = feedback(Gol_p*29.7,1)
step(Gcl_p)
title('Closed Loop Position')
figure
pole_clp=pole(Gcl_p)
bode(Gcl_p)
title('Bode-Closed Loop Position');
```

Appendix D

Equation of motion in a non-inertial reference frame is given in Equation D.1.

$$\begin{aligned} \mathbf{F} &= m\left(\frac{d\mathbf{V}}{dt}\bigg|_{BFP} + \boldsymbol{\omega}_{BFP} \times \mathbf{V}\right) \\ \mathbf{M} &= \mathbf{I}\frac{d\boldsymbol{\omega}}{dt}\bigg|_{BFP} + \boldsymbol{\omega}_{BFP} \times \mathbf{I}\boldsymbol{\omega} \end{aligned} \tag{D.1}$$

The symbols used in Equation D.1 are explained in the equations below.

F: Total force vector acting on projectile body written in Body Fixed Plane Reference Frame.

$$\mathbf{F} = \begin{bmatrix} X \\ Y \\ Z \end{bmatrix} \tag{D.2}$$

M: Total moment vector acting on projectile body written at Body Fixed Plane Reference Frame.

$$\mathbf{M} = \begin{bmatrix} L \\ M \\ N \end{bmatrix} \tag{D.3}$$

V: Linear velocity vector of the projectile body written at Body Fixed Plane Reference Frame.

$$\mathbf{V} = \begin{bmatrix} u \\ v \\ w \end{bmatrix} \tag{D.4}$$

$\boldsymbol{\omega}_{BFP}$: Angular velocity vector of the Body Fixed Plane Reference Frame.

$$\boldsymbol{\omega}_{BFP} = \begin{bmatrix} p_{BFP} \\ q \\ r \end{bmatrix} \tag{D.5}$$

$\boldsymbol{\omega}$: Angular velocity vector of the projectile body written at Body Fixed Plane Reference Frame.

$$\boldsymbol{\omega}_{6DOF} = \begin{bmatrix} p \\ q \\ r \end{bmatrix} \tag{D.6}$$

I: Inertia matrix of the projectile body.

$$\mathbf{I} = \begin{bmatrix} I_x & 0 & 0 \\ 0 & I_y & 0 \\ 0 & 0 & I_Z \end{bmatrix} \tag{D.7}$$

Cross product of $\boldsymbol{\omega}_{BFP}$ can be written in matrix form and if we replace p_{BFP} in this matrix form with $-r\tan\theta$, which is found in Equation 5.5, the skew-symmetric matrix form of the cross product is given in Equation D.8.

$$\boldsymbol{\omega}_{BFP}\times = \begin{bmatrix} 0 & -r & q \\ r & 0 & r\tan\theta \\ -q & -r\tan\theta & 0 \end{bmatrix} \tag{D.8}$$

If we take the derivative of the linear velocity vector in Equation D.1 to the left side and replace the symbols with Equations D.2, D.4, D.5, and D.8; the equation of the motion of the linear velocity can be found as given in Equation D.9.

$$\begin{bmatrix} \dot{u} \\ \dot{v} \\ \dot{w} \end{bmatrix} = \begin{bmatrix} \frac{X}{m} \\ \frac{Y}{m} \\ \frac{Z}{m} \end{bmatrix} - \begin{bmatrix} 0 & -r & q \\ r & 0 & r\tan\theta \\ -q & -r\tan\theta & 0 \end{bmatrix} \begin{bmatrix} u \\ v \\ w \end{bmatrix} \tag{D.9}$$

If we take the derivative of the angular velocity vector in Equation D.1 to the left side and replace the symbols with Equations D.3, D.5, D.6, D.7, and D.8; the equation of the motion of the angular velocity can be found as given in Equation D.10.

$$\begin{bmatrix} \dot{p} \\ \dot{q} \\ \dot{r} \end{bmatrix} = \mathbf{I}^{-1} \left(\begin{bmatrix} L \\ M \\ N \end{bmatrix} - \begin{bmatrix} 0 & -r & q \\ r & 0 & r\tan\theta \\ -q & -r\tan\theta & 0 \end{bmatrix} \mathbf{I} \begin{bmatrix} p \\ q \\ r \end{bmatrix} \right) \tag{D.10}$$

The transformation of the body axis angular angular velocity vector to the rate of Euler angles is given in Equation D.11.

$$\begin{bmatrix} \dot{\phi} \\ \dot{\theta} \\ \dot{\psi} \end{bmatrix} = \begin{bmatrix} 1 & \sin\phi\tan\theta & \cos\phi\tan\theta \\ 0 & \cos\phi & -\sin\phi \\ 0 & \frac{\sin\phi}{\cos\theta} & \frac{\cos\phi}{\sin\theta} \end{bmatrix} \begin{bmatrix} p_F \\ q_F \\ r_F \end{bmatrix} \tag{D.11}$$

Since $\dot{\phi}$ and ϕ are equated to zero by equating p_F to $-r\tan\theta$, Equation D.11 reduces to Equation D.12. Note that, the rotation of the Body Fixed Plane Reference Frame is the same with the angular velocity of the projectile except p_F. Therefore, q_F and r_F is replaced with q and r.

$$\begin{bmatrix} \dot{\theta} \\ \dot{\psi} \end{bmatrix} = \begin{bmatrix} 1 & 0 \\ 0 & \frac{1}{\cos\theta} \end{bmatrix} \begin{bmatrix} q \\ r \end{bmatrix} \tag{D.12}$$

The transformation of linear velocities of the body to Earth Fixed Reference Frame is given in Equation D.13.

$$\begin{bmatrix} \dot{x_E} \\ \dot{y_E} \\ \dot{z_E} \end{bmatrix} = \mathbf{G} \begin{bmatrix} u \\ v \\ w \end{bmatrix} \tag{D.13}$$

where transformation matrix **G** is given in Equation D.14.

$$\mathbf{G} = \begin{bmatrix} \cos\theta\cos\psi & \sin\phi\sin\theta\cos\psi - \cos\phi\sin\psi & \cos\phi\sin\theta\cos\psi + \sin\phi\sin\psi \\ \cos\theta\sin\psi & \sin\phi\sin\theta\sin\psi + \cos\phi\cos\psi & \cos\phi\sin\theta\sin\psi - \sin\phi\cos\psi \\ -\sin\theta & \sin\phi\cos\theta & \cos\phi\cos\theta \end{bmatrix} \tag{D.14}$$

Since we equated ϕ to 0, Equation D.14 reduces to Equation D.15.

$$\mathbf{G} = \begin{bmatrix} \cos\theta\cos\psi & -\sin\psi & \sin\theta\cos\psi \\ \cos\theta\sin\psi & \cos\psi & \sin\theta\sin\psi \\ -\sin\theta & 0 & \cos\theta \end{bmatrix} \tag{D.15}$$

Appendix E

With the addition of 1-DOF to the system, the inertia matrix, moment vector, angular velocity vector, and the skew-symmetric matrix form of the cross product of $\boldsymbol{\omega}_{BFP}$ need to be modified. [22]

Since the system has an independent degree of freedom at the X-axis, the inertia matrix should be updated to include two different inertia which can rotate independently.

The modified inertia matrix is given in Equation E.1.

$$\begin{bmatrix} I_{x_{gk}} & 0 & 0 & 0 \\ 0 & I_{x_{body}} & 0 & 0 \\ 0 & 0 & I_y & 0 \\ 0 & 0 & 0 & I_z \end{bmatrix} \tag{E.1}$$

Torques at the guidance kit need to be added to the moment vector. We need to add a row to $\mathbf{M}_{7DOF}$ to take total aerodynamic torque in the guidance kit, $L_{gk-7DOF}$ which is given in Equation G.18, into account. The modified moment vector is given in Equation E.2.

$$\mathbf{M}_{7DOF} = \begin{bmatrix} L_{gk-7DOF} \\ L_{b-7DOF} \\ M_{7DOF} \\ N_{7DOF} \end{bmatrix} \tag{E.2}$$

The angular velocity vector of the projectile needs to be modified to include the angular velocity of the guidance kit, p_{gk}. The modified angular velocity vector is given

in Equation E.3.

$$\boldsymbol{\omega}_{7DOF} = \begin{bmatrix} p_{gk} \\ p_{body} \\ q \\ r \end{bmatrix} \tag{E.3}$$

The skew-symmetric matrix version of the cross product of $\boldsymbol{\omega}_{BFP}$ needs to be modified to be consistent with the dimensions of the other vectors. Also, the first row of the matrix needs to be doubled since p_{body} and p_{gk} should be multiplied by the same row. Since they are independent angular velocities at the same axis, the row they need to be multiplied by should be the same to take the derivative in the non-inertial frame correctly. The modified version is given in Figure E.4.

$$\boldsymbol{\omega}_{BFP}\times = \begin{bmatrix} 0 & 0 & -r & q \\ 0 & 0 & -r & q \\ 0 & r & 0 & r\tan\theta \\ 0 & -q & -r\tan\theta & 0 \end{bmatrix} \tag{E.4}$$

Appendix F

The numerical value of the transfer function between I_{load} and p_{gk} is given in Equation F.1. Also in this equation locations of the poles are presented.

$$\begin{aligned} G_{I_{load}P_{gk}} &= \frac{1.367e9}{s^3 + 705.6s^2 + 2.325e6s + 2.418e6} \\ p1 &= -1.04 \\ p2 &= -352.28 + 1483.20i \\ p3 &= -352.28 - 1483.20i \end{aligned} \tag{F.1}$$

Since the complex conjugate pole pair is 338.73 times far away from the imaginary axis, it is possible to neglect the dynamics coming from these poles. By using partial fraction expansion we can find residues related to poles. Residues and pole pairs are found by using Matlab "residue" function and they are listed in Equation F.2. Residues for complex conjugate poles are not in the traditional form since Matlab gives complex residues for complex conjugate pole pairs.

$$\begin{aligned} G_{I_{load}P_{gk}} &= \frac{1.367e9}{s^3 + 705.6s^2 + 2.325e6s + 2.418e6} \\ r1 &= 588.4 \\ r2 &= -294.2 + 69.7i \\ r3 &= -294.2 - 69.7i \end{aligned} \tag{F.2}$$

The reduced transfer function is given in Equation F.3. The comparison of the step responses for original and reduced transfer functions is given in Figure F.1. As it is expected, the results are nearly the same.

$$\hat{G} = \frac{588.4}{s + 1.04} \tag{F.3}$$

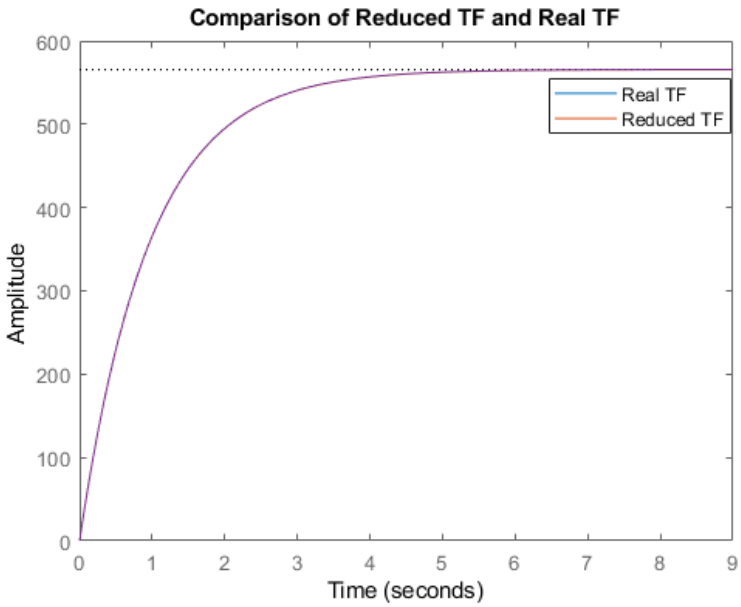

Figure F.1: Comparison of Real and Reduced Transfer Functions

The main parameter in the first-order low pass filter design is the time constant. A relatively large time constant, 0.5, is selected in order not to take the responses due to measurement noise. Since aerodynamic torque and friction torque does not have high-frequency component it is a proper choice for this control case. Step response and Bode plot of the designed filter are given in Figure F.3 and Figure F.2. The transfer function of the designed filter is given in Equation F.4.

$$Q = \frac{1}{0.5s + 1} \tag{F.4}$$

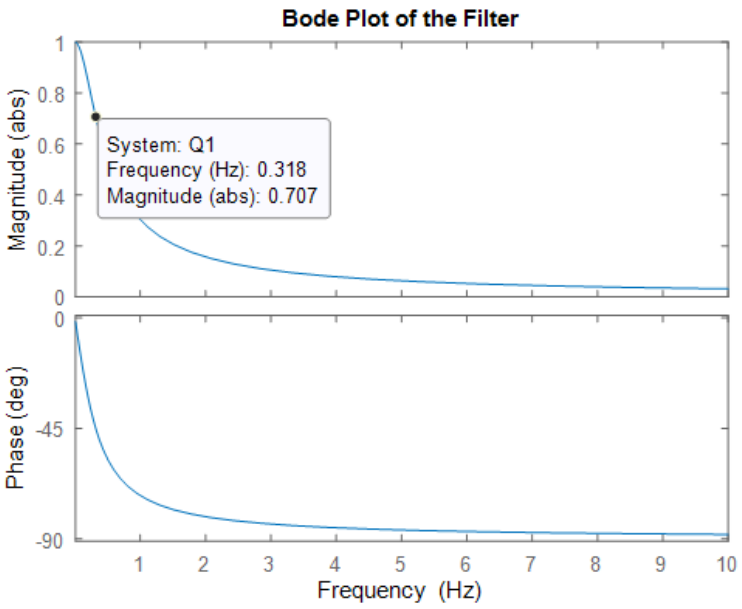

Figure F.2: Bode Plot of the Filter

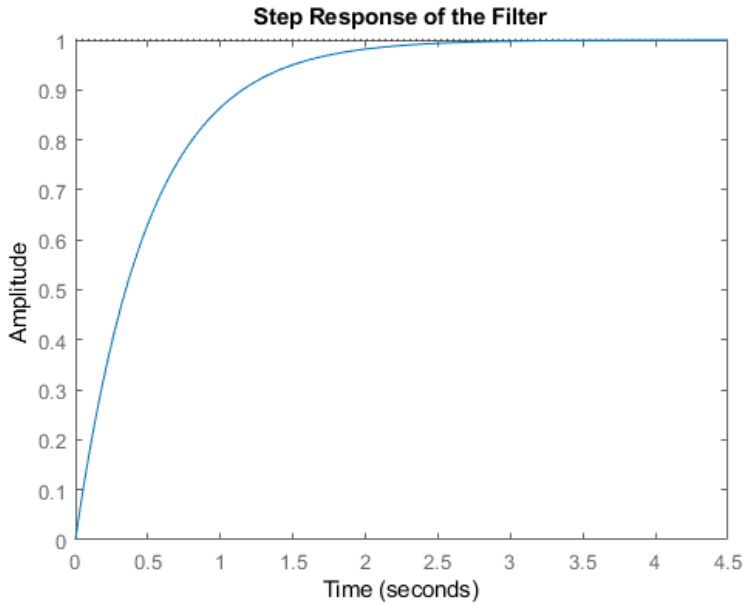

Figure F.3: Step Response of the Filter

Appendix G

G.1 Aerodynamic Forces And Moments

Aerodynamic forces and moments on a spin-stabilized projectile are explained in this section. Numerical values of the coefficients are taken from [23]. Aerodynamic forces and moments are calculated at the reference frame where incidence angle α and sideslip angle β are calculated. Definitions of the α and β are given in Equation G.1 where u, v, and w are linear velocity components of the center of mass.

$$\begin{aligned} \alpha &= \tan^{-1}(\frac{w}{u}) \\ \beta &= \tan^{-1}(\frac{v}{\sqrt{u^2+w^2}}) \end{aligned} \tag{G.1}$$

G.1.1 Aerodynamic Forces And Moments for 6-DOF Model

G.1.1.1 Lift Force

$$\mathbf{L} = \frac{1}{2}\rho S V^2 C_{L\alpha} \times \begin{bmatrix} \sin\beta^2 + \cos\beta^2 \sin\alpha^2 \\ -\sin\beta\cos\alpha\cos\beta \\ -\cos\beta^2 \sin\alpha\cos\alpha \end{bmatrix} \tag{G.2}$$

G.1.1.2 Drag Force

$$\mathbf{D} = -\frac{1}{2}\rho S V^2 C_D \times \begin{bmatrix} \cos\alpha\cos\beta \\ \sin\beta \\ \sin\alpha\cos\beta \end{bmatrix} \tag{G.3}$$

G.1.1.3 Magnus Force

$$\mathbf{K} = \frac{1}{2}\rho S V^2 C_{yp\alpha}\frac{pd}{V} \times \begin{bmatrix} 0 \\ -\sin\alpha\cos\beta \\ \sin\beta \end{bmatrix} \tag{G.4}$$

G.1.1.4 Pitching/Yawing Moment

$$\mathbf{M}_{PY} = \frac{1}{2}\rho s d V^2 C_{M\alpha} \times \begin{bmatrix} 0 \\ \sin\alpha\cos\beta \\ -\sin\beta \end{bmatrix} \tag{G.5}$$

G.1.1.5 Magnus Moment

$$\mathbf{M}_m = \frac{1}{2}\rho S d V^2 (-C_{np\alpha})\frac{pd}{V} \times \begin{bmatrix} 0 \\ -\sin\beta \\ -\sin\alpha\cos\beta \end{bmatrix} \tag{G.6}$$

G.1.1.6 Pitch / Yaw Damping Moment

$$\mathbf{M}_{pyd} = \frac{1}{2}\rho S d V^2 C_{mq}\frac{d}{V} \times \begin{bmatrix} 0 \\ q \\ r \end{bmatrix} \tag{G.7}$$

G.1.1.7 Roll Damping Moment

$$\mathbf{M}_{rd} = \frac{1}{2}\rho S d V^2 C_{lp} \frac{pd}{V} \times \begin{bmatrix} 1 \\ 0 \\ 0 \end{bmatrix} \tag{G.8}$$

G.1.1.8 Gravitational Force

$$\mathbf{F}_g = mg \times \begin{bmatrix} -\sin\theta \\ \sin\phi\cos\theta \\ \cos\phi\cos\theta \end{bmatrix} \tag{G.9}$$

Total aerodynamic forces on the projectile are given in Equation G.10.

$$\mathbf{F} = \begin{bmatrix} X \\ Y \\ Z \end{bmatrix} = \mathbf{L} + \mathbf{D} + \mathbf{K} + \mathbf{F}_g \tag{G.10}$$

Total aerodynamic moments on the projectile body are given in Equation G.11.

$$\mathbf{M} = \begin{bmatrix} L \\ M \\ N \end{bmatrix} = \mathbf{M}_{PY} + \mathbf{M}_m + \mathbf{M}_{pyd} + \mathbf{M}_{rd} \tag{G.11}$$

G.1.2 Aerodynamic Forces And Moments for 7-DOF Model

Explanations of aerodynamic forces and moments which are formed by the guidance kit are given below. Numerical values of these coefficients are taken from [1].

G.1.2.1 Control Forces

These are the forces that arise from the addition of the guidance kit to the projectile.

$$\mathbf{F}_c = \frac{\rho S V^2}{2} C_{N_\delta} \left(\delta_S \begin{bmatrix} 0 \\ \cos\theta_{gk} \\ \sin\theta_{gk} \end{bmatrix} + \begin{bmatrix} 0 \\ \alpha \\ \beta \end{bmatrix} \right) \tag{G.12}$$

G.1.2.2 Control Moments

These are the moments that arise from the addition of the guidance kit to the projectile.

$$\mathbf{M}_C = \frac{\rho S V^2 l_{CG}}{2} C_{N\delta} \left(\delta_S \begin{bmatrix} 0 \\ -\sin p_F \\ \cos p_F \end{bmatrix} + \begin{bmatrix} 0 \\ -\beta \\ \alpha \end{bmatrix} \right) \tag{G.13}$$

To find total aerodynamic force and moments on the guidance kit, it is required to add control forces and control moments to Equation G.10 and Equation G.11. Total aerodynamic force on the projectile with the addition of the guidance kit is given in Equation G.14.

$$\mathbf{F}_{7DOF} = \begin{bmatrix} X_{7DOF} \\ Y_{7DOF} \\ Z_{7DOF} \end{bmatrix} = \mathbf{F}_{6DOF} + \mathbf{F}_c \tag{G.14}$$

Total moment on the projectile with the addition of guidance kit is given in Equation G.15. Since there will be another equation for added 7_{th} DOF to the system related to angular velocity about the X-axis, the component of the total moment on the body of the projectile labeled as L_{B-7DOF}.

$$\mathbf{M}_{7DOF} = \begin{bmatrix} L_{B-7DOF} \\ M_{7DOF} \\ N_{7DOF} \end{bmatrix} = \mathbf{M}_{6DOF} + \mathbf{M}_c \tag{G.15}$$

G.1.2.3 Aerodynamic Torque on Guidance Kit

This is the torque due to the cant angle of the control canards. The direction of this torque is in the opposite direction to the projectile angular velocity.

$$T_{aero} = \frac{1}{2} \rho V^2 S l_{gk} C_{rc} \tag{G.16}$$

G.1.2.4 Aerodynamic Damping Torque on Guidance Kit

This is the damping torque due to the angular velocity of the guidance kit. It is in the opposite direction of the angular velocity of the guidance kit.

$$T_{ad} = \frac{1}{2}\rho S d^2 V p_{gk} C_{rdgk} \tag{G.17}$$

Total aerodynamic torque on the guidance kit is given in Equation G.18.

$$L_{gk-7DOF} = T_{aero} + T_{ad} \tag{G.18}$$